Technische Universität München

TUM School of Engineering and Design

Numerical investigation of the bubble dynamics in consideration of heat and mass transfer

Yuanwei Cao

Vollständiger Abdruck der von der TUM School of Engineering and Design der Technischen Universität München zur Erlangung des akademischen Grades eines Doktors der Ingenieurwissenschaften genehmigten Dissertation.

Vorsitzender:	Prof. Wolfgang Polifke, Ph.D.
Prüfer der Dissertation:	1. Prof. Rafael Macián-Juan, Ph.D.
	2. Prof. Dr. Rafael Miró Herrero

Die Dissertation wurd am 02.06.2021 bei der Technischen Universität München eingereicht und durch die TUM School of Engineering and Design am 09.03.2022 angenommen.

Acknowledgement

First of all, I would thank my supervisor, Prof. Rafael Macián-Juan. In February 2017, he accepted me as a PhD student in my hardest time in Germany. From then on, Prof. Macián-Juan has been giving me all kinds of support. Without him, I cannot finish this thesis. I would also thank Prof. Sergio Chiva Vicent and Dr. Carlos Peña-Monferrer as well. In the first year of my PhD study, they helped me with the research proposal and OpenFOAM. Besides, I would express my appreciation to the entire staff of the department, the technical and administrative stall, all my students, who supported this work. I would thank Prof. Dr. Rafael Miró Herrero for reviewing my thesis and the positive expert comments. Prof. Wolfgang Polifke is also acknowledged for being the president of my thesis commitee.

Last but not least, I want to express my deepest appreciation and love to my families. My parents always support all my decisions. Their hardworking and persistence have been inspiring me. I would express my deepest love to my wife, Dantong. Without her, I could not have such a happy life and family. My daughter, Nuoxi, I cannot express my feelings with any word. I would give all my love to you.

The research work is funded by China Scholarship Council (No. 201606060149), whose financial support was gratefully acknowledged.

Abstract

In this thesis, numerical investigations of the rising bubble dynamics with heat and mass transfer are carried out. Volume of Fluid method is adopted to capture the interface. Continuum Surface Force model is used to calculte the surface tension force. Two phase change models are implemented and assessed to simulate the bubble condensation.

The first part is the numerical study of the isothermal bubble rising in quiescent liquid, including the path instability and the central breakup. The path instability results from the coupling of the bubble shape, path and wake. The vortex dynamics, shape evolution and wake structure are analyzed. The interactions of two in-line bubbles with path instability are studied. The central breakup of a large bubble is caused by the high-speed liquid jet, which is related to the high pressure difference between the top and bottom of the bubble. It is reported for the first time that the collision of the liquid jet on the bubble surface varies the pressure difference, thus changing the jet velocity and affecting the central breakup behaviors. The influences of the bubble size, liquid properties, density and viscosity ratio, initial bubble shape on the central breakup are investigated. All these influencing factors can be clarified with the dimensionless numbers, Galilei number and Eötvös number. Two inline bubbles with different distance are also simulated. A linear relation between the jet (bubble) Reynolds number and Galilei number is summarized.

For a further research, the heat transfer during the bubble rising in quiescent water is investigated. Empirical correlations in terms of temperature for thermophysical properties and equation of state for air are considered in the simulations. The zigzag motion of a compressible air bubble considering the temperature difference with respect to the surrounding water is analyzed. The mechanism of the zigzag motion is clarified by analyzing the shape evolution and the wake structure. The periodic shedding of hairpin vortex with 2R mode is observed during the zigzag motion. There are two periods of the bubble shape oscillation within one zigzag cycle.

In the end, the rising bubble dynamics with heat and mass transfer, i.e. bubble condensation are numerically investigated. Two phase change models, Lee model and Tanasawa model, are assessed using experimental data. The Tanasawa model is adopted for further study after validation. The hydrodynamics of bubble condensation are analyzed. The effects of the bubble size, subcooling, and liquid properties on the bubble condensation are investigated.

Publications

Peer-Reviewed Journal Papers

1. **Cao, Yuanwei**, and Rafael Macián-Juan. The wobbling motion of single and two inline bubbles rising in quiescent liquid. *Physics of Fluids* 33.7 (2021): 073305 (Editor's Pick, Chapter 3)

2. **Cao, Yuanwei**, and Rafael Macián-Juan. Numerical investigation of central breakup of large bubble induced by liquid jet. *Physics of Fluids* 32, no. 3 (2020): 033302. (Chapter 4)

3. **Cao, Yuanwei**, and Rafael Macián-Juan. Numerical study of the central breakup behaviors of a large bubble rising in quiescent liquid. *Chemical Engineering Science* (2020): 115804. (Chapter 4)

4. **Cao, Yuanwei**, Inés Mateos Canals, and Rafael Macián-Juan. Path instability of a compressible air bubble rising in quiescent water with consideration of variable thermophysical properties. *International Journal of Multiphase Flow* (2020): 103320. (Chapter 5)

5. **Cao, Yuanwei**, and Rafael Macián-Juan. Numerical investigation of vapor bubble condensation in subcooled quiescent water. *Nuclear Engineering and Design* 388 (2022): 111621. (Chapter 6)

6. **Cao, Yuanwei**, Inés Mateos Canals, and Rafael Macián-Juan. Numerical investigation of hot and cold bubbles rising in water. *Nuclear*

Engineering and Design 382 (2021): 111390. (not included in the thesis)

Peer-Reviewed Conference Paper

1. **Cao, Yuanwei**, and Rafael Macián-Juan. Coupled Level Set and isoAdvector method for the simulation of gas-liquid flow. *14th international conference on Gas-Liquid and Gas-Liquid-Solid Reactor Engineering* (2019). Guilin, China. (Presentation)

Contributions to Scientific Conferences without a Written Paper

1. **Cao, Yuanwei**, Inés Mateos Canals, and Rafael Macián-Juan. Numerical simulation of compressible air bubble rising in quiescent water with heat transfer. *17th Multiphase Flow Conference and Short Course* (2019). Dresden, Germany. (Poster)

Supervised Bachelor and Master Thesis

1. Vicente Fuerte Marco. Numerical Simulation of Bubble Rising in Still Liquid with OpenFOAM. 2018. (Bachelor thesis)

2. Ignacio Camps Bas. Numerical simulation of the bubble growth and detachment with OpenFOAM. 2019. (Bachelor thesis)

3. Inés Mateos Canals. Numerical Simulation of the Compressibility Effect on Bubble Dynamics in Non-Isothermal Conditions. 2019 (Master thesis)

Contents

List of Figures

List of Tables

List of Acronyms

Re	Reynolds number
Eo	Eötvös number
Mo	Morton number
CFD	Computational Fluid Dynamics
DNS	Direct Numerical Simulation
We	Weber number
Ga	Galilei number
2D	two dimensional
3D	three dimensional
VoF	Volume of Fluid
CLSVOF	Couple level set and volume of fluid method
St	Strouhal number
Re_b	bubble Reynolds number
Ja	Jakob number
Pr	Prandtl number
Nu	Nusselt number

LS level set method

FCT flux corrected transport

CICSAM compressive interface capturing scheme for arbitrary meshes

OpenFOAM Open-source Field Operation And Manipulation

MULES Multidimensional Universal Limiter with Explicit Solution

SLIC simple line interface calculation

PLIC piecewise linear interface calculation

STF surface tension force

CSF Continuous Surface Force

Co Courant number

Z vertical bubble position

MRV mean rise velocity

LB leading bubble

TB trailing bubble

Chapter 1

Introduction

1.1 Background

Bubbles play an important role in a wide range of natural and engineering applications, such as nuclear industry, chemical engineering, enhanced oil recovery, brewing industry etc. [8, 9]. In the nuclear industry, the existence of gaseous bubbles could enhance the heat and mass transfer in the bubbly flow displayed in Figure 1.1. The enhancement of heat and mass transfer depends primarily on the interaction and distribution of the bubbles as well as on the flow characteristics [10]. Thus the heat and mass transfer processes are greatly influenced by the bubble topological changes and by the rising path they follow [11]. On the other hand, the heat and mass transfer can in turn affect the bubble dynamics, such as the bubble shape and rising path, since the fluid properties e.g. density and viscosity, are functions of temperature and pressure. The bubble dynamics is influenced by the variation of physical properties of the two phase flow. Besides, the mass transfer can affect the size of the bubble, which greatly affects the rising bubble dynamics. Therefore, the rising bubble dynamics with heat and mass transfer is a quite complex problem, which needs further research [12].

In bubbly flow, the bubbles may be small and spherical at one extreme, while they may also be large with a spherical cap at the other extreme. The shapes

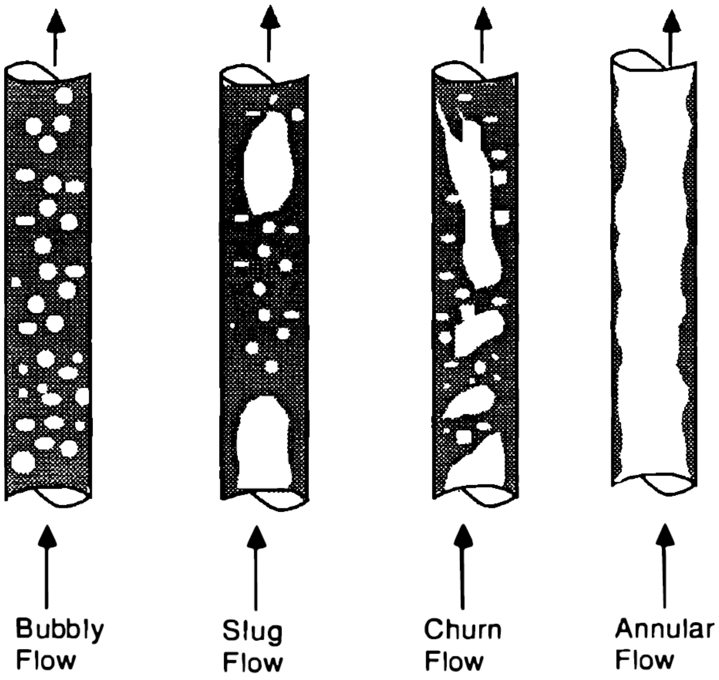

Figure 1.1: Flow patterns in vertical pipes [1]

and paths of the bubble motion depend on many factors, including the bubble size, liquid properties, arrangements etc. However, many aspects about the bubble dynamics such as path instability, breakup, and the influence of the mass transfer are still unclear. Moreover, the analysis of multiple bubbles with different shapes and paths is quite difficult to carry out experimentally and to simulate numerically. Therefore, the investigation and understanding of the flow hydrodynamics of a simplified system consisting of the rising of a single bubble or two bubbles under gravity with heat and mass transfer can play a fundamental role in the analysis and understanding of complex two-phase flow systems containing many bubbles. This thesis focuses mainly on the hydrodynamics of a single bubble or two bubbles rising in quiescent liquid considering heat and mass transfer. To achieve the goal of the thesis, the research is divided into three steps. First, we conduct simulation of the bubble rising in isothermal two-phase systems, which means no heat and mass transfer is considered. The physical properties of the two phases are thought as constant. Second, the heat transfer is considered. The bubble rising in non-isothermal two phase systems is investigated. Last, the mass transfer models are added. In this thesis, this refers to the bubble condensation. The literature review in the next section also follows this logical order.

1.2 State of the Art

1.2.1 Isothermal Bubble Rising Phenomenon

A bubble rising in quiescent liquid is a fundamental problem concerned in the multi-phase fluid mechanics. The bubble rises due to the buoyancy effect, which yields different shapes and paths due to the interaction of the inertia, viscous force and surface tension force. The complexity of the rising bubble dynamics lies on several factors: the external and internal circulations of the two fluids, the interfacial forces between the two phases [13]. To study the rising bubble dynamics, experimental and numerical methods are usually adopted, which are reviewed below.

For the experimental study of a spherical bubble rising in quiescent liquid, a known volume of gas is obtained by an inverted hemispherical cup, which is slowly rotated to carefully release the bubble within the stagnant liquid [13]. By using a high speed camera and image processing, the instantaneous bubble velocity and trajectory can be measured [14].

In the work of Bhaga and Weber [2], different shapes of bubbles rising in quiescent liquid were identified based on three dimensionless parameters: Reynolds number (Re), Eötvös number (Eo), and Morton number (Mo), which are listed in Figure 1.2. The drag experienced by the bubbles and their respective terminal velocities were also measured. Landel et al. [15] extended the experimental work of Bhaga and Weber [2] and demonstrated that bubbles created using an inverted hemispherical cup tend to form a leading spherical cap bubble followed by a crown of satellite bubbles. More recently, Sharaf et al. [3] conducted experimental research on the single spherical bubble rising in quiescent liquid and identified four different regions,

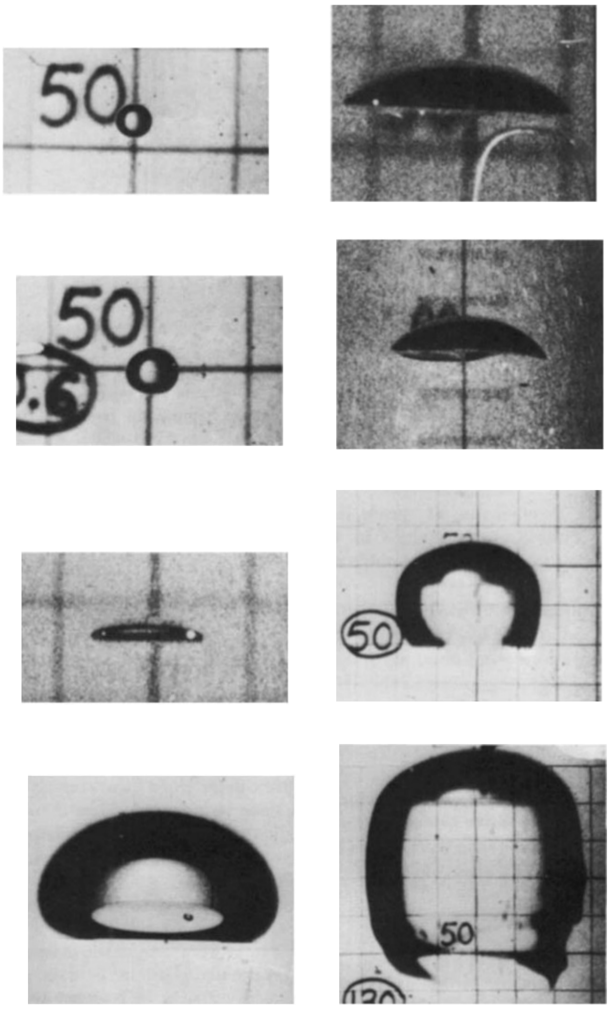

Figure 1.2: Different bubble shapes in the work of Bhaga and Weber [2]

which are axisymmetric, spherical, oscillatory and peripheral breakup. They plotted in the Ga-Eo plane based on their experimental results as shown in Figure 1.3.

With the increase of the computing power, Computational Fluid Dynamics (CFD) has emerged as a powerful tool for the investigation of rising bubble dynamics. We can get detailed information from the numerical results than the experimental ones, such as the wake structures, interface information and the flow field inside the bubble. With the aid of the CFD tools, significant progress has been achieved about the understanding of the rising bubble

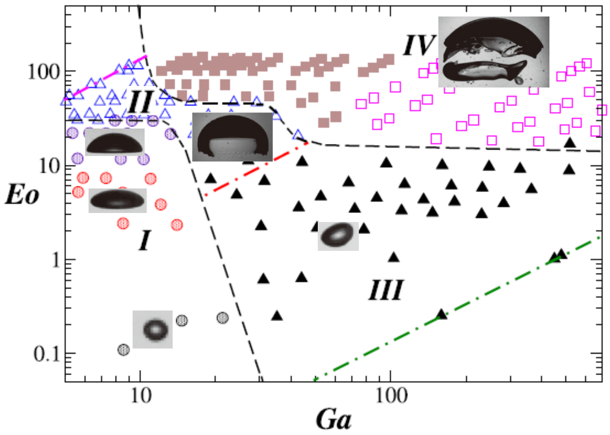

Figure 1.3: Different regions of bubble shape and behaviour obtained from the experimental work of Sharaf et al. [3].

dynamics.

A representative and comprehensive numerical work has been reported by Tripathi et al. [4]. They conducted Direct Numerical Simulation (DNS) for a bubble rising in quiescent liquid, covering a wide range of Galilei number (Ga) and Eo numbers. Based on the observation of the shape evolution and the rising path, they divided the behavior patterns of the air bubble into five regions plotted in the Ga–Eo plane based on their simulation results shown in Figure 1.4, which are axisymmetric (region I), skirted (region II), oscillatory (region III), peripheral breakup (region IV), and central breakup (region V). The numerical results agree well with the experimental ones by Bhaga and Weber [2] and Sharaf et al. [3].

Among the different regimes in Figure 1.4, the path instability in region III and bubble breakup in region V attract the most attention due to their complexity and wide engineering applications, which are reviewed in the following sections.

1.2.1.1 Path Instability

Among the different regimes in Figure 1.3, a bubble in region III rises in a zigzag or a spiral path. The bubble maintains its integrity but its shape

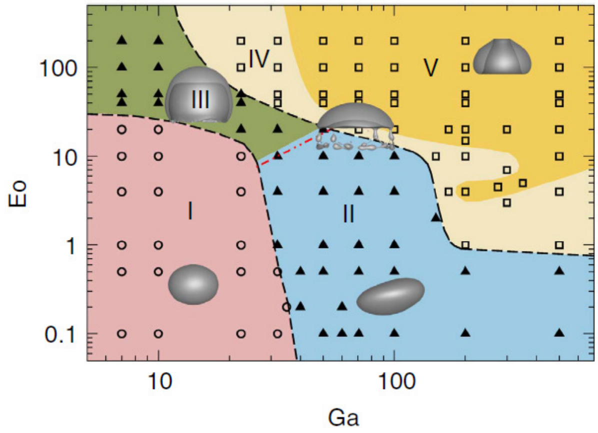

Figure 1.4: Different regimes of bubble shape and behavior in the work of Tripathi et al. [4].

changes with time due to the influence of a relatively low surface tension. Due to the coupling of the bubble shape, path and wake, the rising path is unsteady, which is a clear sign of path instability and gets the most attention because of its complexity.

Winnikow and Chao [16] showed two wake regimes for a bubble rising. The bubble in the first regimes form a stationary wake while oscillations and periodic vorticity discharges were observed in the second regime. They suggested that the transition between the non-oscillating and oscillating regimes happens at the critical Weber number (We) of 4. Ryskin and Leal [17] thought the vortex shedding leads to the path instability. Duineveld [18] confirmed for the first time that the bubble presented an oscillatory path in water when the bubble radius is bigger than 0.91 mm by using hyper-purified water. Tomiyama et al. [19] conducted experiments using air and water to measure bubble trajectories, shapes and velocities. They found that the prime cause of widely scattered terminal velocity in this regime is the initial bubble's shape. Small initial shape deformation resulted in a low velocity and a high aspect ratio. However, in Vries's work [20], no vortex shedding in a region of path instability was found. Christian et al. [21] studied the air bubbles rising in purified water and found that the oscillations were indicated as (2,0) axisymmetric and with wavelength equal to the distance from pole to pole and (2,2) non-axisymmetric and with wavelength equal to one-half of the length of the equator. By ruling out contamination effects, Wegener et al. [22–24] conducted a series of experiments about the oscillating bubbles. In addition to the monitoring of the change between oscillating regimes at a critical We, an additional transition for the water/toluene system was also observed. For a certain diameter range with $We < We_{cr}$, they found that bubbles suffer a sharp reduction in rise velocity right after an initial acceleration and then oscillate.

Even though some advances have been made with the above mentioned works, some aspects still remain unclear, such the influence of density and viscosity ratios on the path instability. Therefore it is necessary to conduct further research on this problem, which is one of the goals of this thesis.

1.2.1.2 Bubble Breakup

Bubble breakup is encountered in many natural and engineering applications. Examples include condensation [25], underwater explosion [26], ultrasonic cleaning [27, 28], shock wave lithotripsy [29], cavitation [30] and so on. During the bubble breakup process, bubbles often yield violent jets as a result of their rapid out-of-equilibrium dynamics [31]. To improve the understanding of the bubble breakup behavior, the simplified system of a large bubble rising in quiescent liquid is numerical investigated in this work.

The central breakup bubble or toroidal bubble has been observed in some experimental and numerical works [26, 31–33]. Séon and Antkowiak [31] observed the long and narrow jets shooting out in disconnecting large elongated bubbles. The height of the bubble in their experiment is 4.22cm. They ruled out the effect of pinch-off singularity and found that the liquid jet leading to the rupture of the bubble was driven only by gravity. In the field of underwater explosion, Zhang et al. [26] created a "discharged vapor bubble" with diameter of 50mm in their experiment. The toroidal bubble formed by a liquid jet can be clearly observed. They also analyzed the bubble migration, jet velocity and jet initiation time. Liu et al. [33] studied the dynamics of a toroidal bubble near a solid wall for different stand-off parameters by simulating a toroidal bubble. Li et al. [34] investigated the strong bubble interactions and bursting behaviors near a free surface using a compressible two phase flow solver.

However, by comparing the experimental results in [3] and the numerical results in [4], we find that all the regions except the central breakup region (V) are identified in their experiments as is shown in Figure. 1.5. Actually, most of the numerical results appear to agree excellently with the experimental observations, except for the formation of unstable toroidal bubbles in systems with large bubbles and low surface tension [13]. The reason can be attributed to the difficulty in creating large spherical bubbles experimentally [4, 13]. In experimental setups an inverted hemispherical cup is used to retain gas with a known volume and then slowly rotated to release the bubble into the stagnant liquid. In this procedure the initial shape of the bubble is approximately ellipsoidal [13] and the initial bubble shape can influence the final state of the bubble [35, 36]. Therefore, the formation of the toroidal bubble for a large spherical bubble rising in quiescent liquid needs further numerical research.

Several numerical works on the central breakup of a large spherical bubble rising in quiescent liquid can be found in [4, 13, 36, 37]. Chen et al. [37] discussed the physical mechanisms for the the formation of a toroidal bubble. They found that when the Reynolds number reaches a value of 28 and the Bond number exceeds 20, toroidal bubbles are formed. Bonometti and Mafnaudet [36] conducted a two dimensional (2D) simulation on the transition from sphrical cap to toroidal bubbles based on the values of the Bo number and the Ar number. Tripathi et al. [4] suggested a different delineation of stable and unstable regions based on their three dimensional (3D) simulation from the 2D results of Bonometti and Mafnaudet [36]. Gumulya et al. [13] obtained the critical bubble Reynolds number as a function of the Eo num-

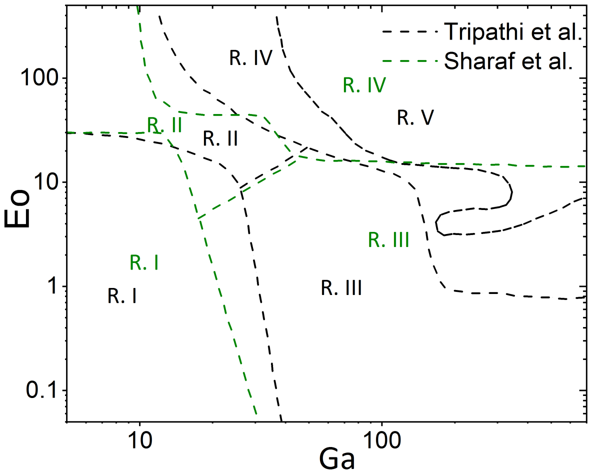

Figure 1.5: Bubble shapes in different regions [5]. The green dot line is from [3] and black from [4].

ber, above which the toroidal bubble formation is expected. The author also highlighted the importance of 3D simulations.

However, despite the above mentioned investigations, there are still many aspects which are not well described and analyzed for a large spherical bubble rising in quiescent liquid. Therefore, the fully 3D simulation of large bubbles rising in quiescent liquid in central breakup region is conducted in this thesis [5, 38]

1.2.2 Non-isothermal Bubble Rising Phenomenon

In many engineering applications, there exists heat transfer between the two phases. Besides, all the physical properties, including density, viscosity, surface tension and thermal conductivity, are functions of the temperature, which could affect the bubble dynamics and can not be ignored.

Some researchers study the bubble dynamics with the variation of one property such as surface tension [39, 40] or viscosity [41, 42]. A review of these studies can be found in the work of Sahu [43]. The surface tension of water decreases almost linearly with increasing temperature, which is termed as "linear" fluid[39]. The thermocapillary motion of bubbles in a "linear" fluid was first reported by Young et al. [44]. Tripathi et al. [39] conducted a simulation of bubble rising by considering a linear and quadratic dependence of surface tension on temperature without referring to path instability. Balla et al. [40] simulated the bubble rising in "self-rewetting" fluid. The viscosity of water can also vary due to the presence of temperature variation. Tsamopoulos et al. [45] studied the buoyancy-driven rise of a bubble in a Newtonian or a viscoplastic fluid assuming axial symmetry and steady flow. However, in reality, all the physical properties, including density, viscosity, surface tension and thermal conductivity, are functions of temperature, which could affect the bubble dynamics and can not be ignored. Therefore it is crucial to account for the variation of thermophysical properties and the compressibility of air for the investigation of bubble rising dynamics in consideration of the temperature difference between the bubble and the surrounding fluid. However, this research topic is barely covered in the literature [46]. Therefore, another objective of the thesis is to simulate a compressible air bubble rising in quiescent water with variable thermophysical properties and compare the results among the cases with different thermal conditions.

1.2.3 Bubble Condensation

When a vapor bubble is exposed into subcooled liquid, heat is transferred from the bubble to the liquid, causing eventually the bubble condensation and collapse. The bubble condensation is an extremely complex problem, depending on many factors, including the subcooled temperature, system pressure, fluid properties, vapor bubble size and so on. Thus, it is a rather difficult problem numerically, and most of the previous works are experimental.

With the advancement of numerical techniques in CFD and the development of powerful supercomputers, many researchers have tried to model bubble condensation by incorporating phase change models. Jone et al. [47] used a 2D Volume of Fluid (VoF) method to study the bubble condensing behaviors. The phase change models in their paper was derived from the interfacial heat transfer coefficient estimated by an empirical formula. Pan et al. [48] investigated 3D bubble condensation in vertical channel. Two empirical correlations were incorporated into the phase change model and simulation results agreed well with the experiments. Zeng et al. [49] adopted a CLSVOF to study the bubble condensation. The phase change model was obtained by the local superheat and the interfacial heat resistence. Qu and Tian [50] also adopted empirical correlations for the numerical simulation of steam-air jet condensation. Liu et al. [51] implemented five phase change models in FLUENT and assessed them for the simulation of bubble condensation.

Although many investigations have been conducted on the bubble condensation process in the past, there still exist many problems unresolved. Until now, there is no universal phase change model that is suitable for all flow conditions. The mechanism of bubble condensation is still not fully understood. Some factors that influence the bubble condensation have not been investigated. Therefore, in this thesis, the appropriate phase change model is determined based on the experimental data. The effects of bubble diameter, subcooled temperature, liquid viscosity and surface tension on the bubble condensation are analyzed.

1.2.4 Dimensionless Numbers

In dimensionless formulation, a rising bubble can be completely described by four dimensionless numbers [4]: Ga, Eo, density ratio (ρ_r) and viscosity ratio (μ_r).

$$Ga = \frac{\rho_0 \sqrt{g} R^{3/2}}{\mu_0} \tag{1.1}$$

$$Eo = \frac{\rho_0 g R^2}{\sigma} \tag{1.2}$$

$$\rho_r = \frac{\rho_i}{\rho_0} \tag{1.3}$$

$$\mu_r = \frac{\mu_i}{\mu_0} \tag{1.4}$$

Where R is the radius of the bubble, ρ_0, μ_0 and ρ_i, μ_i are density and viscosity of the continuous and dispersed phases, respectively. The Ga number represents the ratio of gravity force to viscous force and the Eo number represents the ration of gravity force to surface tension force.
To study the oscillatory motion of a bubble, we introduce the Strouhal number (St), which is defined as:

$$St = \frac{fD}{U_T} \tag{1.5}$$

Where f is the oscillation frequency of the path and U_T is the bubble terminal velocity [52]. The bubble Reynolds number (bubble Reynolds number (Re_b)) can be defined as:

$$Re_b = \frac{\rho_0 V_b d}{\mu_0} \tag{1.6}$$

where V_b is the terminal velocity of the bubble, and d is its diameter. To describe the heat and mass transfer, the following dimensionless numbers, Jakob number (Ja), Prandtl number (Pr), and Nusselt number (Nu) are defined:

$$Ja = \frac{\rho_0 C_{p,0} \Delta T_{sub}}{\rho_i h_{fg}} \tag{1.7}$$

$$Pr = \frac{C_{p,0}\mu_0}{\kappa_0} \tag{1.8}$$

$$Nu = \frac{hD_0}{\kappa_0} \tag{1.9}$$

where $C_{p,0}$ is the specific heat capacity of the liquid, ΔT_{sub} is the subcooled temperature, h_{fg} is the latent heat, κ is the thermal conductivity.

1.3 Numerical Methods

1.3.1 Interface Capturing Method

Despite the high quality of the experimental work, however, it is virtually impossible to trace flow separation and vortex detachment in such delicate two phase system, not to mention the difficult access to the interfacial related dynamics with experiments [53]. The development of sophisticate non-intrusive visualization techniques is still in process [54]. In such a context, numerical simulations based on CFD appears to be a powerful tool and it has been adopted by many researchers for the purpose of better understanding the details of the flow in bubbly conditions . After the code validation, numerical simulation helps to increase the understanding of the bubble dynamics.

The numerical simulation of the rising bubble is rather difficult due to the following reasons: 1) the discontinuities of the fluid properties such as density and viscosity across the interface, which could lead to numerical instability; 2) the interface locations should be tracked/captured accurately as it evolves; 3) last but not the least, the interface sharpness should be maintained throughout the simulation. To overcome these difficulties, implicit interface capturing approaches like VoF [55] and level set method (LS) [56] have proven to be efficient in simulating multiphase flows.

The LS method was first developed by Osher and Sethian [56] and implemented for multiphase flows by Sussman et al [57]. The distinction between the two fluids in the mixture relies on a distance function ϕ, which has a positive value in one fluid and a negative value in the other. The interface ($\phi = 0$) is advected by solving a transport equation and a reinitialization process is required to recover the distancing property. The LS method provides a sharp interface and smooth variation of the physical properties across the interface. However the LS method does not preserve mass conservation due to the re-distancing process. The detailed discussion can be found in the work of Chene et al [58] and Gibou et al [59], which could shed light on this issue. Some improvements have been proposed to solve this problems [60, 61]. For example, Coquerelle and Glockner [60] propose a fourth-order curvature extension algorithm in a LS framework. In the work of Zhang and Yue [61], a high order interface preserving reinitialization method is proposed. The gradient of LS function is computed by solving a Hamilton-Jacobi equation as a conservation law system using the disscontinuous Galerkin method.

In the VoF method [55], the volume fraction α in every cell is used to distinguish the two fluids, where $0 < \alpha < 1$ represents the interface. The interface transport equation is solved either by an algebraic compressive scheme or by a geometrical reconstruction coupled with a geometrical approximation of the volume of fluid advection. Mass conservation can be achieved with this method.

For the algebraic VoF method, the interface typically spreads over a few cells and a geometric interface reconstruction is, therefore not needed. The main algebraic VoF methods include the donor-acceptor scheme by Hirt and Nichols [55], the flux corrected transport (FCT) scheme by Rudman [62], and the compressive interface capturing scheme for arbitrary meshes (CICSAM) by Ubbink and Issa [63]. In Open-source Field Operation And Manipulation (OpenFOAM) [64], the algebraic VoF method is called Multidimensional Universal Limiter with Explicit Solution (MULES) [65]. The algebraic method is time saving because of no geometric interface reconstruction and the extension to 3D and unstructured mesh is straightforward. However, the interface smearing is encountered for most of algebraic VoF methods [66, 67]. Recently, in the work of Hill et al [68], a sharp interface advection method was presented, which has sophisticated algebraic interface advection schemes.

For the geometric VoF, the interface position is determined by calculating the interface normal vector and the interface shape is solved using piecewise constant or piecewise linear schemes. They include the simple line interface calculation (SLIC) [69], the piecewise linear interface calculation (PLIC) [70]. Recently, Roenby et al. [71] created a new geometric VoF advection scheme which is called isoAdvector method and is already implemented in OpenFOAM, where the iso-surface is used to reconstruct a sharp interface. In this thesis, the isoAdvector method is adopted to simulate the bubble central breakup behaviors.

In addition to capturing the interface, the numerical challenge of representing the surface tension force (STF) is also encountered by both methods (VoF and LS). The common method is to represent the STF as a source term in the momentum equation using the Continuous Surface Force (CSF) model [72].

The calculation includes an approximation of the interface curvature from the gradients of either the VoF or LS function as well as the calculation of the normal to the interface. For the VoF method that suffers from diffusion, it is rather difficult to achieve an accurate representation of the interface curvature. For the LS methods with a sharp interface reconstruction, the volumetric force of the surface tension is confined to a narrow region around the interface and the calculation of normal vector can be numerically unstable. These numerical effects are known to generate non-physical velocities known as “parasitic currents” [66, 67]. The appearance of parasitic currents is problematic for capillary flows and surface tension dominated flows. The issue becomes more prominent in large density ratio flows, as the interface force imbalance becomes larger.

The CLSVOF method has drawn many researchers’ attention because it combines the advantages of both the VoF (mass conservation) and the LS methods (interface sharpness). Sussman and Puckett [73] proposed a fully CLSVOF method by advecting the interface using a VoF function, calculating the interface normal using a LS function and, then, updating the physical properties from a smoothed Heaviside function. Wang et al. [74] combined the LS and the PLIC VoF methods for the simulation of plunging breaking waves. Albadawi et al [75] coupled the LS and the MULES VoF methods to simulate bubble formation, which will be used for the simulation of a compressible air bubble rising in quiescent water with variable thermophysical properties in this thesis. Dianat et al. [76] also coupled LS and PLIC VoF method in the framework of OpenFOAM for the simulation of automotive exterior water management.

1.3.2 Phase Change Models

The occurrence of mass transfer due to the phase change in the interface makes the two-phase schemes for interface tracking or capturing more complex. In the presence of interfacial mass transfer, interface topology tends to be less stable, and the developed schemes must be capable of tackling this issue [77]. The transfer of the mass, momentum, heat across the interface must also be estimated accurately. Due to the complexity of the phase change problems, there is still no universal numerical solution to a two-phase flow problem involving phase change. In the framework of interface capturing method, different phase change models have been developed to solve different flow conditions, which are reviewed here.

Lee [78] developed a simplified saturation model to solve the evaporation and condenstaion problems. In this model, the phase change occurred due to the deviation of interfacial temperature from the saturation temperature. which has been used widely in the research of phase change phenomena [79, 80]. Overall, the Lee model is a simplified saturation model that does not set limits on the value of mass transfer rate which is based on the empirical parameters. But this lack of specificity is advantageous since it allows researchers to set their own appropriate value. Therefore, the Lee model serves as a good starting point to study rather complex phase change phenomena. Thus the Lee model is used in this thesis as a choice of the phase change models.

In the 1950s, Schrage [81] proposed a phase change model using the kinetic gas theory based on the Hertz-Knudsen equation. It is assumed that the vapor and liquid are in saturation states, allowing for the temperature and pressure jump across the interface. Based on the Schrage model, Tanasawa [82] further simplified it by suggesting the dependence of mass flux on temperature jump between the interface and vapor phase. The application of the Schrage model and Tanasawa in the study of phase change phenomena can be found in [49, 83]. Overall, these two models are both physically based and account for the kinetic energy effects. Therefore, the kinetic gas theory model is adopted as an alternative for the study of bubble condensation.

Another phase change model to account for the mass transfer is the Rankine-Hugoniot jump condition [84], where the mass transfer rate is based on the net energy transfer across the interface. The example of using this model for phase change phenomena can be see in [85]. Although this model is physically based and free from empiricism, it does not account for the kinetic

Table 1.1: Empirical correlations of bubble condensation in literatures.

Author	Correlations	range of applicability
Isenberg and Sideman [86]	$Nu = (1/\pi)Re_b^{1/2}Pr^{1/3}$	-
Akiyama [87]	$Nu = 0.37Re_b^{0.6}Pr^{1/3}$	-
Chen and Mayinger [88]	$Nu = 0.185Re_b^{0.7}Pr^{0.5}$	$0 < Re_b < 1000, 0 < Ja < 80, 2 < Pr < 15$
Warrier et al. [89]	$Nu = 0.6Re_b^{1/2}Pr^{1/3}[1 - 1.2Ja^{0.9}Fo^{2/3}]$	$20 < Re_b < 700, 12 < Ja < 100, 1.8 < Pr < 2.9$
Yuan et al. [90]	$Nu = 0.6Re_b^{1/2}Pr^{1/3}[1 - Ja^{0.1}Fo]$	$335 < Re_b < 1770, 20 < Ja < 60, 1.71 < Pr < 1.75$
Lucic and Mayinger [91]	$Nu = 1.46Re_b^{0.61}Ja^{-0.31}Pr^{0.33}$	$1000 < Re_b < 3400, 10 < Ja < 30$
Kim and Park [92]	$Nu = 0.2575Re_b^{0.7}Ja^{-0.2043}Pr^{-0.4564}$	$1000 < Re_b < 6000, 18 < Ja < 36, 1.87 < Pr < 2.03$
Issa et al. [25]	$Nu = 0.0609Re_b^{0.89}Pr^{1/3}$	$2000 < Re_b < 270000, 16 < Ja < 35, 1.75 < Pr < 1.9$
Tang et al. [93]	$Nu = 4.34Re_b^{0.584}Ja^{-0.419}Pr^{0.333}$	$1000 < Re_b < 30000, 45 < Ja < 180, 2.1 < Pr < 4.3$

energy contributions, and this model is not used in this thesis.

The last reviewed phase change model is the empirical correlation model, where the mass transfer rate is calculated using the different empirical correlations obtained from different experimental data. A summary of the empirical correlations proposed by different researchers is list in Table 1.1 [51]. As we can see in Table 1.1, there are many variability of the correlations, even in the same range of a specific parameter. Therefore, the empirical correlation model is not considered in this thesis.

1.4 Objective of the Thesis

The goal of the thesis is to gain a comprensive understanding of the bubble dynamics in consideration of the heat and mass transfer. To achieve this objective, three steps are considered in this thesis: 1) isothermal bubble dynamics (no heat and mass transfer); 2) non-isothermal bubble dynamics (with heat transfer); 3) bubble condensation (with heat and mass transfer). The detailed descriptions are summarized below:

- To obtain a detailed understanding of the bubble dynamics without heat and mass transfer. The rising bubble yields different behavior patterns referring to the shape evolution, terminal velocity, and rising path, which will affect the heat and mass transfer rate. The bubbly dynamics are affected by different factors, such as the liquid properties, bubble size and shape, etc. Among others, the phenomena of path instability and bubble breakup are the most complex, which are the research focus of the isothermal bubble dynamics. The physical properties of the two phases are constant and there is no heat transfer across the interface between the gas and the liquid. The research of isothermal bubble dynamics can serve as a basis for the more complex investigation when heat and mass transfe across the interface is considered.

- After the study of the isothermal bubble dynamics, we would take a step furhter, in which the heat transfer across the interface is considered. The typical two-phase flow, air bubble rising in quiescent water is simulated, which is also beneficial for the investigation of bubble condensation. A millimeter-sized air bubble rising in water usually yields oscillatory behavior, referring to the path instability in the first part. In real application, the thermal-physical properties of water is temperature-dependent (atmospheric pressure) and the air of certain volume will expand/contract when the temperature difference exists. Therefore, we would gain a comprehensive understanding of the non-isothermal bubble dynamics when there is heat transfer across the interface and the thermal-properties varies with temperature.

- In the last step, the bubble condensation behavior is simulated and investigated. As review in Section 1.3.2, there is still no universal phase change model for the simulation of bubble condensation. The Lee model and Tanasawa model are adopted and assessed with experimental data. After that, the most appropriate phase change model can be decided, which will be used for the study of bubble condensation. The bubble dynamics during the condensation will be analyzed. Then the influencing factors which affect the bubble dynamics are studied under the circumstance of bubble condensation, including the physical properties, bubble size, etc. With the previous study of isothermal and non-isothermal bubble dynamics, we can gain a good understanding of the bubble dynamics with heat and mass transfer, which is the final objective of this thesis.

1.5 Outline of the Thesis

To achieve these goals, the thesis contains the following chapters:

- Chapter 2 describes the governing equations for the two-phase flows with heat and mass transfer. The VoF method is introduced in detail. The calculation method for the surface tension is covered. Different phase change models are clarified.

- Chapter 3 addresses the mechanism of the path instability of a bubble rising in quiescent liquid. The wake structures, bubble wobbling, the aspect ratio, and forces are analyzed. The interactions of two in-line bubbles are covered.

- Chapter 4 contains the detailed simulation results of the bubble central breakup behaviors. The mechanism of central breakup is analyzed. The influence of bubble size, liquid properties, initial bubble shape on the central breakup are presented. All these influencing factors are non-dimensionlized. Two inline bubbles are simulated. A simple linear relation between the jet Reynolds number and Ga number is summarized.

- Chapter 5 includes the validation of the compressible two-phase flow solver with heat transfer using the experimental results of 3D bubble rising and theoretical solution of a static bubble. The parasitic currents are analyzed. The simulation results of the path instability of a compressible air bubble rising in quiescent water with variable thermophysical properties are presented. Four cases are investigated: 1) isothermal water and air (293K); 2) hot air (363K) in cold water (293K); 3) isothermal water and air (363K); 4) cold air (293K) in hot water (363K). The mechanisms behind the path instability including the shape evolution, wake structure and vortex dynamics are analyzed.

- Chapter 6 is the numerical investigation of bubble condensation. First, the phase change models are evaluated using the published experimental data. The influence of empirical coefficient, mesh size, 2d and 3D simulation is covered. The mechanisms are clarified. Different influencing factors on the bubble condensation are discussed.
- Chapter 7 is devoted to the conclusion and outlooks of the whole thesis.

Chapter 2

Physical and Numerical Model

To study the bubble dynamics with/without the heat and mass transfer, including the shape, path, terminal velocity, etc, the VoF method as implemented in OpenFOAM v1806 has been adopted to capture the bubble interface. 3D simulations have been conducted in this work for such purpose. In this context the CSF model is used to calculate the surface tension. Two phase change models, Lee model and Tanasawa model, are implemented. This chapter describes these numerical methods employed in the thesis work.

2.1 Governing Equations

In the VoF method, the volume fraction is represented by a discontinuous scalar function which is applied for the two-phase interface tracking in fixed Eulerian grids [55]. This scalar function is defined as the ratio of one fluid volume to the volume of the computational cell (Figure 2.1):

$$\alpha(\mathbf{x},t) = \begin{cases} 1 & \mathbf{x} \in \text{tracked phase} \\ 0 < \alpha < 1 & \mathbf{x} \in \text{interface} \\ 0 & \mathbf{x} \in \text{other phase} \end{cases} \tag{2.1}$$

The volume fraction makes it possible to use only one set of equations to

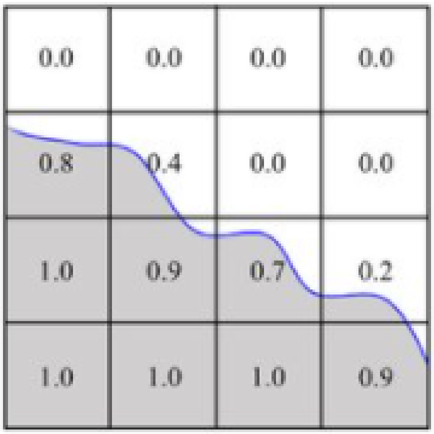

Figure 2.1: The definition of volume fraction [6].

describe the local properties. The physical properties such as density (ρ), viscosity (μ), specific heat capacity (C_p), and thermal conductivity (λ) are calculated using a volume-weighted average:

$$y = \alpha y_l + (1.0 - \alpha) y_g, \quad y \in [\rho, \mu, C_p, \lambda] \tag{2.2}$$

Where l and g are the liquid and gas phase respectively. The governing equations for mass, momentum, energy conservation and advection equations are:

$$\nabla \cdot \rho \mathbf{U} = \dot{m} \tag{2.3}$$

$$\frac{\partial \rho \mathbf{U}}{\partial t} + \nabla \cdot \rho \mathbf{U}\mathbf{U} - \nabla \cdot \mu \nabla (\mathbf{U}) = \mathbf{F}_\sigma - (\mathbf{g} \cdot \mathbf{x}) \nabla \rho - \nabla p_d \tag{2.4}$$

$$\frac{\partial \rho C_p T}{\partial t} + \nabla \cdot (\rho C_p \mathbf{U} T) - \nabla \cdot (\kappa \nabla T) = S_{com} + S_e \tag{2.5}$$

Where $\mathbf{U}$ is the velocity vector, $F_\sigma$is the surface tension force, $\mathbf{g}$ is the gravitational acceleration, t is the time and $p_d = p - \rho(\mathbf{g} \cdot \mathbf{x})$ is the dynamic pressure used to avoid any sudden changes in the pressure at the boundaries for hydrostatic problems. T is the temperature. Here, $\dot{m}$ is the volumetric mass source term, non-zero only at the interface. The sign convention is that a positive $\dot{m}$ represents evaporation and a negative $\dot{m}$ is associated with condensation. The volumetric energy source term S_e is obtained by multiplying mass source term by the latent heat h_{fg}:

$$S_e = \dot{m}h_{fg} \tag{2.6}$$

Note that $\dot{m}$ is set to zero when there is no phase change, which means $\dot{m}$ and S_e are only considered in Chapter 6. In Equation 2.5, S_{com} is the kinetic energy term:

$$S_{com} = -\frac{\partial \rho K}{\partial t} + \nabla \cdot (\rho \mathbf{U} K) + \nabla \cdot (\mathbf{U} p) \tag{2.7}$$

where $K = |\mathbf{U}|^2/2$ is the specific kinetic energy. The term S_{com} is only considered for the non-isothermal two-phase flow, which is only adopted in Chapter 5. In addition, the interface advection equation of the ith phase is:

$$\frac{\partial \alpha_i}{\partial t} + \nabla \cdot (\alpha_i \mathbf{U}) = \frac{\dot{m}_i}{\rho_i} + \alpha_{com} \tag{2.8}$$

where α_{com} results from the compressibility effect and is defined as:

$$\alpha_{com} = \alpha(1-\alpha)(\frac{1}{\rho_2}\frac{d\rho_2}{dt} - \frac{1}{\rho_1}\frac{d\rho_1}{dt}) + \alpha \nabla \cdot \mathbf{U} \tag{2.9}$$

Like S_e and S_{com}, α_v and α_{com} are only considered in Chapter 6 and Chapter 5, respectively.

2.2 Interface Capturing Method

To solve Euqation 2.8, two kinds of VoF methods are adopted in OpenFOAM v1806. One is the geometric VoF method, isoAdvector [71], which is used for the simulation of isothermal two phase flow (chapter 3 and 4). The other is the algebraic VoF method, MULES [65], which is used for the simulation of compressible non-isothermal two-phase flow with/without phase change (chapter 5 and 6). These two VoF methods are discussed in the following sections.

2.2.1 Geometric VoF Method: IsoAdvector

The isoAdvector method uses the concept of isosurface to calculate the face fluxes for the cells containing the interface more accurately. Roenby et al.[71] reported that it can reconstruct a sharp interface and keep a good mass conservation property. The volume fraction in cell n at time t, $\alpha_n(t)$, is calculated from a function $H(\mathbf{x}, t)$,

$$\alpha_n(t) = \frac{1}{V_n} \int_{\Omega_n} H(\mathbf{x}, t) dV \tag{2.10}$$

Where V_n is the volume of cell n, Ω_n represents each cell and $H(\mathbf{x}, t)$ is defined as:

$$H(\mathbf{x}, t) = \frac{\rho(\mathbf{x}, \mathbf{t}) - \rho_G}{\rho_L - \rho_G} \tag{2.11}$$

The phase fractions in next time step read:

$$\alpha_n(t + \Delta t) = \alpha_n(t) - \frac{1}{V_n} \sum_{j \in B_n} S_{nm} \int_t^{t+\Delta t} \int_{F_m} H(\mathbf{x}, t) \mathbf{U}(\mathbf{x}, t) \cdot d\mathbf{S} d\tau \tag{2.12}$$

where B_n represents the boundary of cell n , S_{nm} is used to orient the flux out of the cell and τ is the time integration variable. $d\mathbf{S}$ is the differential area vector pointing out of the volume. S_{nm} is $+1$ or -1 so that $S_{nm} d\mathbf{S}$ points out of cell n for face m. F_m is the face m of the cell n. The time integral on the right hand side in Equation (2.12) can be replaced by $\Delta V_m(t, \Delta t)$ which describes the total volume of fluid transported across face m during one time step

$$\Delta V_m(t, \Delta t) = \int_t^{t+\Delta t} \int_{F_m} H(\mathbf{x}, t) \mathbf{U}(\mathbf{x}, t) \cdot d\mathbf{S} d\tau \tag{2.13}$$

This is the fundamental quantity estimated to advance α_n in isoAdvector method. Another important velocity field representation are the volumetric fluxes across the mesh faces,

$$\phi_m(t) = \mathbf{U}(\mathbf{x}, \tau) \cdot d\mathbf{S} \tag{2.14}$$

The bounding procedure, including the upper and lower bounding, clipping, to limit volume fraction between 0 and 1. The detailed description of isoAdvector algorithm and implementation as well as the evaluation and validation can be found in [71, 94].

2.2.2 Algebraic VoF Method: MULES

In the compressible non-isothermal two-phase flow solver, we use the MULES method [95] to solve Equation 2.8, which is improved based on FCT [96]. The idea of the MULES method is to add an anti-diffusion term into the left side of Equation 2.8:

$$\frac{\partial \alpha}{\partial t} + \nabla \cdot (\alpha \mathbf{U}) + \nabla \cdot \mathbf{U}_c \alpha (1 - \alpha) = \alpha_v + \alpha_{com} \tag{2.15}$$

$\mathbf{U}_c$ is given by

$$\mathbf{U}_c = min(c_\alpha |\mathbf{U}|, max|\mathbf{U}|) \frac{\nabla \alpha}{|\nabla \alpha|} \tag{2.16}$$

Where c_α is the compression coefficient. Here $c_\alpha = 1$ is used in the present study, since increasing or decreasing it can exacerbate errors in interfacial curvature and interfacial smearing [67]. In practice, values of $1 \leq c_\alpha \leq 4$ give good behaviour [67, 97] although for some cases it might be useful to use $c_\alpha > 4$. $max|\mathbf{U}|$ is the largest value of $|\mathbf{U}|$ anywhere in the domain whereas $min(c_\alpha |\mathbf{U}|, max|\mathbf{U}|)$ returns the minimum $(c_\alpha |\mathbf{U}|)$ field limited by maximum $|\mathbf{U}|$. In this way, a sharp interface is maintained and the volume fraction α is limited to values between 0 and 1.

2.2.3 CLSVOF

The CLSVOF method in the work of Albadawi et al.[75] is adopted here to improve the surface tension calculation in Chapter 5. After solving Equation (2.15) using MULES, a new level set field φ is introduced by the iso-line contour $\alpha = 0.5$ [75],

$$\varphi_0 = (2\alpha_L - 1) \cdot \Gamma \tag{2.17}$$

Where Γ is a small non-dimensional number whose value depends on the mesh size Δx (non-dimensional by dividing the length scale m), $\Gamma = 0.75\Delta x$. Then the re-initialization equation is given by:

$$\begin{cases} \frac{\partial \varphi}{\partial \tau} = S(\varphi_0)(1 - |\nabla \varphi|) \\ \varphi(\mathbf{x}, 0) = \varphi_0(\mathbf{x}) \end{cases} \tag{2.18}$$

where τ is a fixed artificial time step which is chosen as $\Delta\tau = 0.1\Delta x$ and $S(\phi_0)$ is a sign function defined as,

$$S(\varphi_0) = \frac{\varphi_0}{|\varphi_0|} \tag{2.19}$$

To solve Equation (2.18), only a few iterations (ϕ_{corr}) are required according to Albadawi et al. [75]. The number of iterations ((ϕ_{corr})) is defined as:

$$\phi_{corr} = \frac{\epsilon}{\Delta\tau} \tag{2.20}$$

where ϵ is the non-dimensional interface thickness calculated as $\epsilon = 1.5\Delta x$. The flow chart of CLSVOF method is displayed in Figure The code implementation is in the Appendix A.

2.3 Calculation of the Surface Tension Force

The CSF model [72] is adopted here to calculate the surface tension force, which is represented as a source term in the momentum equation. The calculation includes an approximation of the interface curvature from the gradients of the VoF function as well as the calculation of the vector normal to the interface.

After solving the advection equation (Equation 2.8, the surface tension force $\mathbf{F}_\sigma$ in Equation 2.4 is defined as:

$$\mathbf{F}_\sigma = \sigma\kappa(\alpha)\nabla\alpha \tag{2.21}$$

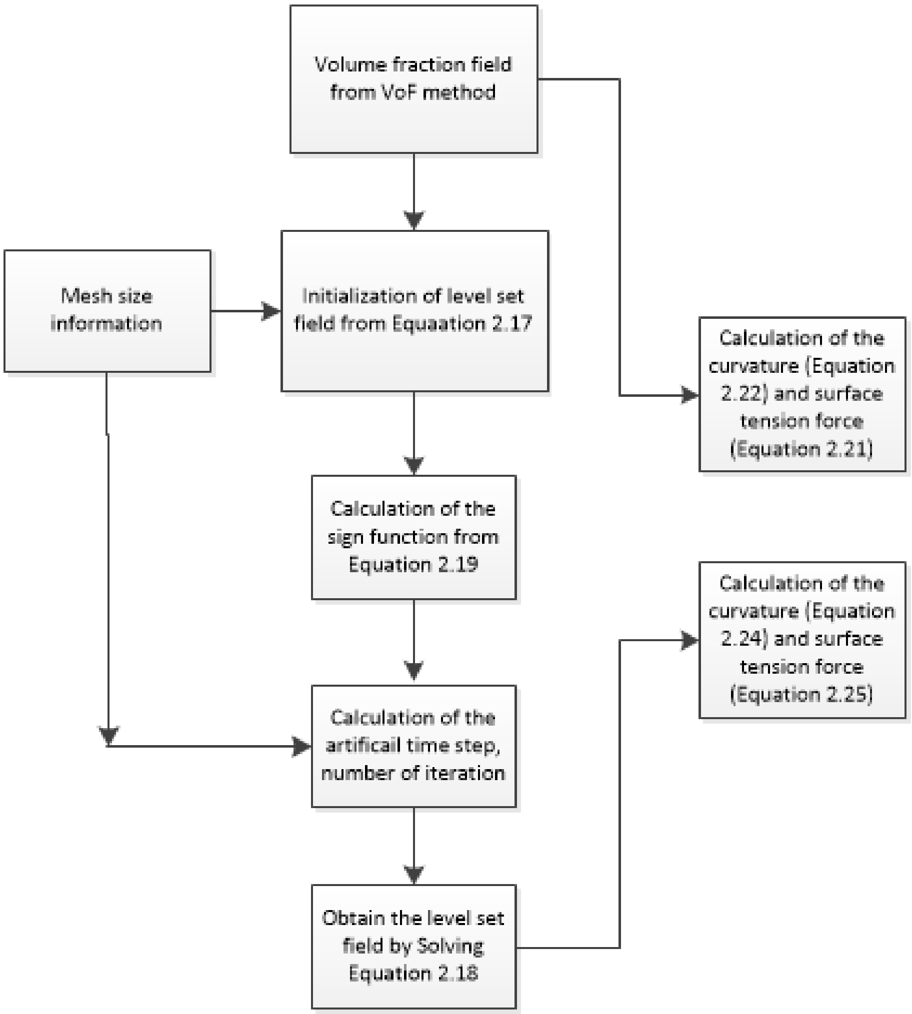

Figure 2.2: The flow chart of CLSVOF method.

where σ is the surface tension coefficient, κ is the interface curvature, which represents the magnitude of the interface normal flux at a specific face of the cell. The curvature indicates the direction of this flux calculated as

$$\kappa = -\nabla \cdot (\mathbf{n} \cdot \mathbf{S_f}) \tag{2.22}$$

where $\mathbf{S_f}$ is the surface vector of the cell face, f stands for the cell face. $\mathbf{n}$ is the unit interface normal which is calculated based on α and refers to the direction of the phase field changes in the numerical domain:

$$\mathbf{n} = \frac{\nabla\alpha}{|\nabla\alpha|} \tag{2.23}$$

For the CLSVOF method, the surface tension force is calculated based on the level set function, which can improve the accuracy of interface curvature calculation,

$$\kappa(\varphi) = -\nabla \cdot \frac{\nabla\varphi}{|\nabla\varphi|} \tag{2.24}$$

So the surface tension force can be calculated as,

$$F_\sigma = \sigma\kappa(\varphi)\delta(\varphi)\nabla\varphi \tag{2.25}$$

Where $\delta(\varphi)$ is the Dirac function used to limit the influence of the surface tension to a narrow region around the interface, which is defined as

$$\delta(\varphi) = \begin{cases} 0 & \text{if} \quad |\varphi| > \epsilon \\ \frac{1}{2\epsilon}(1 + \cos(\frac{\pi\varphi}{\epsilon})) & \text{if} \quad |\varphi| \leq \epsilon \end{cases} \tag{2.26}$$

All the adjusting parameters in the CLSVOF method are calculated based on the recommended value in [75]. The code implementation of the surface tension is in the Appendix B.

2.4 Phase Change Models

The volumetric mass source term $\dot{m}_v$ in Equation 2.3 is calculated from the phase change models. In this work, two different phase change models are evaluated, which are the Lee model [78] and the Tanasawa model [82]. The assessment of the phase change model is shown in Chapter 6.

2.4.1 Lee Model

In the Lee model, the phase change is driven by the deviation of the interfacial temperature from the saturation temperature T_{sat}. The phase change rate is propotional to the deviation $(T - T_{sat})$. The mass transfer is considered to occur at constant pressure in a quasi-thermo-equilibrium state. The volumetric mass transfer is calculated as:

$$\begin{aligned} \dot{m}_v = -\dot{m}_l = L\alpha_g\rho_g\frac{T - T_{sat}}{T_{sat}} \quad \text{for} \quad \text{condensation} \quad (T < T_{sat}) \\ \dot{m}_v = -\dot{m}_l = L\alpha_l\rho_l\frac{T - T_{sat}}{T_{sat}} \quad \text{for} \quad \text{evaporation} \quad (T > T_{sat}) \end{aligned} \tag{2.27}$$

where L is an empirical coefficient called the mass transfer intensity factor [77] with dimensions of s^{-1}. There is a great variability in the choice of the L value, ranging from 0.1 to $1 \times 10^7 \mathrm{s}^{-1}$ [77]. The determination of L depends on many factors, such as the specific phase-change phenomenon, flow rate, mesh size, time step and so on. In this work, the determination of L in OpenFOAM v1806 is studied later in Chapter 6.

2.4.2 Tanasawa Model

The Tanasawa model [82] is simplified from the Schrage model [81], in which the kinetic theory of gases based on Hertz-Knudsen equation [98] is used. In the Schrage model, it is assumed that the vapor and liquid are in saturation state except that the jump in temperature and pressure across the interface is allowed. The flux of molecules crossing the interface during phase change is connected to the temperature and pressure of the phases by the kinetic theory of gases. A fraction (γ) is adopted to represent the number of molecules changing phase across the interface, and $(1 - \gamma)$ the fraction reflected [77].

γ_c and γ_e are defined as [77]:

$$\begin{aligned}\gamma_c &= \frac{\text{number of molecules absorbed by liquid phase}}{\text{number of molecules impinging on liquid phase}} \\ \gamma_e &= \frac{\text{number of molecules transferred to vapor phase}}{\text{number of molecules emitted from liquid phase}}\end{aligned} \tag{2.28}$$

Then the volumeric mass flux is calculated from the difference between the liquid-to-vapor and vapor-to-liquid mass fluxes,

$$\dot{m} = \frac{2}{2-\gamma_c}\sqrt{\frac{M}{2\pi R}}\left[\gamma_c \frac{p_g}{\sqrt{T_{g,sat}}} - \gamma_e \frac{p_f}{\sqrt{T_{f,sat}}}\right] \tag{2.29}$$

where R is the universal gas constant, M is the molecular weight, p_g (p_f) and $T_{g,sat}$ ($T_{f,sat}$) are the vapor (liquid) pressure and saturation temperature at the interface. Usually, it is considered that $\gamma_c = \gamma_e$.
The Clapeyron-Clausius equation, which relates the pressure to the temperature for the saturation condition, is:

$$\frac{dp}{dT} = -\frac{h_{fg}}{T(\rho_l^{-1} - \rho_g^{-1})} \tag{2.30}$$

Using above equation, Equation 2.29 becomes:

$$\dot{m} = \frac{2\gamma}{2-\gamma}\sqrt{\frac{M}{2\pi R}T_{sat}}h_{fg}\frac{\rho_g \rho_l}{\rho_l - \rho_g}\frac{(T - T_{sat})}{T_{sat}} \tag{2.31}$$

Tanasawa [82] suggested that, the mass flux is linearly dependent on the temperature jump between the interface and the vapor phase. Based on this simplification, Equation 2.29 becomes:

$$\dot{m} = \frac{2\gamma}{2-\gamma}\sqrt{\frac{M}{2\pi R}}\left[\frac{\rho_g h_{fg}(T - T_{sat})}{T_{sat}^{3/2}}\right] \tag{2.32}$$

Marek and Straub [99] recommended $\gamma = 0.1 - 1$ for jets and moving films, and below 0.1 for stagnant liquid surfaces. In this work, we will determine

γ by comparing to the experimental data of bubble condensation in Chapter 6.

Chapter 3

Isothermal Bubble Rising: Path Instability

In this chapter, the path instability of an air bubble rising in quiescent water is numerically analyzed. The path instability, coupling the bubble shape, path and wake, has been widely studied due to its complexity. However, this problem is still not resolved and many aspects are unclear. In this chapter, the following problems are solved: 1) the validation of the incompressible, isothermal, two phase flow solver; 2) the mechanism of the bubble wobbling motion, including the shape oscillation, path instability, vorticity and forces; 3) the interaction of two in-line bubbles.
The contents in this chapter have been published by the author in Physics of Fluids [100].

3.1 Validation of the Solver

3.1.1 2D Bubble Rising

Hysing et al. [101] proposed two benchmark test cases for quantitative validation of different numerical schemes, which have been adopted by many researchers [102, 103]. In this part, these two cases are used to validate the solver. The initial configuration consists of a circular bubble of radius

$r_0 = 0.25\,\mathrm{m}$ centered at $(0.5\,\mathrm{m}, 0.5\,\mathrm{m})$ in a $1\,\mathrm{m} \times 2\,\mathrm{m}$ rectangular domain. The physical properties of the bubble and surrounding fluid are listed in Table 3.1. The no-slip boundary condition is applied at the top and bottom boundaries while a free slip conditions is used on the vertical walls. The computations were performed on a regular hexahedron mesh with a mesh size of $h = 1/160$. According to [75], the first-order Euler scheme was used for time discretization with time step $\Delta t = 1 \times 10^{-4}$ s and a maximum Courant number (Co) $Co = 0.05$.

Table 3.1: Physical properties of the bubble and surrounding fluid for the test cases

Test case	ρ_1 (kg/m^3)	ρ_2	μ_1 (Pa $\cdot$ s)	μ_2	g (m/s^2)	σ (kg/s^2)
1	1000	100	10	1	0.98	24.5
2	1000	1	10	0.1	0.98	1.96

Similar bubble shapes are observed compared to the results in Hysing et al. [101] shown in Figure 3.1. Furthermore, for quantitative validation of the solver, the same benchmark quantities in [101] are adopted, which are:

- Centre of mass, position over time in the vertical axis:

$$\mathbf{x}_{cm} = (x_{cm}, y_{cm}) = \frac{\int_{\alpha<0.5} \mathbf{x} dS}{\int_{\alpha<0.5} dS} \tag{3.1}$$

  where $\mathbf{x}$ represents the position, $\mathbf{x} = (x, y)$ and dS is a surface infinitesimal. $\alpha < 0.5$ means the volumetrix cells inside the gas bubble.

- mean rise velocity (MRV):

$$\mathbf{u} = \frac{\int_{\alpha<0.5} \mathbf{U} dS}{\int_{\alpha<0.5} dS} \tag{3.2}$$

  where $\mathbf{U}$ is the instant velocity at a particular point

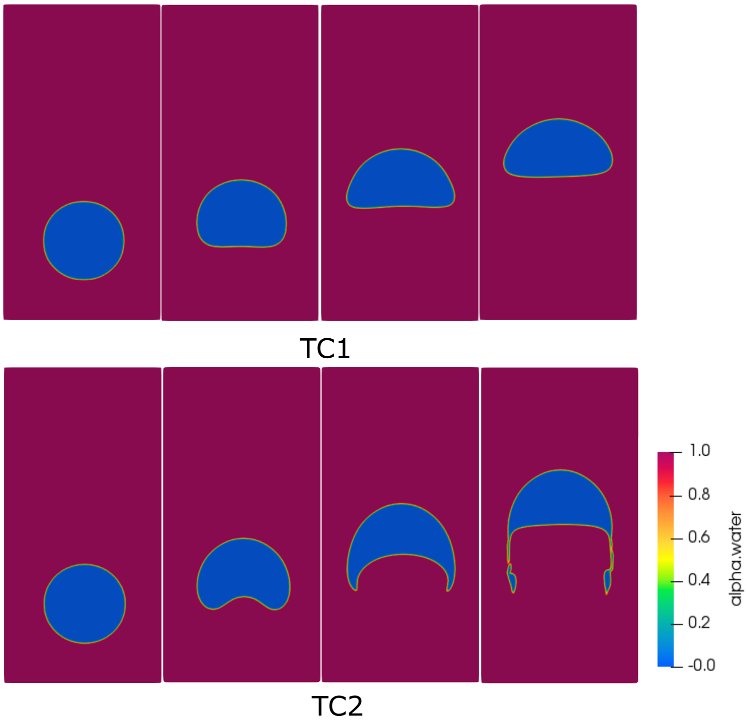

Figure 3.1: The bubble shape evolution of test cases at different time instants (h=1/160).

- Circularity, defined as the ratio of the perimeter of an area-equivalent circle by the actual perimeter of the bubble:

  $$c = \frac{\pi d_{eq}}{\int_{\Gamma} dx} \tag{3.3}$$

  where d_{eq} denotes the diameter of area-equivalent circle, Γ is a curve defined by the interface between water and air in a two-dimensional case.

The quantitative results obtained by the simulation agree well with those in [101] (Figure 3.2 and 3.3). The comparison of all the benchmark quantities, including circularity, MRV and vertical bubble position (Z), between the present simulation results and Hysing et al [101] is shown in Figure 3.2 and 3.3, where the accuracy of the present solver is confirmed.

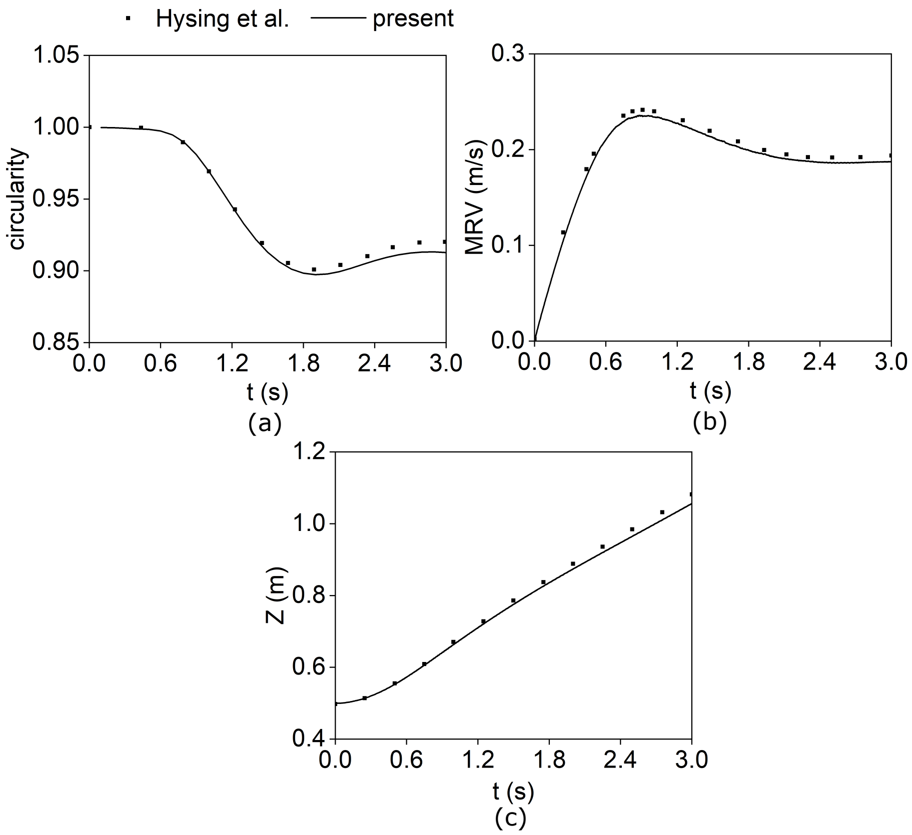

Figure 3.2: Quantitative validation of TC1 with (a), circularity, (b) MRV and (c) center of mass.

3.1.2 3D Bubble Rising

The skirted bubble in region II from the experimental results of Sharaf et al. [3] is chosen for the validation of the 3D bubble rising in quiescent liquid and the parameters are displayed in Table 3.2. The fluid domain of a cuboid with 6d × 6d×15d is adopted here for the simulation of a bubble rising, where d is the bubble diameter. A structured hexahedral mesh is used for the simulations. Atmospheric and wall boundary conditions are set for the top and bottom boundaries, while slip boundary conditions are used on the cuboid wall. Three sets of mesh sizes are used and the simulation results are compared to the experiments in Figure 3.4 and the time step is set to $\Delta x/10$ s. Z_{tip} is the bubble-tip position normalized with the equivalent radius of the

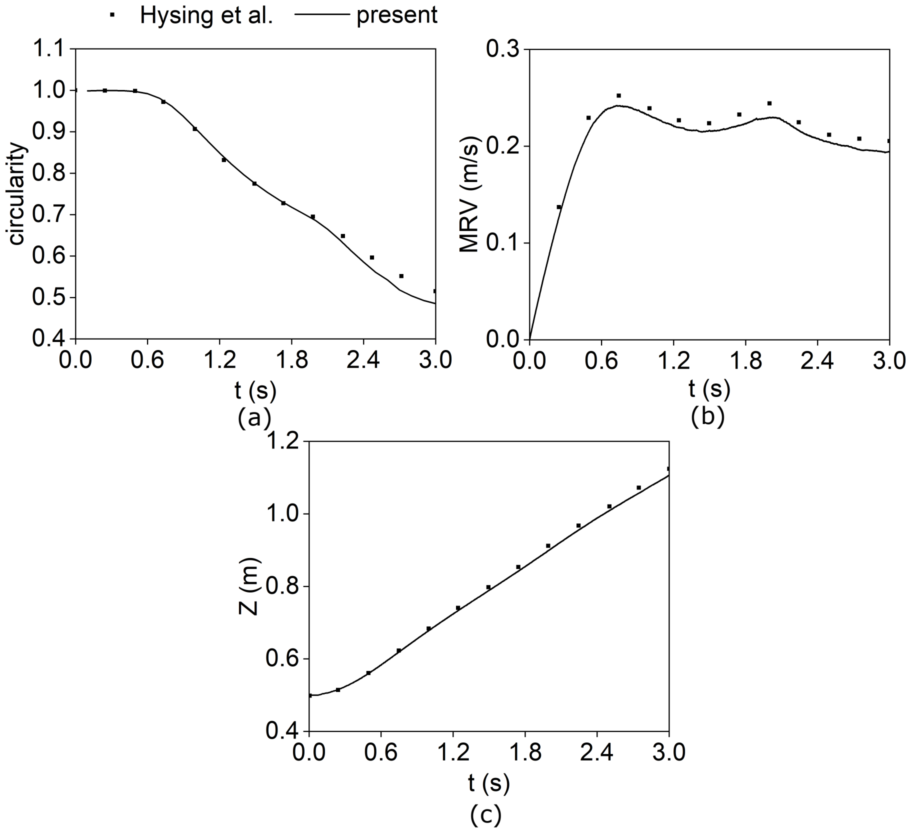

Figure 3.3: Quantitative validation of TC2 with (a), circularity, (b) MRV and (c) center of mass.

bubble and the dimensionless time t^* is normalized with $\sqrt{R/g}$, where R is the bubble radius and g is the gravity acceleration. From Figure 3.4, we can see that the result of mesh size d/20 is already converged. The comparison of the bubble shape evolution between the present numerical results and the experimental results is shown in Figure 3.4, which displays a good agreement. Further tests were conducted to assess the influence of the time step on the bubble rise velocity as shown in Table 3.3. Every time step value yields similar results and the relative differences are all around 0.1%-0.2%. So the time step $\Delta x/10$ s is chosen and the switch to Courant number 0.1 is also switched on for all the following simulations.

Table 3.2: The physical parameters of skirted bubble in the work of Sharaf et al. [3]

	ρ (kg/m^3)	μ (mPa s)	σ (kg/s^2)	Eo	Ga
liquid	1254	967.8	0.0624	73.28	10.86
gas	1	0.0151			

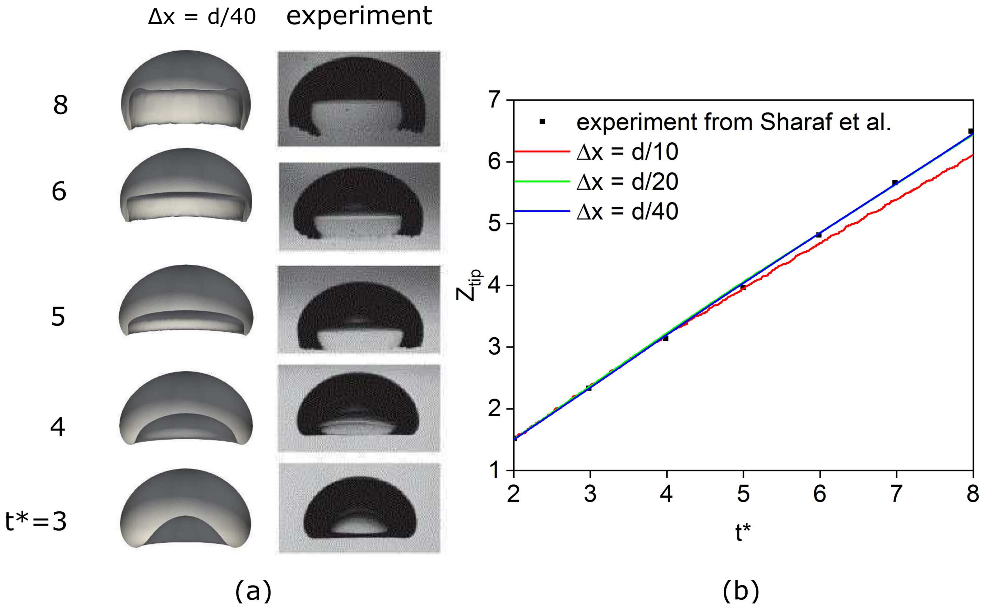

(a) (b)

Figure 3.4: (a) Comparison of the bubble shape evolution between experimental [3] and present numerical results. (b) Comparison of the temporal variation of Z_{tip} obtained from different mesh size and the experimental results.

Table 3.3: Convergence analysis of time step discretization for skirted bubble

Grid Size	Time Step (s)	Terminal Velocity (m/s)
d/40	1×10^{-5}	0.29021
d/40	5×10^{-5}	0.28994
d/40	$\Delta x/10$	0.2896
d/40	Counrant (0.1)	0.28968

Table 3.4: The physical properties of the two phases.

phase	ρ (kg/m^3)	μ (mPa s)	σ (kg/s^2)
water	998	1	0.073
air	1.2	0.0151	

Table 3.5: The setting of boundary conditions.

boundary	volume fraction	pressure	velocity
bottom wall	zeroGradient	fixedFluxPressure	fixedValue (0 0 0)
top wall	inletOutlet	totalPressure	pressureInletOutletVelocity
side walls	zeroGradient	zeroGradient	slip

3.2 Numerical Analysis of Path Instability

3.2.1 Numerical Setting

The numerical domain for the simulation of the rising bubble with path instability is a cuboid fluid domain with a size of $6d \times 6d \times 50d$ m^3 (d is the bubble diameter) filled with water. Atmospheric and wall boundary conditions are applied on the top and bottom boundaries while slip boundary conditions are used for all the vertical walls (Table 3.5). The bubble is initially located at $1.5d$ above the bottom wall. The physical properties of the two phases are listed in Table 3.4. All the computations are performed on a structured hexahedral mesh. According to Albadawi et al. [75], the transient terms are discretized using a first order implicit Euler scheme. For spatial discretization, we use the second order scheme, which is listed in Table 3.6 [104].

Table 3.6: The discretization schemes used in the present study.

Term	Discretization scheme
$\nabla \cdot \rho \mathbf{U}\mathbf{U}$	Gauss limited linear scheme
$\nabla \cdot \mu \nabla(\mathbf{U})$	Gauss linear
$\nabla \cdot (\alpha \mathbf{U})$	Gauss vanleer01
interpolation face value	Linear interpolation

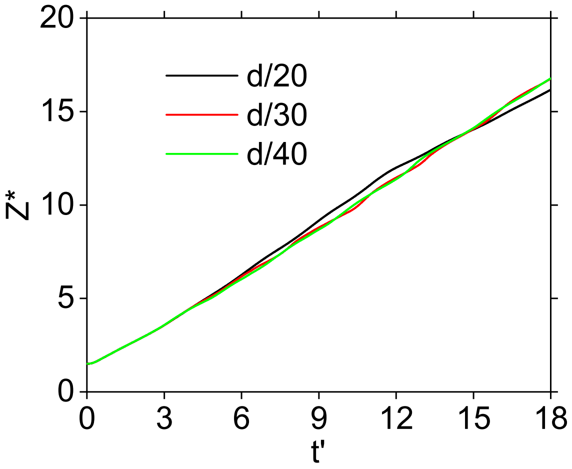

Figure 3.5: The mesh independence study for the path instability.

3.2.2 Mesh Independence Study

To simulate the path instability, the interface and the wake structure must be fully resolved, which are dependent on the mesh resolution. Thus a mesh independence study should be conducted. In this section, the mesh sizes used are $\Delta x = d/[20, 30, 40]$. The time step is set as $\Delta x/10$ and the Courant number is 0.5. The bubble diameter is 0.008 m.

The results of the center of mass for different mesh sizes are shown in Figure 3.5. The center of mass is made dimensionless with the bubble diameter ($Z^* = Z/d$) and the dimensionless time is normalized with $t' = t/\sqrt{d/g}$. From Figure 3.5, we can see that the results for the mesh size $d/30$ are already converged. In consideration of the work of Tripathi et al. [4] and Zhang and Ni [105], the mesh size of $d/32$ is used for all the following simulations in this chapter. Then the terminal velocity (V_t) and aspect ratio (E) from our simulation results are compared to the experimental data of Liu et al. [7], which is shown in Table 3.7. The terminal velocity is obtained when the bubble rising velocity reaches a constant value. The bubble rising velocity is defined as:

$$V = \frac{\int_{\alpha<0.5} \mathbf{U} dV}{\int_{\alpha<0.5} dV} \tag{3.4}$$

Where **U** is the instant vertical velocity in a particular cell. The aspect ratio is calculated as $E = d_Z/\sqrt{d_X d_Y}$, where d_X, d_Y are the major axes of the bubble and d_Z is the minor axis. The relative errors of V_t and E are 1.4% and 8.3%, which supports the validity of the current numerical approach and mesh resolution.

Table 3.7: Comparison of the terminal velocity and aspect ratio with the experimental data [7]

	V_T (m/s)	E
simulation	0.209	0.55
experiment	0.212	0.6

3.3 Results

3.3.1 Mechanism of the Path Instability

In this section, the mechanism of the path instability is elucidated with the validated case in last Section. The trajectory of the bubble is displayed in Figure 3.6. The hydrodynamics of a single bubble with path instability is highly relevant to the bubble shape deformation, wake development and the transverse forces exerted on the bubble [106], which are analyzed in the following sections.

The temporal variations of the rising velocity and aspect ratio are shown in Figure 3.7. The velocity is made dimensionless with $V^* = V/\sqrt{gd}$ [107] due to the high Re (≈ 2000, see below). Before the analysis of the path instability, the velocity oscillation appeared in Figure 3.7 (a) is first examined as we think it promotes the formation of the asymmetric vortex in the rear of the bubble, which contributes to the occurrence of the path instability. Once the air bubble is released in the water, it rises due to the buoyancy and a boundary layer around the bubble is formed. The water motions are completely driven by the bubble rise. Due to the interaction of inertia and surface tension force, the bubble wobbling is observed as shown in Figure

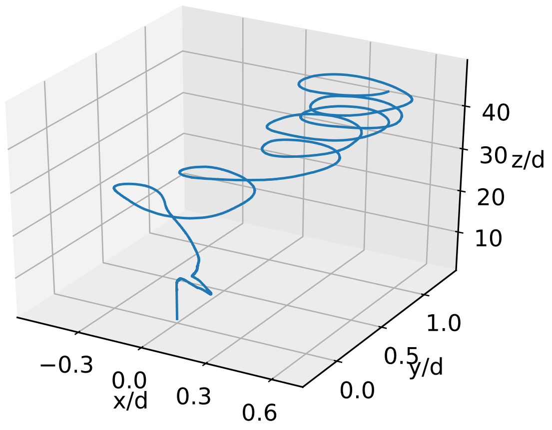

Figure 3.6: The rising path of the bubble in the computation domain.

3.7 (b). We think that the bubble wobbling has two roles: (1) the excessive curvature speeds up the separation of the boundary layer; (2) the velocity peaks (high Re) results in the formation of asymmetrical vortices. The maximum velocity can reach 1.26 at t'=8, corresponding to the $Re \approx 2000$. Then the vortices are not formed symmetrically at some point and different lift forces develop on each side of the bubble, which results in the bubble motion transverse to the flow.

As a further analysis, we calculate the bubble movement, the vorticity accumulated on the bubble surface, the lift force and viscous force exerted on the bubble (all in X and Y directions), which is shown in Figure 3.8. Then the hydrodynamics of the rising bubble with path instability are analyzed. The vorticity components in X and Y directions accumulated on the bubble surface are calculated as $\tau_{(X,Y)} = \int_s \omega_{(X,Y)} dS$, where S is the bubble interface and $\omega_{X,Y}$ is the vorticity component in X and Y direction. The lift force is calculated as $F_{(X,Y)} = \int_s p \cdot \mathbf{n}_{(X,Y)} + \tau_{(X,Y)} dS$, where p is the pressure, $\mathbf{n}_{X,Y}$ is the bubble surface normal direction, and $\tau_{X,Y}$ is the viscous force. We can observe that the oscillation frequencies (6Hz, St=0.22) of the bubble movement, the vorticity accumulated on the bubble surface, the lift force and

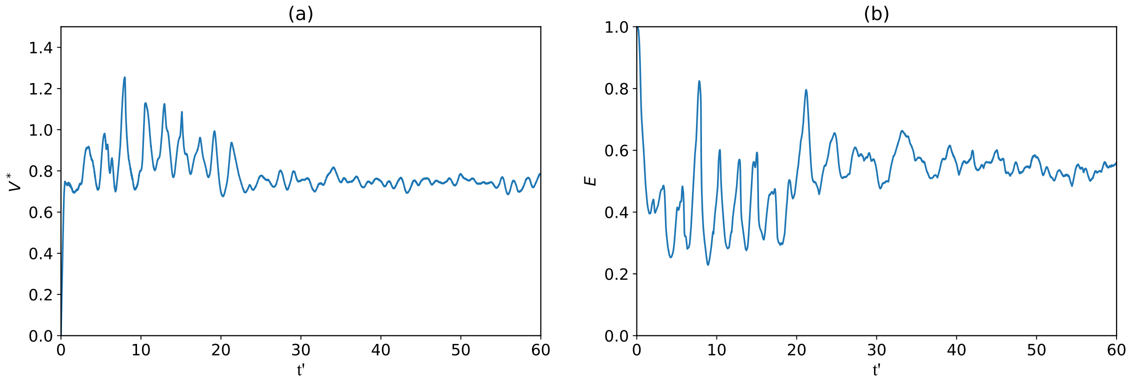

Figure 3.7: The temporal variations of a) the terminal velocity, and b) aspect ratio.

viscous force are the same. In the straight path, the oscillation amplitude of these variables are all 0, which means a symmetric flow field. After t'=8 ($V^* = 1.26$), the forces exerted on the bubble seem to oscillate firstly, earlier than that of the bubble movement and the vorticity. Afterwards, the accumulated vorticity on the bubble surface seems to oscillate followed by the horizontal bubble movement. Therefore, after the pressure loses symmetry, the vorticity and bubble movement begin to oscillate, which means the happening of the path instability. Compared to the contribution of the pressure, the influence of the viscous force (10^{-6}) on the path instability is negligible due to the large Re.

Figure 3.9 shows the bubble shape evolution and the vortex structures during the wobbling. We can observe that the bubble wobbling mainly manifest in the vertical length variation of the bubble in Figure 3.9 (b). The longest vertical length (t'=8 and t'=10.5) corresponds to the velocity maxima. As discussed in our previous paper [5], the liquid jet in the rear of the bubble with higher velocity than the bubble rising velocity, resulting from the pressure difference between the top and bottom of the bubble, can "push" the bubble and increase the bubble rising velocity. In the meantime, the liquid jet can also compress the bubble (can not penetrate the bubble due to the surface tension force), decreasing the vertical length of the bubble, thus de-

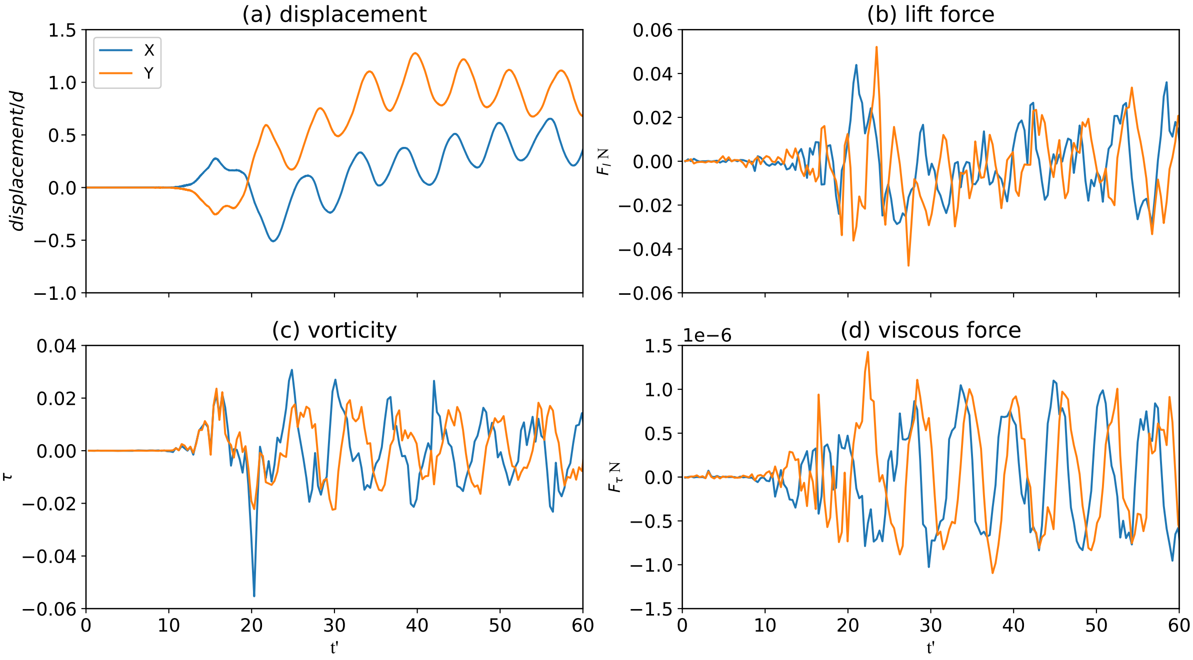

Figure 3.8: The time history of (a) the displacement of the bubble, (b) lift force, (c) the vorticity accumulation on the bubble surface, and (d) viscous force in X and Y direction.

creasing the liquid jet velocity. Here we use the Q criterion [108] to identify the pure rotational motion in the liquid. The vortex structures revealed by Q criterion during the bubble wobbling are shown in Figure 3.9 (a). In Figure 3.9 (a), we carefully tune the Q values and the hairpin structures are observed. In classic wall turbulence flows, hairpin vortices are widely studied as an important structural aspect. The hairpin structures control the turbulent motions by the parent-offspring mechanism by generating a series of hairpins one after another [109]. As the bubble rises, a toroidal vortex ring is formed on the bubble surface ahead of the maximum diameter plane and develops further to the rear side of the bubble. At the stagnation point in the rear side of the bubble, a low pressure zone is created and the hairpin structures appear in the flow [110]. The hairpin legs are still attached to the bubble while the legs point downwards. Four hairpin legs can be observed in our simulation. With the bubble wobbling, more hairpin vortices are generated and interact with each other, which forms a flower-like structure. The flower-like structure bursts with the bubble wobbling and ejects small scale liquid motions.

Here we also display the wake structures of the rising bubble in the spiral motion after t'=20 (Figure 3.10). At t'=20, the legs of the old hairpin vortex are still attached to the rear bubble surface. At the same time, new hairpin vortices are also formed . At t'=60 in the fully developed spiral motion, the hairpin vortices are observed in the spiral path induced by the rising bubble. Many hairpin structures are tilted and interacted with one another. The occurrence of the path instability is also related to the shape oscillations in addition to the bubble wake. We analyzed the bubble movement in Y direction and found that the oscillation frequency of the aspect ratio E (d_Z/d_Y) is twice of that of the bubble movement in Y direction. Actually, the shape oscillation of the bubble is considered to be of an effect of the path instability, caused by the uneven pressure distribution about the equatorial plane of the bubble during the spiral motion.

As the bubble rises, energy is transferred from the bubble to the liquid

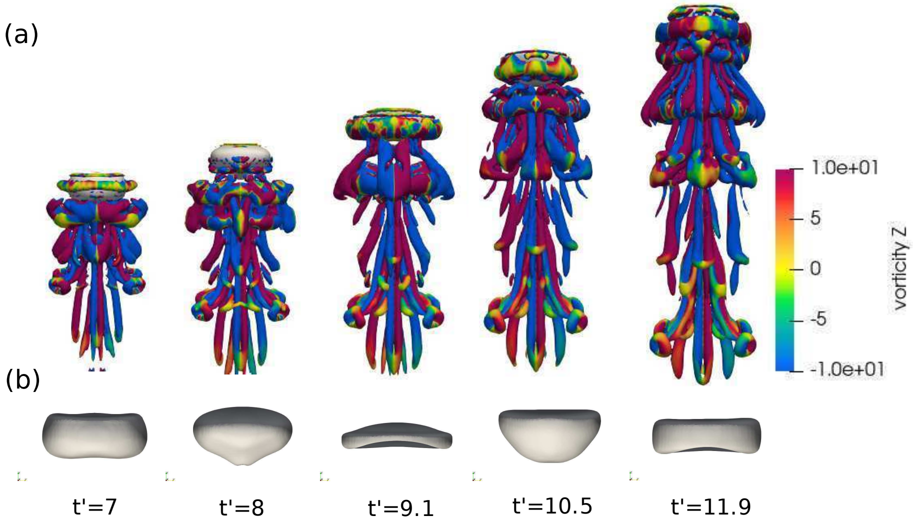

Figure 3.9: (a) The vortex structures revealed by Q criterion (Q=10), and (b) the bubble shape at different time instants. The iso-vortices are colored with ω_z.

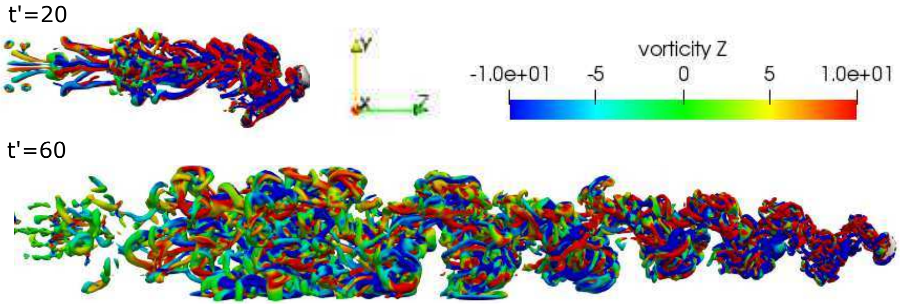

Figure 3.10: The vortex structures extracted using the Q criterion (Q=10) at t=20 and t=60.

phase, generating a wide range of small and large scale of motion which may also create turbulent motion (bulk generated turbulence) [106]. Thus it is necessary to measure the momentum and kinetic energy received by the liquid phase. Here the agitation created in the liquid is quantified with the volume-averaged velocity fluctuation [110], $<\mathbf{u}>=\int_V mag(\mathbf{u})dV$, where $\mathbf{u}$ is the velocity vector in the liquid phase and V is the total liquid volume. The dimensionless volume-averaged total kinetic energy per unit mass in the liquid is calculated as, $\kappa_w = (u_x^2 + u_y^2 + u_z^2)/V_b^2$. The components of the volume-averaged liquid velocity and the dimensionless volume-averaged kinetic energy are shown in Figure 3.11. We can observe that the velocity fluctuations in vertical direction are more intense than that in the lateral direction, all of which present linear increase until t'=55. After that the velocity fluctuates around a stable value. From Figure 3.11 (b), the dimensionless kinetic energy presents a quadratic increase until t'=55 and after that it fluctuates around a stable value.

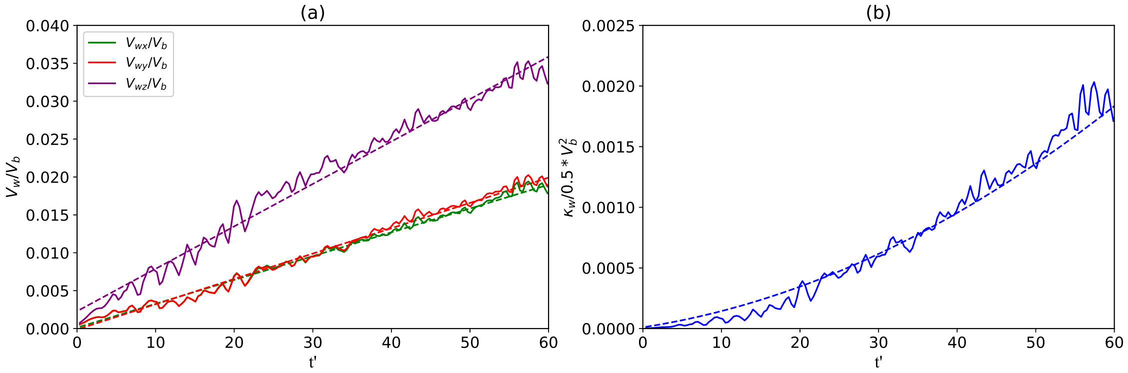

Figure 3.11: The time history of (a) the volume-averaged liquid velocity, and (b) the dimensionless liquid kinetic energy.

3.3.2 Two inline bubbles with path instability

In this section, we simulate and analyze the wobbling motion of two inline bubbles. When the bubble-wake interaction happens in different positions of the bubble rising path, the rising bubble dynamics will be different. There-

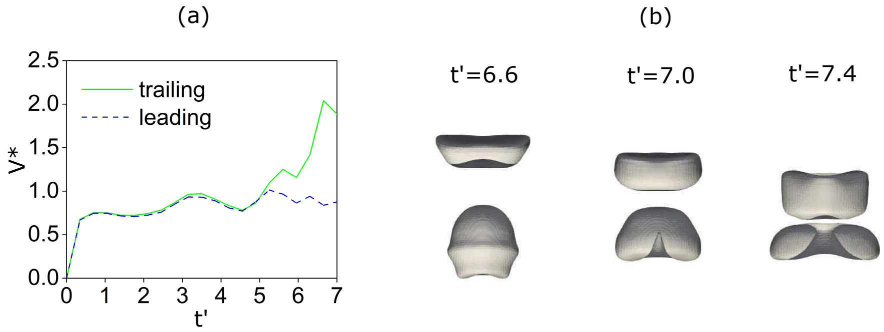

Figure 3.12: a) The time history of the rising velocity of the two bubbles with $h = 2d$, b) the bubble shape evolution.

fore, we simulate three cases: 1) $h = 2d$ (h is the distance of the leading and trailing bubble center); 2) $h = 4d$; 3) $h = 6d$. However, the bubble coalescence is not the objective of the present research and we only investigate the bubble-wake interaction before the coalescence.

3.3.2.1 $h = 2d$

For case 1 ($h = 2d$), the two bubbles interact mainly in the straight rising path. The rising velocity of the two bubbles and the shape evolution are shown in Figure 3.12. Before t'=5, trailing bubble (TB) and leading bubble (LB) rise with the same velocity since TB has not interacted with the wake flow of LB. After t'=5, TB enters into the wake region created by LB. We can observe the velocity increase of TB due to the added mass effect from t'=5 to the coalescence of the two bubbles as shown in Figure 3.12 (a). The approach of the two bubbles is displayed in Figure 3.12 (b). TB is elongated at t'=6.6 as it approached LB. Based on the discussion in [111] and [38], this phenomenon is caused by the shielding effect of the wake flow behind LB. Because of the elongation of TB, the velocity of the liquid jet caused by the pressure difference between the top and bottom of TB [5] becomes larger, resulting in the central breakup of TB (at t'=7.4 in Figure 3.12 b).

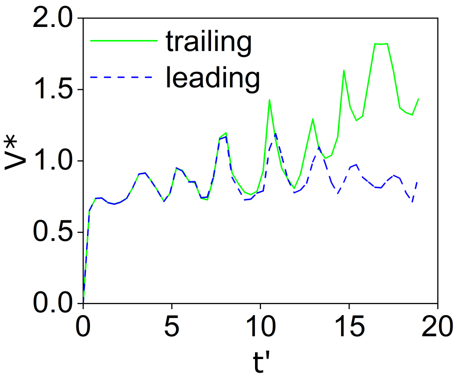

Figure 3.13: The time history of the rising velocity of the two bubbles with $h = 4d$.

3.3.2.2 $h = 4d$

For case 2 ($h = 4d$), the two bubbles interact in the straight rising path and the transition phase. We plot the rising velocity of the two bubbles in Figure 3.13. From t'=0 to t'=10 in the straight rising path, the rising velocities of the two bubbles are almost the same, meaning no interplay of the two bubbles. From t'=10 to t'=14, the velocities of the two bubbles are still oscillating due to the bubble wobbling. But the velocity of TB is slightly higher than that of LB. Therefore, the bubble wobbling caused by the interaction of inertia force and the surface tension force dominates in this period compared to the interaction of the two bubbles. From t'=14 to t'=20 (bubble coalescence), the rising velocity of TB is comparatively higher than that of LB. In this period, the interaction of TB with the wake flow of LB plays a more important role in the bubble motion. However, the velocity oscillation can still be observed and oscillation amplitude ($\Delta V = 0.5$) of TB is larger than that ($\Delta V = 0.2$) of LB.

We plot the evolution of the streamlines of the two bubbles in Figure 3.14. At t'=7, the two bubbles are far away from each other and they do not interplay. From t'=10, TB enters into the flow region which is affected by the rising of LB. Due to the added mass effect, TB starts to accelerate. As TB approaches LB, the vortexes generated by LB merge into the ones generated

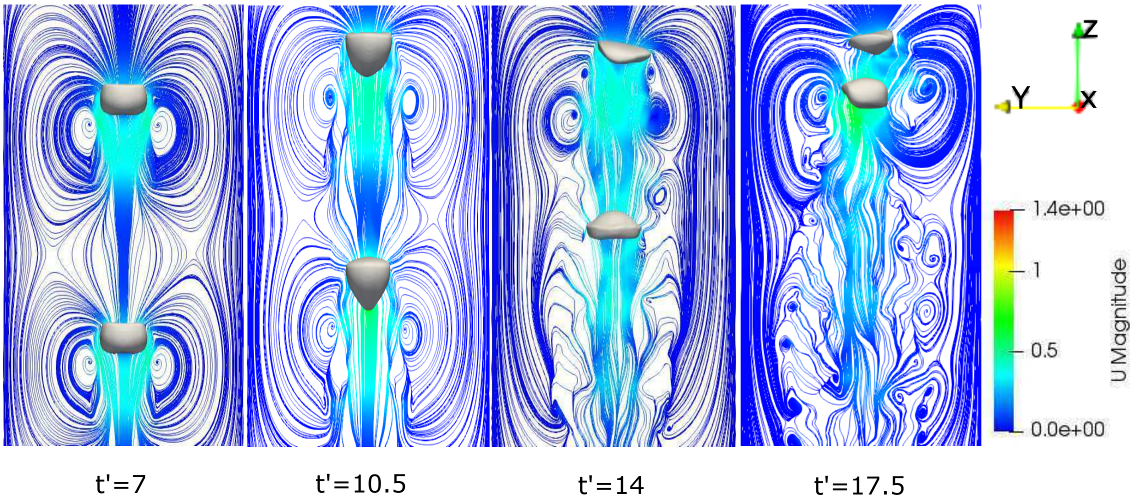

Figure 3.14: The evolution of the streamline of the two bubbles.

by TB (t'=14 in Figure 3.14). Since the distance between the TB and LB is short when they enter the path instability, the effect of the wake generated by LB on TB is not obvious and no horizontal deviation is observed for TB t'=17.5. The wake structures revealed by Q criterion during the rising of the two inline bubbles (h=4d) are displayed in Figure 3.15. At t'=7 when TB and LB do not interplay, the wake structures of the two bubbles are the same to that of a single bubble and the flower-like structures can be observed. At t'=14, TB interacts with the wake generated by LB in the straight path, which affects the rising velocity of TB as seen in Figure 3.13. At t'=17.5 before the coalescence, LB rises with path instability and the lateral motion of TB seems to be slightly delayed due to its interaction with the wake of LB. In addition, more small-scaled hairpin structures can be observed at this time due to the rising motion of TB.

3.3.2.3 $h = 6d$

For $h = 6d$, the interaction of TB with the wake generated by LB becomes more complex. Depending on the position of TB in the wake of LB and the intensity of the vortices TB encounters, the path of TB can be more or less modified. In this section, we analyze the behavior of TB in the wake of LB.

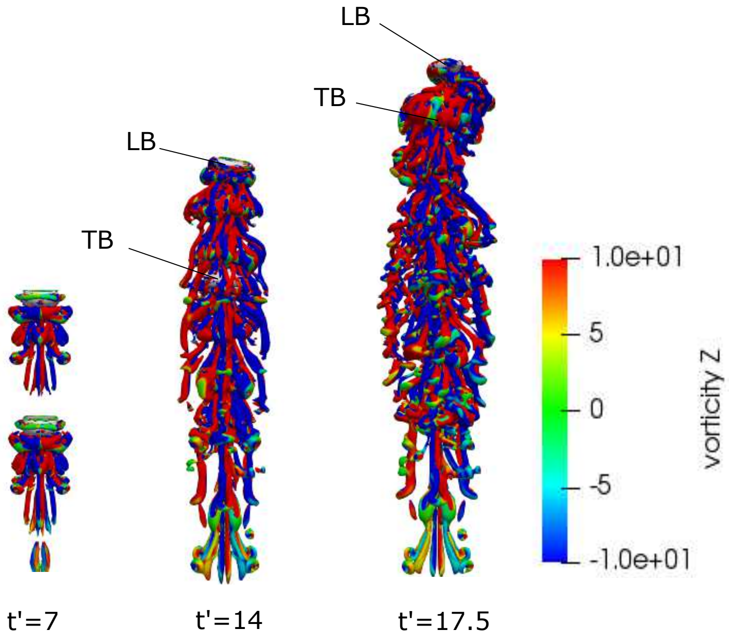

Figure 3.15: The evolution of the vortex structures revealed by Q criterion (Q=10) with h=4d.

We plot the time history of the rising velocity of the two bubbles in Figure 3.16. Before t'=12, the two bubbles rise with the same velocity. After that, the rising velocity of the two bubbles yields different tendency. The time history of LB is the same to that of a single rising bubble. But the rising velocity of TB is much affected by the wake of LB, resulting in distinct oscillations with larger amplitude. However, the average velocity of TB is still larger than that of LB because of the added mass effect from LB, which leads to the coalescence of the two bubbles in the end.

The time history of the bubble displacement and the accumulated vorticity on the bubble surface are displayed in Figure 3.17. Compared to LB, no periodicity of the displacement of TB is observed and the oscillation amplitude is larger. Due to the interaction of TB with the wake shedding from LB, τ_X and τ_Y of TB are disordered due to the position of TB in the wake of LB and the intensity of the vortices TB encounters.

The wake generated by LB can cause the lateral motion of TB, which results in the TB moving either towards the wake center or away from it [112, 113]

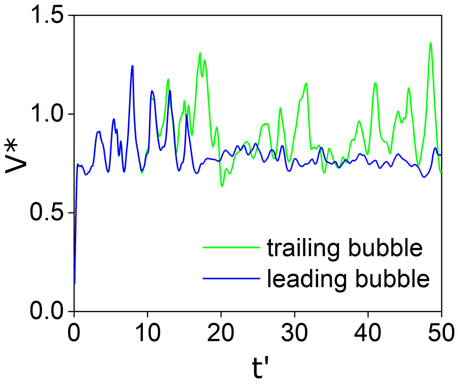

Figure 3.16: The time history of the rising velocity of the two bubbles with $h = 6d$.

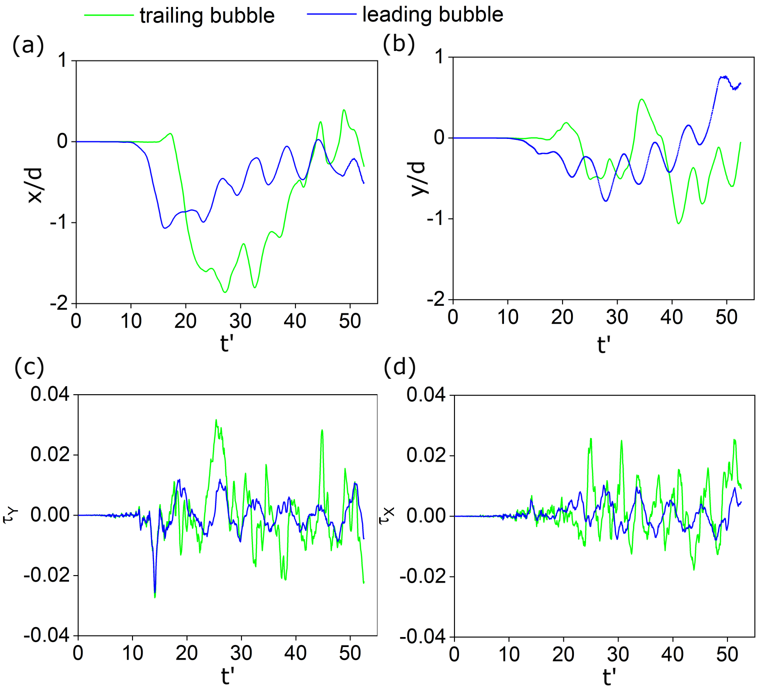

Figure 3.17: The time history of the displacement and vorticity of the two bubbles with $h = 4d$.

depending on the intensity and direction of the wake. These effects are shown in Figure 3.18 and 3.19. In Figure 3.18, TB is drifted from the center in the wake to the leftmost position at t'=28s. We can observe the horizontal drift of TB from the Figure 3.18 (a). The inertial force driving TB towards the

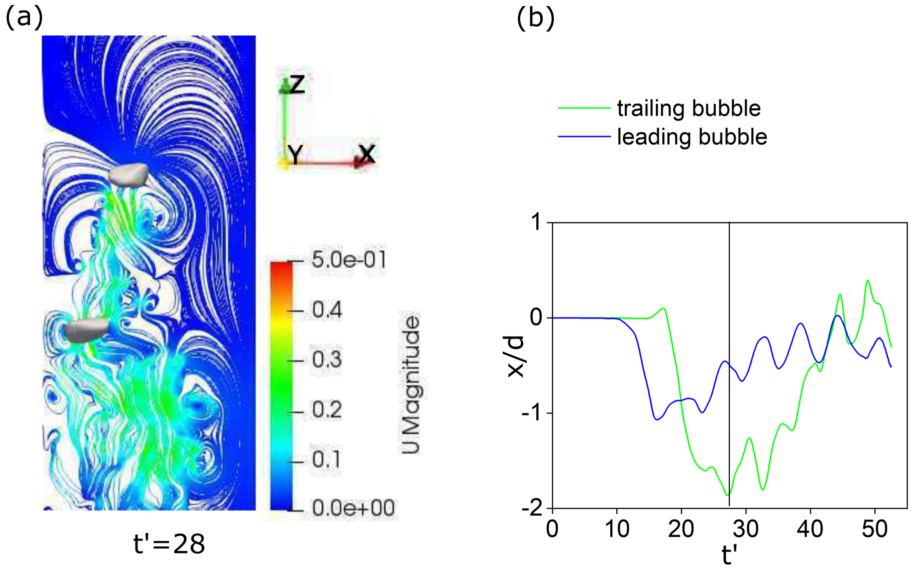

Figure 3.18: Drift away of the trailing bubble. (a) Streamlines of the velocity field at the time of ejection t'=28. (b) The time history of the bubble displacement in X direction.

vortex core is sufficient compared to the buoyancy, which means that the horizontal velocity induced by the vortex is comparable to the terminal velocity of the bubble to yield the modification of the path of TB. Here we measure the horizontal velocity V_x and terminal velocity V_Z at t'=20, which are $V_X = -0.53$ and $V_Z = 0.67$. However, for a single bubble rising, the horizontal velocity V_X is only 0.077 at this time (t'=20).

On the other hand, TB can also drift to the center of the wake, which is shown in Figure 3.19. We can observe that TB enters into the center of the wake progressively at t'=35 and t'=42. The horizontal velocity V_X and terminal velocity V_Z of TB are 0.16 and 0.80 at t'=35, respectively. The horizontal velocity V_X of a single rising bubble is only 0.09. The inertial force induced by the vortex driving TB towards the center of the wake is not big enough compared to the buoyancy since the intensity of the vortex (V1 in Figure 3.19) TB encounters is not strong. After that TB encounters the stronger clockwise rotational motion of the vortex (V2 in Figure 3.19 c) heading to the higher velocities in the ascending flux. At t'=42, the horizon-

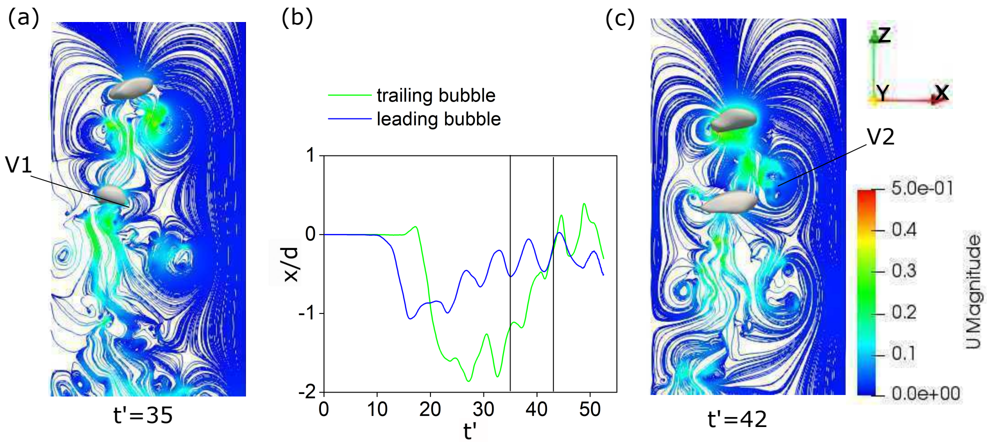

Figure 3.19: Centering of the trailing bubble. (a) Streamlines of the velocity field at the time of centering t'=35. (b) The time history of the bubble displacement in X direction. (c) Streamlines of the velocity field at the time of centering t'=42

tal velocity V_X of TB increases to 0.32. Therefore, the centering of TB is a progressive process, it slowly drifts towards the center of the wake [112].

The wake structures of the two inline bubble with h=6d are shown in Figure 3.20. We can see that the lateral motion of TB is greatly affected by the wake of LB. Depend on the direction and the strength of the vortex TB encounters, the trajectory of TB can either be towards the wake center of away from it. Due to the appearance of TB, more hairpin vortices are generated in the wake.

We also calculate the momentum and kinetic energy received by the liquid phase from the two inline bubbles. The volume-averaged velocity fluctuation and total kinetic energy are shown in Figure 3.21. Compared to the case of single bubble, the liquid volume-averaged velocity created by two inline bubbles is doubled before TB enters the wake region of LB (t'=10) and is less than the doubled value after TB enters the wake region of LB. The total liquid kinetic energy transferred from two inline bubbles is four times of that from single bubble before t'=10 and less than the four times after that due to the wake effect of the LB.

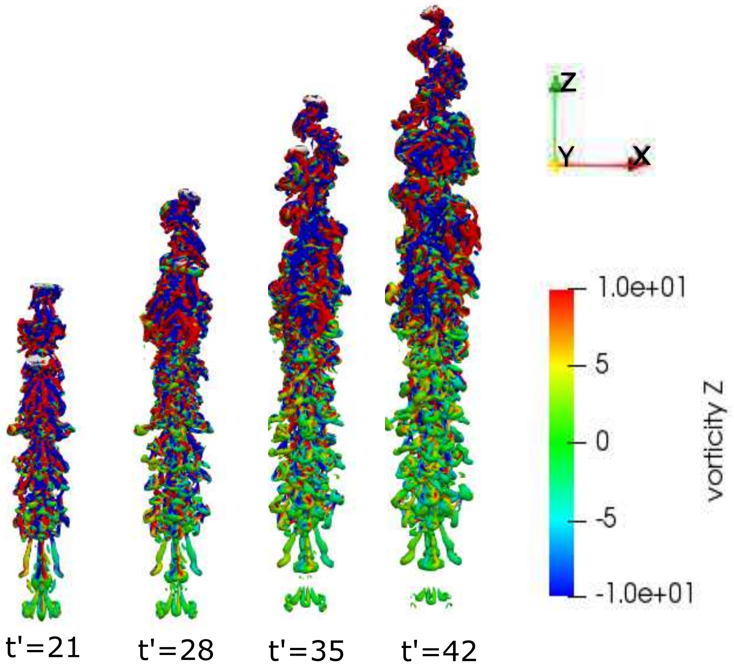

Figure 3.20: The evolution of the vortex structures revealed by Q criterion (Q=10) for two inline bubble rising with h=6d.

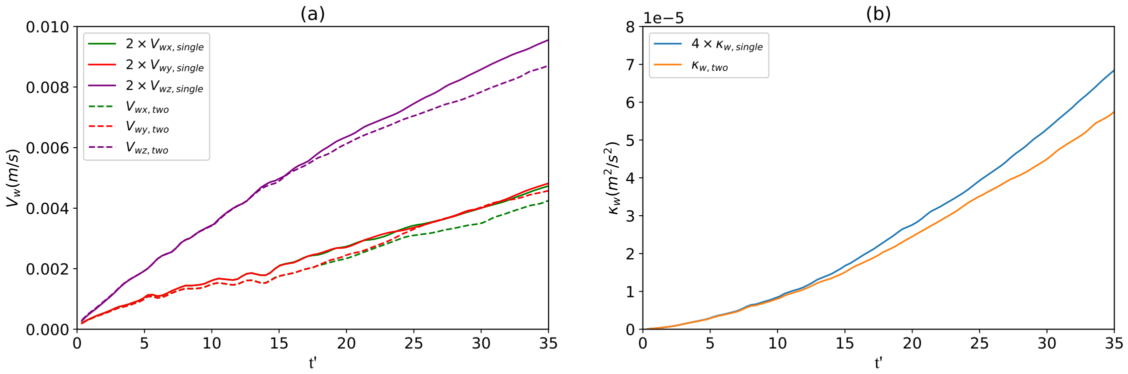

Figure 3.21: The comparison of (a) the volume-averaged liquid velocity, and (b) the dimensionless liquid kinetic energy between single and two inline bubbles.

3.4 Conclusion

In this chapter, the wobbling motions of a single and two inline bubbles rising in quiescent liquid are numerically studied via 3D simulations using

VoF method. The mechanism of the path instability of the wobbling bubble motion is analyzed. We also investigate the two bubbles rising inline with different initial distance.

The path instability is observed in the trajectory of an 8mm air bubble rising in quiescent water and the results are compared to the experimental data. The bubble wobbling has two roles: (1) the excessive curvature speeds up the separation of the boundary layer; (2) the velocity peaks (Re) result in the formation of asymmetrical vortices. The oscillation frequencies (6Hz, St=0.22) of the bubble movement,the vorticity accumulated on the bubble surface, the lift force and viscous force are the same while the oscillation frequency of the aspect ratio E is twice of that of the bubble movement. The forces exerted on the bubble seem to oscillate firstly, earlier than that of the bubble movement and the vorticity. The hairpin structures are tilted and interacted with one another during the spiral motion. The velocity fluctuations in the liquid phase in vertical direction are more intense than that in the lateral direction, all of which present linear increase while the dimensionless kinetic energy presents a quadratic increase.

For two inline bubbles, three cases are considered with the initial distance $h = [2d, 4d, 6d]$. When $h = 2d$, the terminal velocity of TB increases over time due to the added mass effect and TB collides with LB before it enters into the spiral motion. We also observe the central breakup of TB due to its elongation. When $h = 4d$, the two bubbles interact in the straight rising path and the transition phase. The same velocity oscillations are observed when TB is unaffected by LB. After that, the velocity of TB increase due to the interaction with LB and the velocity oscillation of TB is bigger than that of LB. When $h = 6d$, the distance of the two bubble is far enough that both yield path instability. The wake generated by LB can cause the lateral motion of TB (moving either towards the wake center or away from it), which depends on the position of TB in the wake of LB and the intensity of the vortices TB encounters. Compared to the case of single bubble, the liquid volume-averaged velocity created by two inline bubbles is doubled before TB enters the wake region of LB (t'=10) and is less than the doubled value after TB enters the wake region of LB. The total liquid kinetic energy transferred from two inline bubbles is four times of that from single bubble before t'=10 and less than the four times after that due to the wake effect of the LB.

Chapter 4

Isothermal Bubble Rising: Central Breakup

In this chapter, the central breakup behavior of a large bubble is discussed by conducting a fully 3D simulation of large bubbles rising in quiescent liquid. Due to the difficulty in creating a perfectly spherical large bubble in experiments, numerical investigations may shed light on this process. The incompressible two phase flow solver, InterIsoFoam, is used for all the simulations in this chapter. The detailed numerical settings are introduced in Section 4.1, including the flow domain, boundary conditions and mesh independence study. The main results are presented in Section 4.2. The hydrodynamics during the central breakup process are analyzed in detail. Different influencing factors on the central breakup behaviors are discussed. Section 4.3 is devoted to the general summary and conclusion.

The contents in this chapter have been published by the author in Physics of Fluids [5] and Chemical Engineering Science [38].

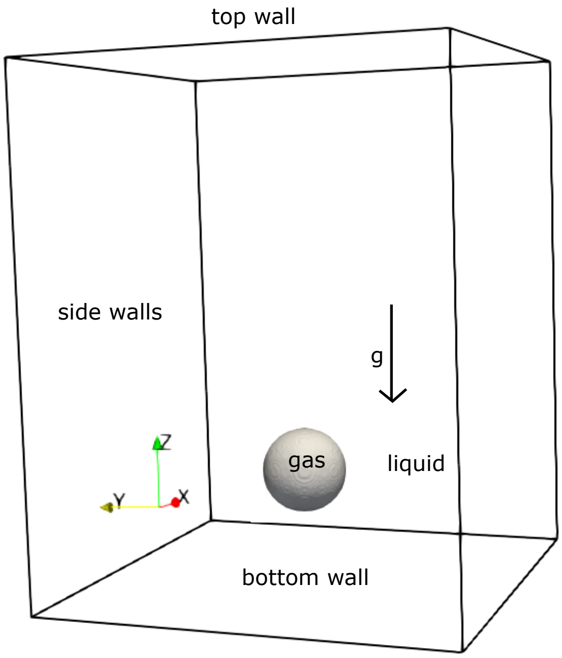

Figure 4.1: The flow domain for the simulation of central breakup.

4.1 Problem Description

4.1.1 Numerical Setting

To study a large bubble rising in quiescent liquid, a cuboid fluid domain with $6d \times 6d \times 7.5d$ (d is the bubble diameter) dimensions is adopted (Figure 4.1). The bubble center initially stands $1.5d$ above the bottom wall. The two fluids are 70% glycerol in water and air, separately. The parameters of the bubble and the liquid properties are displayed in Table 4.1. The boundary conditions for Figure 4.1 are listed in Table 4.2. All the computations are performed on a structured hexahedral mesh. The transient terms are discretized by using a first order implicit Euler scheme. In OpenFOAM, there are several spatial discretization schemes, including first (upwind) and second order schemes (linear, linearUupwind, limitedLinear). Based on the results of the solver validation in Section 3.1 we use the following second order schemes listed in Table 4.3.

Table 4.1: The physical parameters of the central breakup bubble.

	R (m)	ρ (kg/m^3)	μ (mPa $\cdot$ s)	σ (kg/s^2)	Eo	Ga
liquid		1182	57.8	0.0658	110.1	253.2
bubble	0.025	1	0.0151			

Table 4.2: The setting of boundary conditions.

boundary	volume fraction	pressure	velocity
bottom wall	zeroGradient	fixedFluxPressure	fixedValue (0 0 0)
top wall	inletOutlet	totalPressure	pressureInletOutletVelocity
side walls	zeroGradient	zeroGradient	slip

Table 4.3: The discretization schemes used in the present study

Term	Discretization scheme (OpenFOAM)
$\nabla \cdot \rho \mathbf{U}\mathbf{U}$	Gauss limited linear scheme
$\nabla \cdot \mu \nabla(\mathbf{U})$	Gauss linear
$\nabla \cdot (\alpha \mathbf{U})$	Gauss vanleer01
interpolation face value	Linear interpolation

4.1.2 Mesh Independence Study

The VoF method is capable of capturing large interface motions, but it is heavily dependent on the mesh resolution when dealing with complex topological changes. Therefore it is necessary to conduct a mesh independent study for the simulation of central breakup bubble. The mesh sizes are $\Delta x = d/[10, 20, 40, 80, 160]$. The time step is set as $\Delta x/10$ and the Courant number is set to 0.1.

The comparison of the bubble shape at t=0.12 s and the time history of the bubble rising velocity with different mesh sizes are displayed in Figure 4.2. The protrusion appeared with the mesh size of $\Delta x = d/80$ and $\Delta x = d/160$ (Figure 4.2(a)). The results of bubble rising velocity are converged with the mesh size of $\Delta x = d/40$. The comparison of the liquid jet velocity is shown in Table 4.4. The converged results are obtained with the mesh size of $\Delta x = d/40$. To obtain reliable simulation results, the mesh size of $\Delta x = d/80$ is chosen for the following research in this chapter.

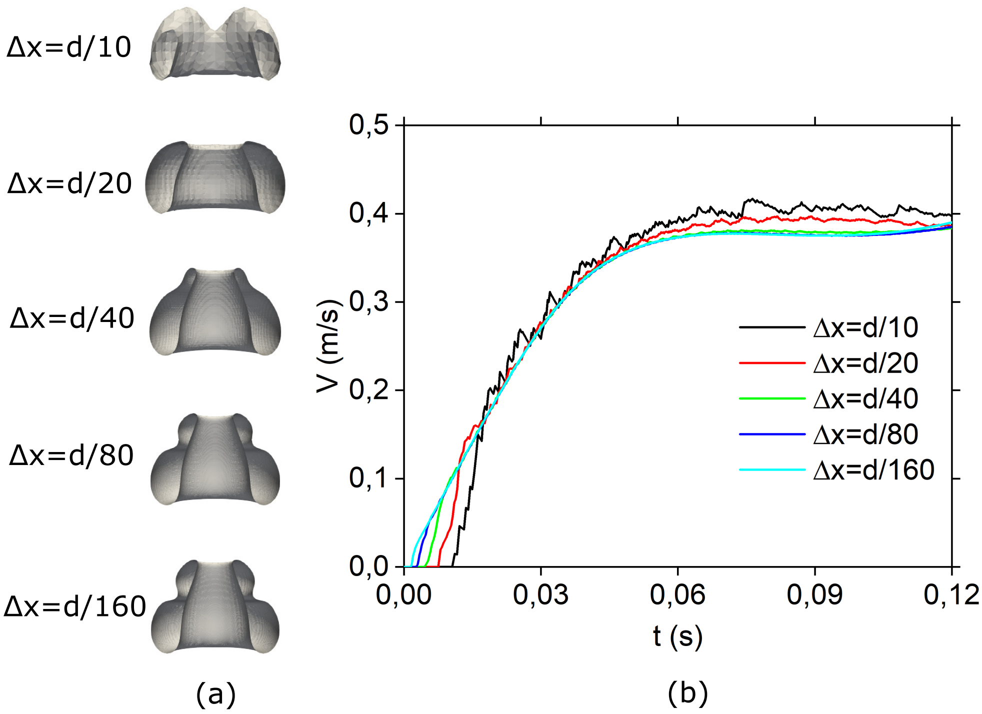

Figure 4.2: The mesh independent study for a central breakup bubble, a) the bubble shape at t=0.12 s, b) the time history of the bubble rising velocity with different mesh sizes.

Table 4.4: The comparison of the jet velocity with different mesh sizes at t=0.044 s.

mesh size	V_{jet} (m/s)
d/10	1.84076
d/20	1.6375
d/40	1.57202
d/80	1.54384
d/160	1.59786

4.2 Results

4.2.1 Central Breakup Mechanism

The results with the mesh size of $\Delta x = d/80$ in Section 4.1.2 are used to analyze the central breakup mechanism. Figure 4.3 illustrates the evolution of the pressure distribution and the shape deformation of a central breakup bubble induced by a strong liquid jet. At the initial time, the bubble shape is spherical (t=0.002 s). As the bubble rises, its lower surface collapses due to the buoyancy force (t=0.03 s) and an upward liquid jet forms (t=0.0044 s), which is caused by the pressure difference between the top and bottom of the bubble. The potential energy $\rho g d$ is converted into the kinetic energy ρV_{jet}^2 [32]. A small local high pressure region in the collapse of the lower surface of the bubble is produced by the collision of the liquid jet with the bottom of bubble (point 1 in Figure 4.5b). But due to the small density of the gas inside the bubble, the local high pressure region is not so obvious. The liquid jet velocity is much larger than that of the rising bubble (Figure 4.6b and c), which leads to the penetration of the liquid jet and the formation of a toroidal bubble (t=0.076 s). Due to the large buoyancy force, the liquid jet has a wide cross section [26]. Right before the bubble breakup, the liquid jet collides with the top of the bubble. At this position (point 2 in Figure 4.5(b)), the gas is squeezed before the bubble breakup, thus a high pressure zone inside the bubble is formed. After that, a small toroidal protrusion appears at the top of the big toroidal bubble (t=0.1 s). Due to the collision of the liquid jet with the bubble, a circulation inside the toroidal bubble is formed and the gas velocity around the liquid jet inside the toroidal bubble is much larger than that of the gas in other places as shown in Figure 4.4. In consideration of the small surface tension force (large Eo number), the gas around the liquid jet with high velocity can overcome the restriction of surface tension and the protrusion is formed at the top of the bubble.

During the breakup process, the bubble vertical height decreases (Figure 4.6a) first due to the buoyancy force and liquid jet. At the instant of bubble

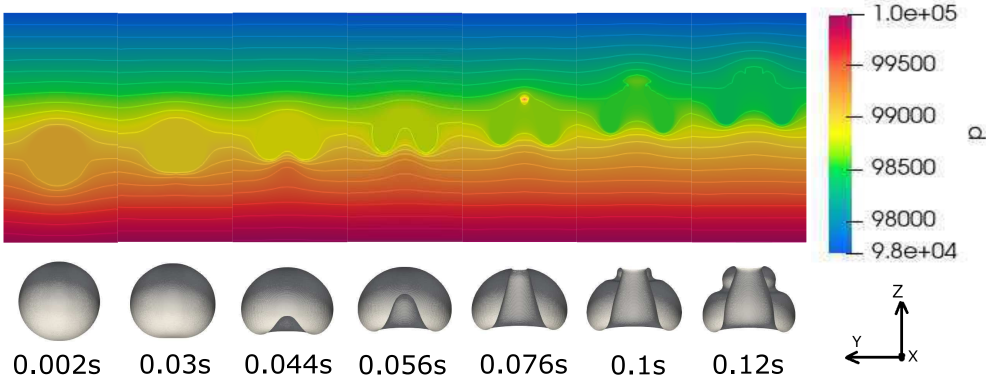

Figure 4.3: The pressure contour and shape evolution of a central breakup bubble from present numerical simulation.

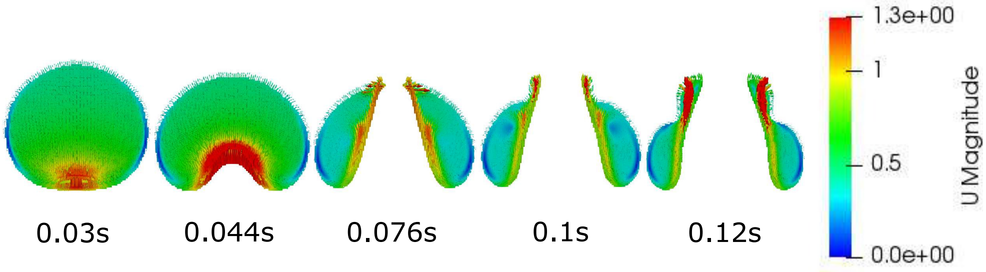

Figure 4.4: The velocity field inside the bubble at different time instants.

breakup, the bubble height reaches the minimum ($\Delta H_{bubble} = 0.01\,\text{m}$). After that, the bubble is "stretched out" in the vertical direction because of the formation of the protrusion. It is interesting to observe the stretched bubble height is almost the same as the initial bubble radius.

Here the bubble rising velocity (Figure 4.6b) and the liquid jet velocity (Figure 4.6c) are also plotted. V_{jet} is defined as the maximum velocity in the center line of the flow domain in each time step. The bubble rising velocity increases due to the buoyancy force and maintains a constant value (0.4 m/s). The liquid jet velocity reaches the maximum (1.7 m/s) at about 0.4 s. During the penetration of the jet into the bubble, the kinetic energy of the liquid jet is used to overcome the surface tension, which tries to keep the bubble spherical. At the time of bubble breakup, the jet velocity decreases from 1.55 m/s to about 1.25 m/s Figure 4.5(a). After that, the jet velocity is still decreasing due to the liquid viscosity (Figure 4.6c).

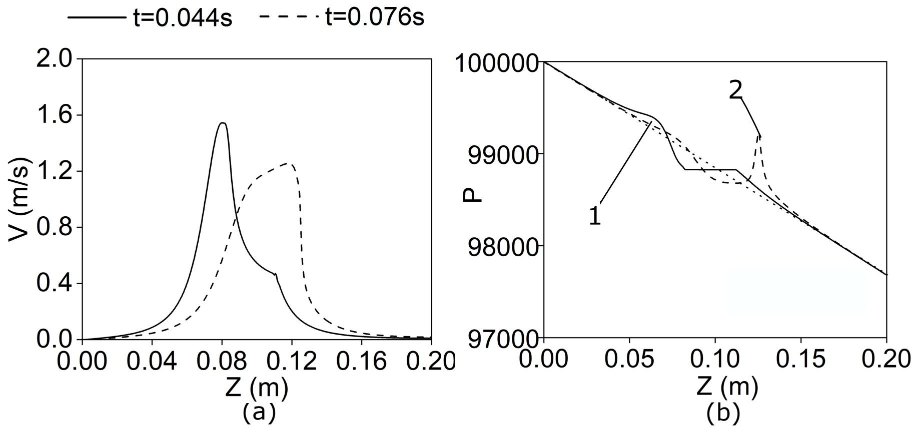

Figure 4.5: The distribution of (a) vertical velocity and (b) pressure along the center line (Z direction) of the domain.

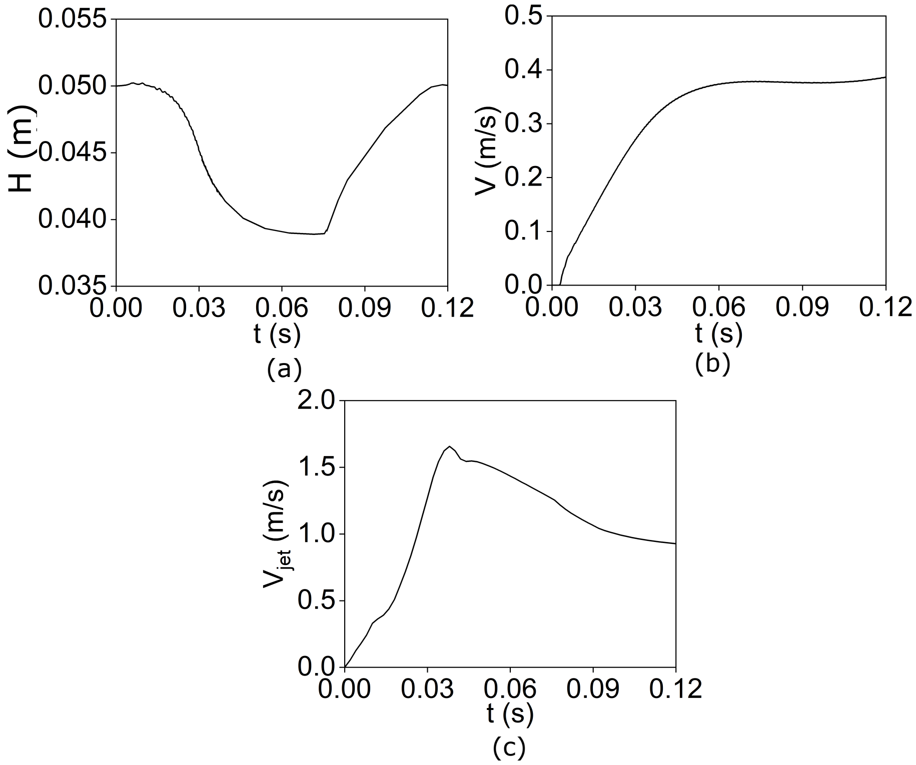

Figure 4.6: Time history of (a) bubble height, (b) bubble rising velocity, (c) liquid jet velocity.

4.2.2 Influence of the Bubble Size on the Bubble Breakup

In this section, the influence of bubble size on the breakup process is studied. On one hand, as the bubble radius increases, the potential energy $\rho g d$ also becomes larger, which leads to the increase of the liquid jet velocity. On the other hand, the larger bubble volume, the bigger the buoyancy force. So the bubble rising velocity is increasing with the enlargement of the bubble. By comparing the results (Figure 4.7) of another two cases with R=0.015 m (case a) and R=0.035 m (case b) with the same liquid properties in Table 4.1, the shape evolution of the two bubbles are almost the same before the central breakup. The central breakup of case (b) happens at t=0.088 s, which is later than that of case (a) (t=0.066 s). After the central breakup of the bubble, the pressure value in the high pressure zone of case (a) is smaller than that of case (b) because the velocity of the liquid jet of case (a) is smaller than that of case (b). At t=0.12 s in Figure 4.7, no protrusion of case (a) is observed while the protrusion of case (b) is longer than that of the bubble with R=0.025 m (Figure 4.3). Based on the analysis of the central breakup mechanism, the velocity of the gas inside the toroidal bubble around the liquid jet in case (a) is not large enough to overcome the surface tension due to the small velocity of the liquid jet, thus no protrusion is formed.

The results of different sized bubble are summarized in Figure 4.8. The physical properties and bubble sizes are displayed in Table 4.5. It takes longer time for the liquid jet to reach the maximum velocity for larger bubbles. Even though the jet velocity is larger for bigger bubbles, the time taken to penetrate the bubble increases as shown in Figure 4.8(a) because of the increase of the bubble rising velocity and of the bubble vertical length. After the central breakup of the bubble, its vertical length also increases due to the large velocity of the gas inside the bubble around the liquid jet.

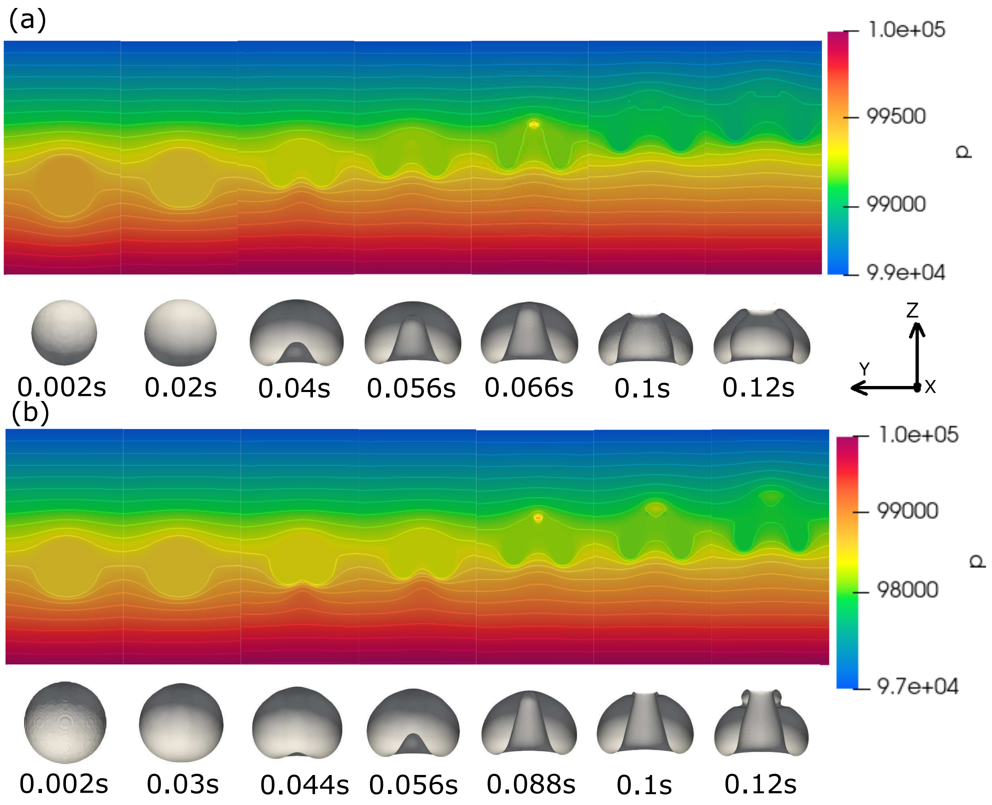

Figure 4.7: The pressure contour and shape evolution of a central breakup bubble with (a) R=0.015 m and (b) R=0.035 m.

Table 4.5: The physical parameters and bubble sizes for different cases.

radius (m)	Eo	Ga
0.015	39.6	117.7
0.02	70.5	181.2
0.0228	91.6	220.5
0.025	110.1	253.2
0.03	158.6	332.8
0.035	215.5	419.4

4.2.3 Influence of Liquid Properties

First the influence of liquid viscosity on the bubble breakup is investigated and the physical properties are shown in Table 4.6. With the increase of the liquid viscosity, part of the potential energy $\rho g d$ is used to overcome the liquid resistance. Therefore, the jet velocity decreases with increase of the

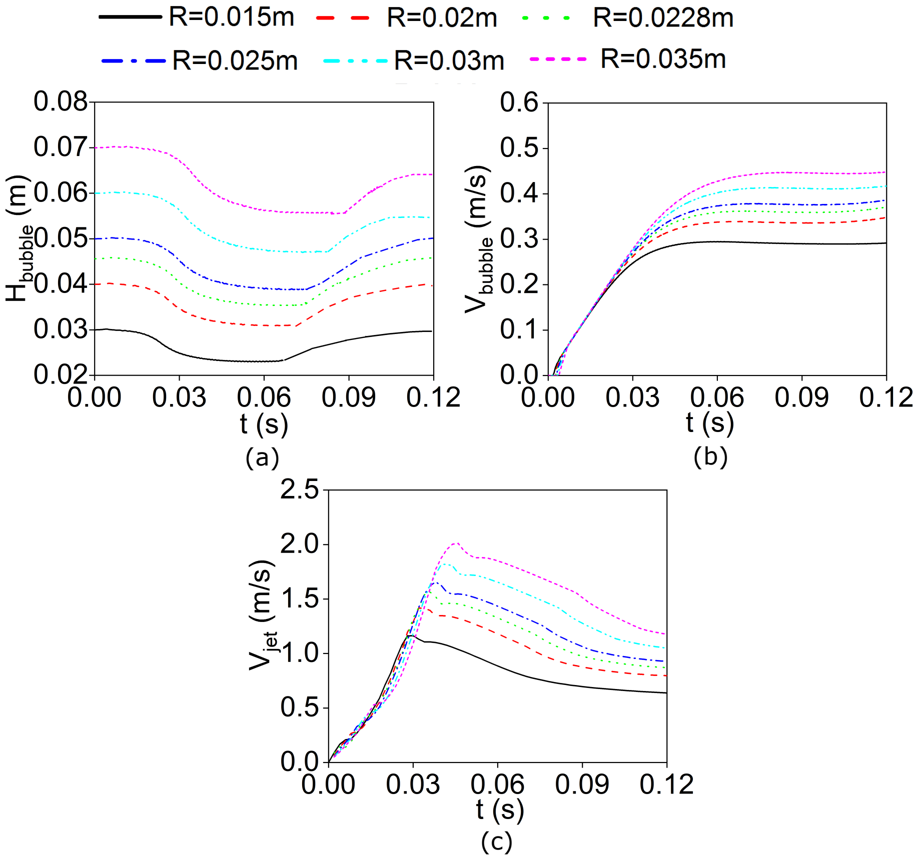

Figure 4.8: The influence of bubble size on the (a) vertical bubble height, (b) bubble rising velocity,(c) liquid jet velocity.

liquid viscosity as shown in Figure 4.9(c). However, the influence of the liquid viscosity on the bubble rising velocity could be ignored as shown in Figure 4.9(b). But at t=0.12 s, the case with smallest liquid viscosity attains the largest rising velocity. In Figure 4.9(a), the bubble in the case of smallest liquid viscosity is penetrated firstly due to the largest jet velocity. After the bubble breakup, the bubble in the case of the smallest viscosity liquid has the longest vertical bubble length. The reason is that part of the kinetic energy of the protrusion is used to overcome the viscosity force. The gas velocity around the liquid jet is higher than that in other places inside the bubble. Therefore, less kinetic energy of the gas around the liquid jet is needed to overcome the smaller viscosity force induced by other gas with lower velocity, thus making the protrusion longer.

Table 4.6: The physical parameters and bubble sizes for different cases.

radius (m)	μ_{liquid} (mPa s)	Eo	Ga
0.025	30	110.1	487.7845
0.025	57.8	110.1	253.2
0.025	90	110.1	162.6
0.025	120	110.1	121.9461

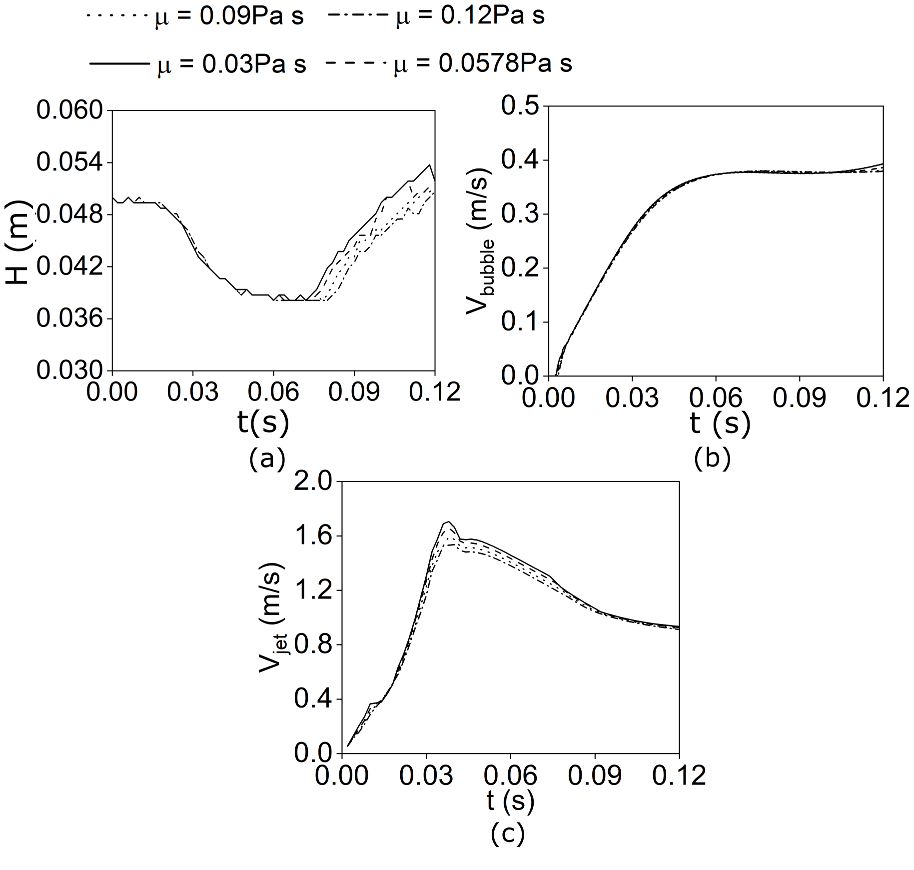

Figure 4.9: The influence of liquid viscosity on the a) vertical bubble height, b) bubble rising velocity, c) liquid jet velocity.

Since the liquid density could affect the potential energy, the influence of liquid density on the breakup is studied as well. The physical properties and bubble sizes are listed in Table 4.7. The maximum liquid jet becomes larger with the increase of the liquid density as shown in Figure 4.10(c). But the

Table 4.7: The physical parameters and bubble sizes for different cases.

radius (m)	ρ_{liquid} (kg/m^3)	Eo	Ga
0.025	500	46.6	107.1
0.025	1182	110.1	253.2
0.025	2000	186.4	428.4
0.025	3000	279.5	642.6

Table 4.8: The physical parameters and bubble sizes for different cases.

case	radius (m)	Surface Tension (kg/s^2)	Eo	Ga
a	0.025	0.03	241.6	253.2
b	0.025	0.0658	110.1	253.2
c	0.025	0.09	80.5	253.2

influence of the liquid density on the bubble rising velocity is negligible as seen in Figure 4.10(b). Before t=0.1 s, the bubble rising velocity in the case of different liquid density is almost the same. After that, the bubble in the larger density liquid rises faster than that in the smaller density one. The larger the liquid jet velocity, the shorter time it needs to breakup the bubble. The vertical bubble length re-increases after breakup and is larger for the case with larger liquid density, due to the large velocity of the liquid jet.

Because the surface tension could keep the bubble spherical and resists the penetration of the liquid jet, the effect of the surface tension on the central breakup is also studied. The physical properties and bubble sizes are listed in Table 4.8. However, due to the large jet velocity, the influence of liquid surface tension on the jet velocity is very small (Figure 4.11 (c)). The same conclusion applies to the influence of surface tension on the bubble rising velocity. The smaller the surface tension, the shorter time is needed to break the bubble up and the bigger the bubble vertical length after the breakup. But still, the liquid surface tension has little effect on the bubble breakup. After the central breakup, some differences are observed as shown in Figure 4.12. Since the surface tension is against the bubble deformation, the larger surface tension (case c) makes the protrusion shorter (blue line in Figure 4.12).

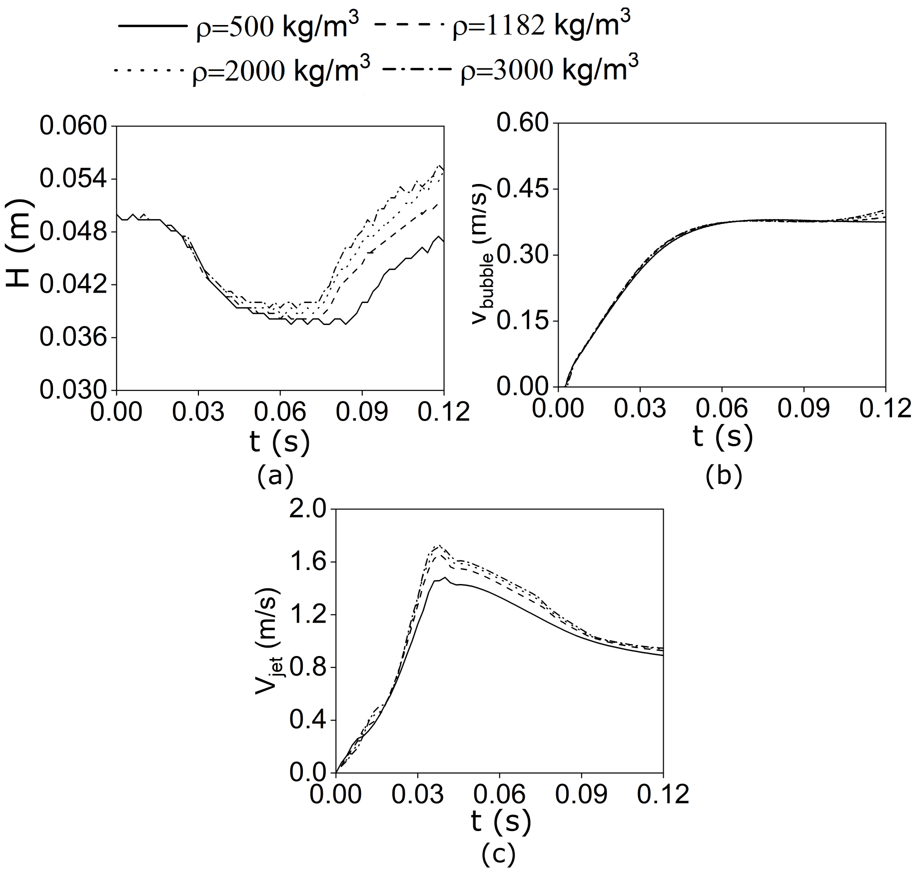

Figure 4.10: The influence of liquid density on the a) vertical bubble height, b) bubble rising velocity, c) liquid jet velocity.

4.2.4 Influence of Density and Viscosity Ratios

In this section, the influence of the density and viscosity ratios on the bubble breakup behaviors is numerically studied. Firstly, the gas density is changed while keeping the liquid properties unchanged as is shown in Table 4.9. From the analysis of the central breakup mechanism, the shape evolution during the central breakup depends largely on the flow field inside the bubble due to the impact of the liquid jet. The variation of the gas density can lead to the change of the flow field inside the bubble, thus changing the central breakup behavior.

The bubble rising velocity and liquid jet velocity under different density ratios are compared while keeping other dimensionless numbers unchanged

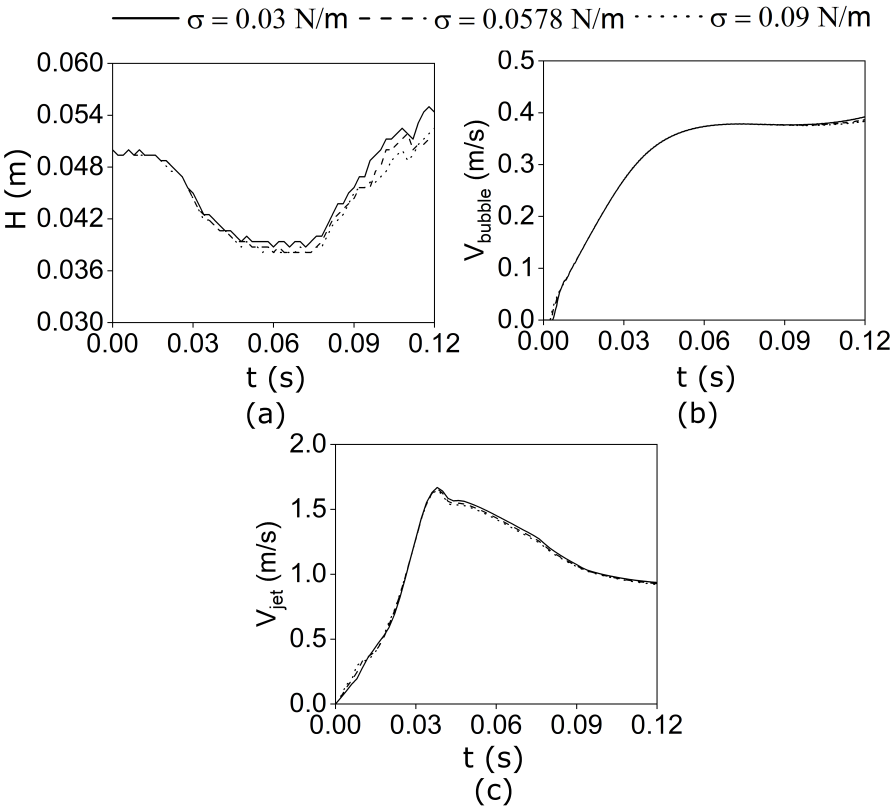

Figure 4.11: The influence of surface tension on the a) vertical bubble height, b) bubble rising velocity, c) liquid jet velocity.

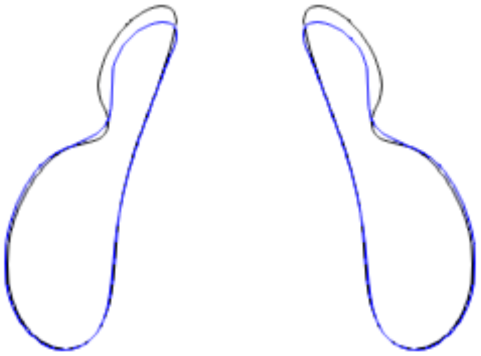

Figure 4.12: The comparison of the bubble shape for case a (black line) and c (blue line).

Table 4.9: Physical properties of the gas bubble.

case	Ga	Eo	μ_r	ρ_r
1	171	131	5.9×10^{-5}	8.27×10^{-4}
2	171	131	5.9×10^{-5}	8.27×10^{-3}
3	171	131	5.9×10^{-5}	8.27×10^{-2}
4	171	131	5.9×10^{-5}	8.27×10^{-1}

as shown in Figure 4.13. The results of cases 1 and 2 are close to each other. For case 3, the bubble rising velocity decreases to 0.38 m/s and the maximum liquid jet velocity to 1.4 m/s due to the increase of the gas density. For case 4, the liquid jet velocity is not large enough to penetrate the bubble and a skirted bubble is observed in this case.

The bubble shape evolution and velocity field inside the bubble for case 3 are shown in Figure 4.14. The breakup time is postponed to t=0.1 s. Small satellite bubbles can be found at the top of the bubble. Another difference is that no protrusion appears. Because the gas inside the bubble of case 3 is "heavier" than that of case 1, The velocity inside the bubble of case 3 is much smaller than that of case 1 after comparing Figure 4.14(b). Therefore, there is no increase of bubble rising velocity after the central breakup for case 3 as shown in Figure 4.13(a).

We also investigate the influence of viscosity ratio on the central breakup behaviors. The dimensionless parameters of the three cases considered are listed in Table 4.10. Only the viscosity ratio is different by changing the gas viscosity. The comparisons of the bubble rising velocity, the liquid jet velocity and the shape evolution under different viscosity ratios are shown in Figure 4.15. The central breakup behavior is observed for all these three

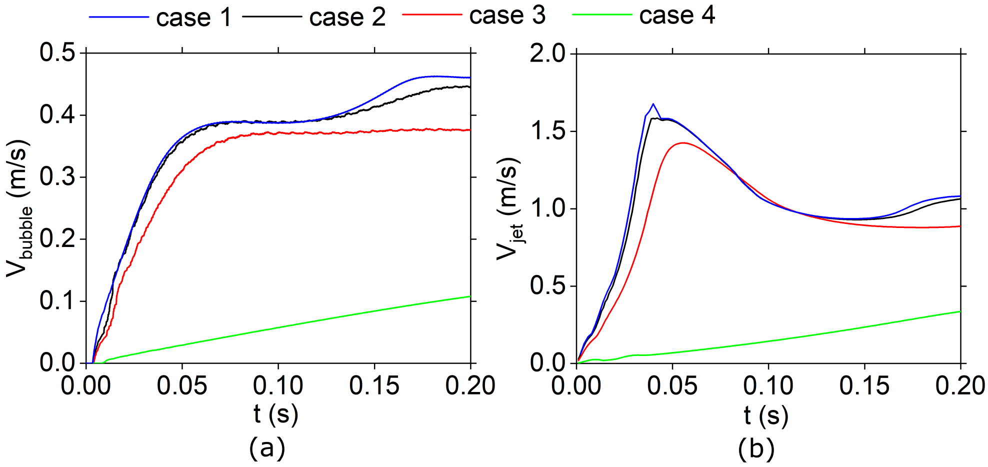

Figure 4.13: The comparison of (a) bubble rising velocity and (b) liquid jet velocity under different gas density.

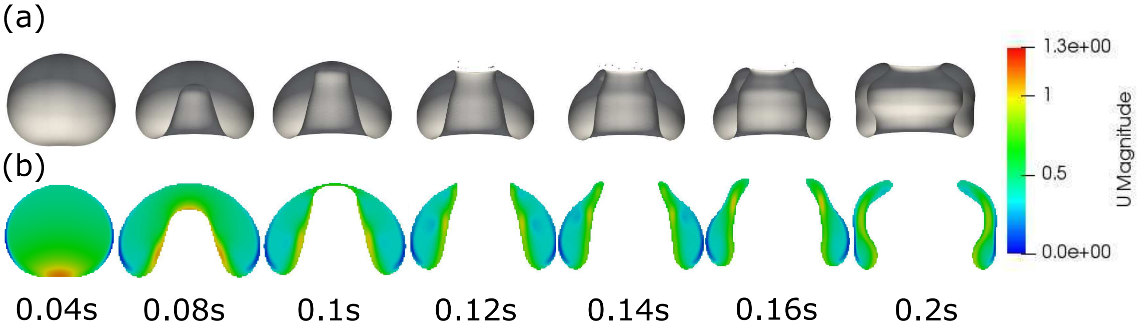

Figure 4.14: The time evolution of a) bubble shape, b) velocity field inside the bubble for case 3.

cases. The time history of the bubble rising velocity and liquid jet velocity is almost the same before t=0.13 s. After that, the bubble rising velocity of case 1 is smaller than that of the other two cases. After the central breakup, the gas inside the bubble around the liquid jet yields a higher velocity compared to the gas in other places inside the toroidal bubble. The higher viscosity of case 1 results in a higher kinematic energy loss compared to the other two cases. Therefore, the bubble rising velocity of case 1 is smaller than in the other two cases and no protrusion is observed for case 1 as shown in Figure 4.15 (c).

Table 4.10: The non-dimensional parameters for the cases

case	Ga	Eo	ρ_r	μ_r
1	171	131	8.27×10^{-4}	1.56×10^{-1}
2	171	131	8.27×10^{-4}	1.56×10^{-4}
3	171	131	8.27×10^{-4}	1.56×10^{-6}

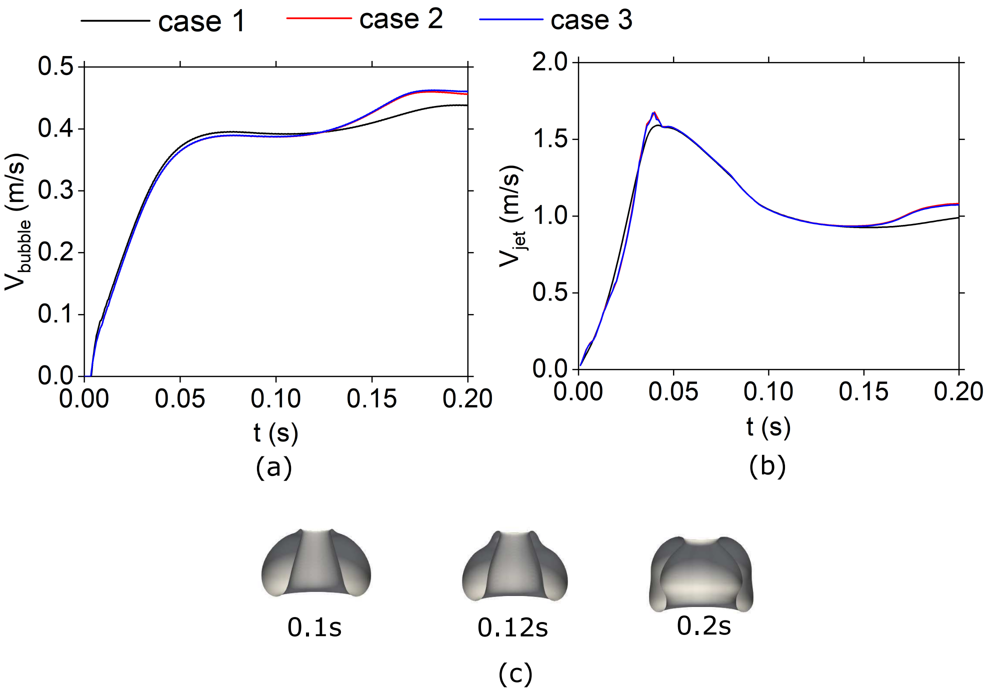

Figure 4.15: The time history of the a) bubble rising velocity, b) liquid jet velocity under different viscosity ratio and c) bubble shape of case 1 .

4.2.5 Influence of the Initial Bubble Shape

In this section, we study the influence of the initial bubble shape on the central breakup behaviors. Here the aspect ratio E is defined as the ratio of the equatorial radius R_x to the polar symmetric semi-axis radius R_z. First we change the length of the equatorial radius while maintaining the polar symmetric semi-axis unchanged. The initial bubble shape with different aspect ratio E is shown in Figure 4.16.

The influence of the aspect ratio on the bubble rising velocity and the liquid jet velocity is shown in Figure 4.17. With the increase of the aspect ratio, the bubble rising velocity becomes smaller due to the decrease of the drag force on the bubble. The bubble with E=0.3 rises much faster than the other bubbles (Figure 4.17 a). The maximum liquid jet velocity becomes larger with the increase of the aspect ratio except for E=0.3 and the reason is clarified later. The bubble shapes at t=0.2 s under different aspect ratios are displayed in Figure 4.18. With the increase of aspect ratio, the torus formed at the bottom of the toroidal bubble becomes smaller but the amount of gas accumulated in the upper part of the toroidal bubble increases. The radius of the liquid jet is decreases with the increase of the aspect ratio. For aspect ratio $E > 1$, the toroidal bubble is broken into two parts (E=1.3 and E=1.5 in Figure 4.18). For an aspect ratio E=0.3, the upper part of the toroidal bubble is broken into satellite bubbles around the lower part of the bubble (the torus formed at the bottom of the original bubble).

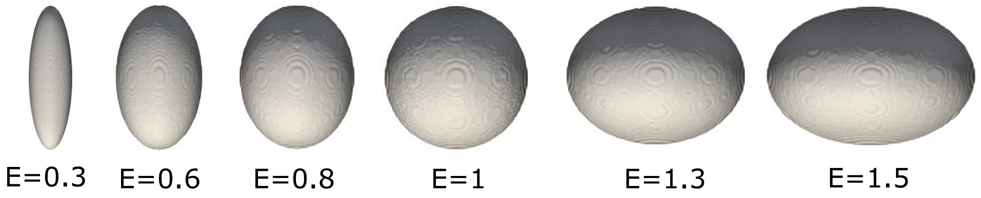

Figure 4.16: The initial bubble shape with different aspect ratio.

Here we analyze the case with E=0.3 and the shape evolution is shown in Figure 4.19. At t=0.2 s, the liquid jet begins to penetrate the bubble from

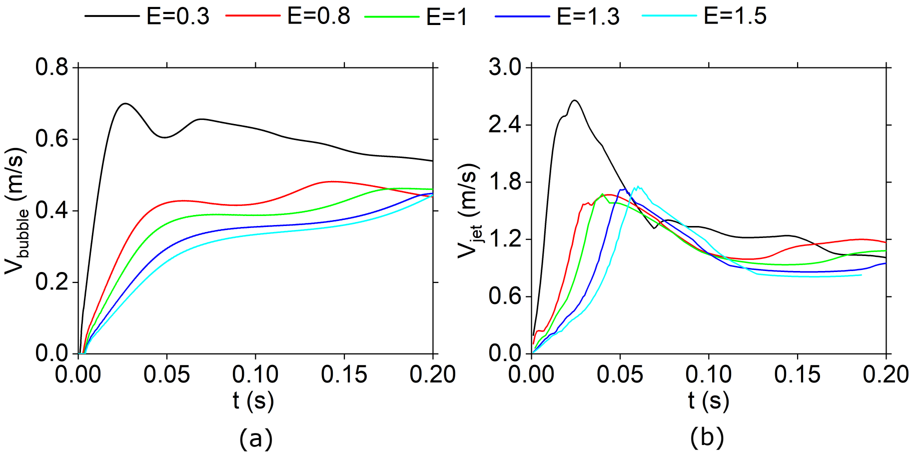

Figure 4.17: The time history of the a) bubble rising velocity, and b) liquid jet velocity under different aspect ratios.

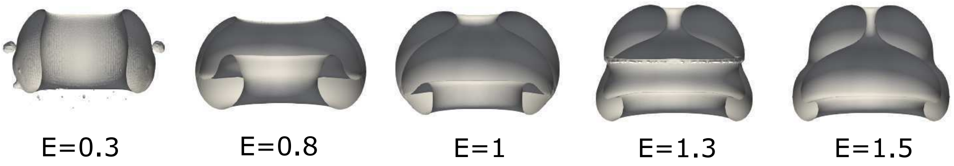

Figure 4.18: The different bubble shapes at t=0.2 s under different aspect ratio.

the bottom. The liquid jet reaches the top surface of the bubble at t=0.04 s. Then due to the circulation inside the bubble and the existence of the liquid jet, the inner radius of the toroidal bubble at the bottom becomes larger (t=0.08 s in Figure 4.19). The broadest hollow part continues to move up until it touches the upper boundary of the toroidal bubble. The toroidal bubble is splitted up at t=0.14 s. With the bubble rising, the splitted upper part is broken into satellite bubbles.

But why the velocity of the liquid jet is much faster than other cases? All the cases have the same vertical length. Therefore the pressure difference ($\Delta\rho g L_v$) between the top and the bottom of the bubble should be the same. Then the potential energy ($\Delta\rho g L_v$) is converted to the kinematic energy (ρV^2) and the jet velocity typically scales as $L_v^{1/2}$. In the experimental paper of Seon and Antkowiak [31], they found a dependence of the liquid jet veloc-

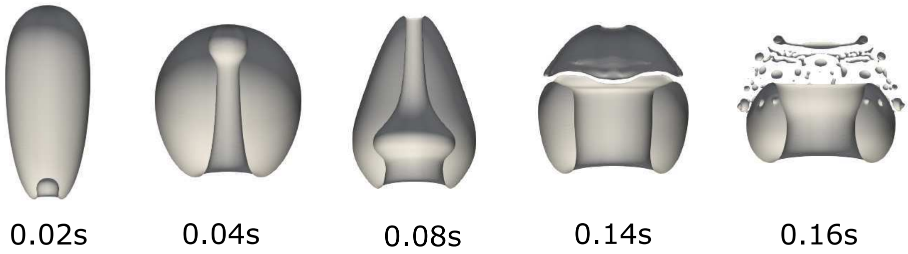

Figure 4.19: The shape evolution of the bubble with E=0.3

ity with $L_v^{3/2}$. Here we give our analysis of a similar numericallly simulated process. In Figure 4.17 (b), one can see thatthe velocity of the jet reaches a maximum at about t=0.02 s. We plot the distribution of the pressure and velocity along the center line in Z-axis direction at t=0.02 s and t=0.04 s (Figure 4.20). One can observe a local high pressure region (point 1) caused by the collision of the liquid jet with the bottom surface of the bubble. The pressure difference between the top and bottom surfaces becomes even larger due to the appearance of a local high pressure region, which in turn increases the jet velocity. Two maximum jet velocities (point a and point b) in Figure 4.20 are observed at t=0.02 s. The first maximum velocity (point a) results from the appearance of the local high pressure region. The second maximum velocity (point b) happens inside the bubble due to the impact of the liquid jet on the bubble. At t=0.04 s before the central breakup, another high pressure region (point 2) appears due to the collision of the jet with the top surface of the bubble. The pressure difference between the top and bottom of the bubble becomes negative and the jet velocity suddenly decreases to 0. But for other cases with $E > 0.8$, no such high pressure region is observed. Thus the collision of the liquid jet with the bottom of the bubble can increases the jet velocity while the collision of the jet with the top of the bubble decreases the jet velocity.

Next we change the length of the polar symmetric semi-axis while the equatorial radius remains unchanged. The initial bubble shape is shown in Figure 4.21, where Z_0 is the vertical radius of the spherical bubble. As analyzed before, the kinematic energy of the liquid jet is related to the potential energy

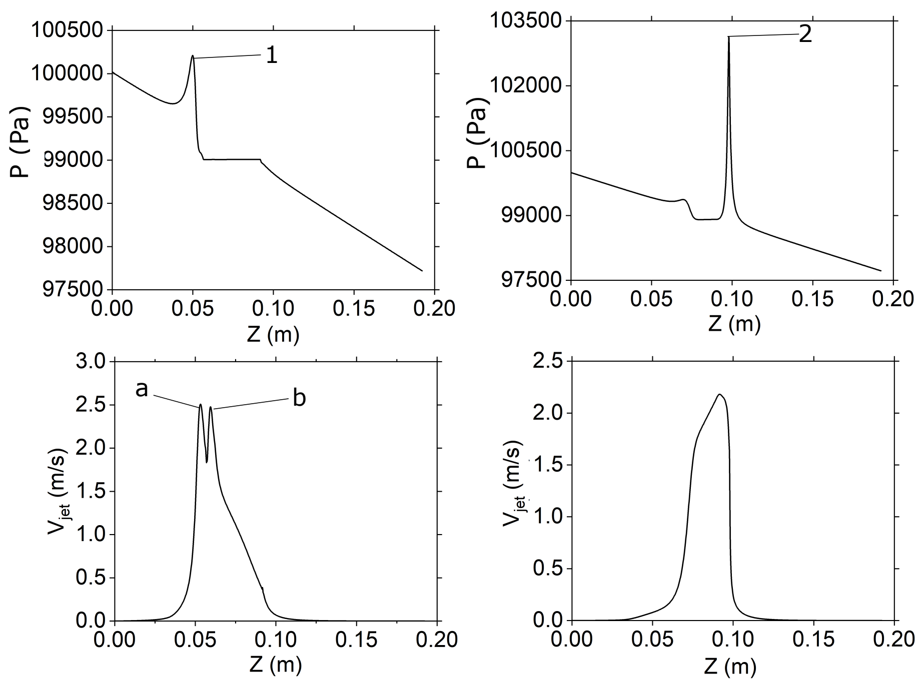

t=0.02s t=0.04s

Figure 4.20: The distribution of pressure and velocity along the center line in Z direction at t=0.02 s and t=0.04 s.

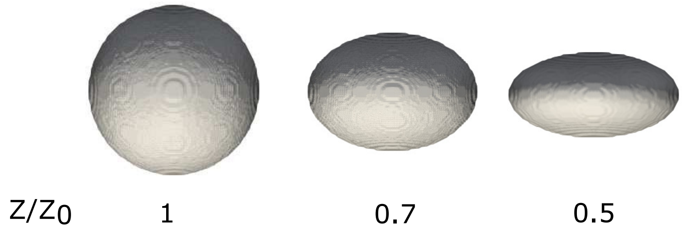

Figure 4.21: The initial bubble shape for $\frac{Z}{Z_0} < 1$

$\rho g L_v$. So the variation of the vertical radius could influence the bubble central breakup behavior. There exists a critical value of the vertical radius, below which the liquid jet can not penetrate the bubble.

Tthree different cases ($Z/Z_0 = 0.5, 0.7, 1$) are simulated. The time history of the bubble rising velocity and of the liquid jet velocity are displayed in Figure 4.22. With the decrease of the initial vertical axis of the bubble, the bubble rising velocity and the liquid jet velocity become both smaller. We

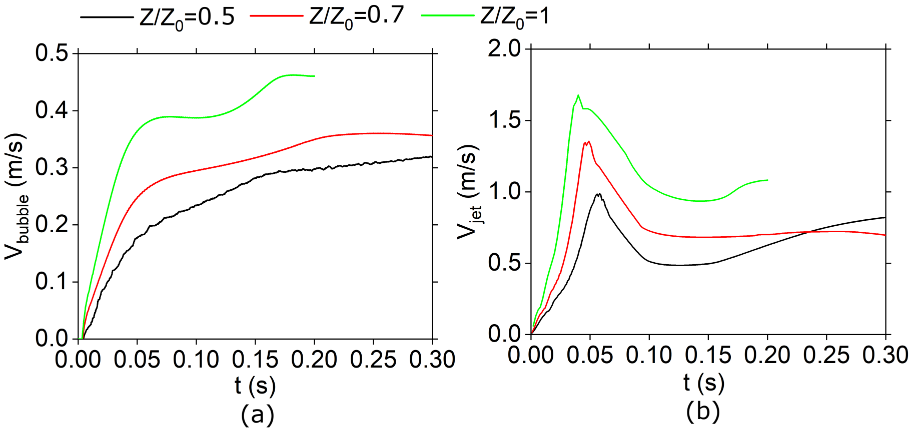

Figure 4.22: The time history of the a) bubble rising velocity, b) liquid jet velocity under different Z/Z_0.

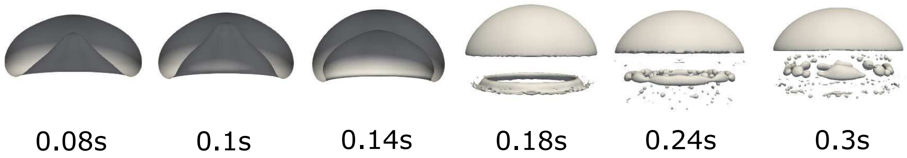

Figure 4.23: The shape evolution of the bubble with $Z/Z_0 = 0.5$.

observe the peripheral breakup instead of the central breakup for the case of $Z/Z_0 = 0.5$ (Figure 4.23). The liquid jet can still lead to the collapse of the bubble(t=0.08 s) but it cannot penetrate the bubble (t=0.1 s). Due to the effect of the liquid jet and the flow field inside the bubble, a ring-like structure is formed at the bottom of the bubble (t=0.14 s). Then the ring-like structure is detached from the main body of the bubble (t=0.18 s). With the bubble rising, the detached ring is broken into satellite bubbles (t=0.3 s).

In experiments, the bubble is usually created with a certain volume of gas. Therefore, it is necessary to study the influence of the aspect ratio on the central breakup with constant bubble volume. Providing the aspect ratio (E=0.3, 0.6, 0.8, 1, 1.3, 1.5) and the bubble volume, one can estimate the equatorial radius R_x and the polar symmetric semi-axis R_z with:

$$R_x^2 \times R_z = R^3 \tag{4.1}$$

Table 4.11: The sizes of the bubble with different aspect ratios and fixed volume

E	R_x (m)	R_z (m)
0.3	0.0179	0.0595
0.6	0.0224	0.0374
0.8	0.0248	0.0310
1.0	0.0267	0.0267
1.3	0.0292	0.0224
1.5	0.0304	0.0203

where R is the spherical bubble radius. The sizes of the bubble with different aspect ratios are displayed in Table 4.11. The bubble rising velocity and the liquid jet velocity of the bubble with different aspect ratios and fixed volumes are shown in Figure 4.24. We can observe the same tendency as that in Figure 4.17. With the increase of the aspect ratio, both V_{bubble} and V_{jet} decrease. V_{bubble} and V_{jet} of the bubble with E=0.3 are much larger than that of other cases. Compared to the bubble with variable volume (Figure 4.16), V_{bubble} of the bubble with the fixed volume is larger when $E < 1$ while it is opposite when $E > 1$ (Figure 4.24a). We can conclude the bubble volume affects V_{bubble}. From Figure 4.24 (b), V_{jet} decreases with the increase of the aspect ratio E due to the decrease of the vertical length of the bubble L_v. For the bubble with E=0.3, the maximum V_{jet} of can even reach 4.5 m/s because the large vertical length of the bubble ($L_v = 0.0595$ m).

4.2.6 Two Inline Bubbles

In this section, the interaction of two inline bubbles is analyzed. Two cases are simulated (Figure 4.25) and the distances between the two bubbles h, are 1.5d and 2d (d is the bubble diameter). The shape evolution of the two cases is shown in Figure 4.26. The trailing bubble experiences a drastic shape change due to the influence of the leading bubble for $h = 1.5d$. However, for $h = 2d$, the influence of the leading bubble on the trailing bubble is insignificant. The same conclusion can be obtained from Figure 4.27.

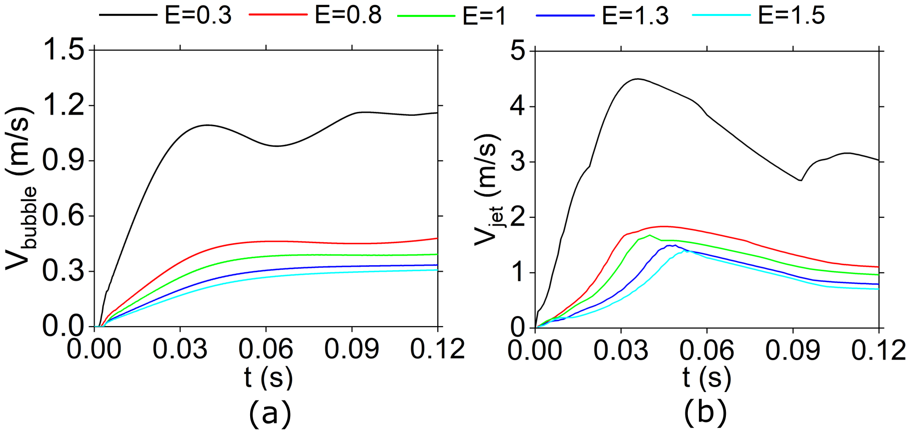

Figure 4.24: The time history of the a) bubble rising velocity, and b) liquid jet velocity under different aspect ratios and same volume.

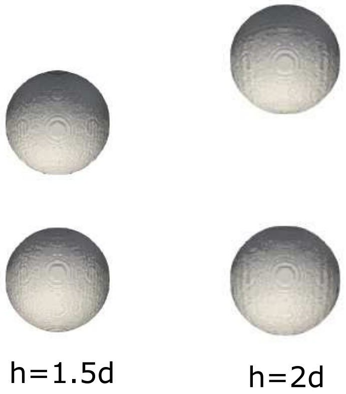

Figure 4.25: The initial configuration of two inline bubbles.

Here the results of two inline bubbles with $h = 1.5d$ are analyzed. As is shown in Figure 4.26 (a), the trailing bubble is slightly elongated at t=0.04 s. More specifically, this is due to the shielding effect of the wake flow behind the leading bubble [111, 114]. This effect tends to entrain the trailing bubble into the dimple formed by the leading one. Due to the elongation of the trailing bubble, the leading bubble is penetrated first at t=0.08 s. From Figure 4.27 (a), the traling bubble rises faster than the leading one after t=0.03 s. Two physical mechanisms are considered for the acceleration of the trailing bubble. First, the decrease of the axial interfacial area reduces the resistance imposed by the upper liquid. Second, the elongation of the trailing bubble

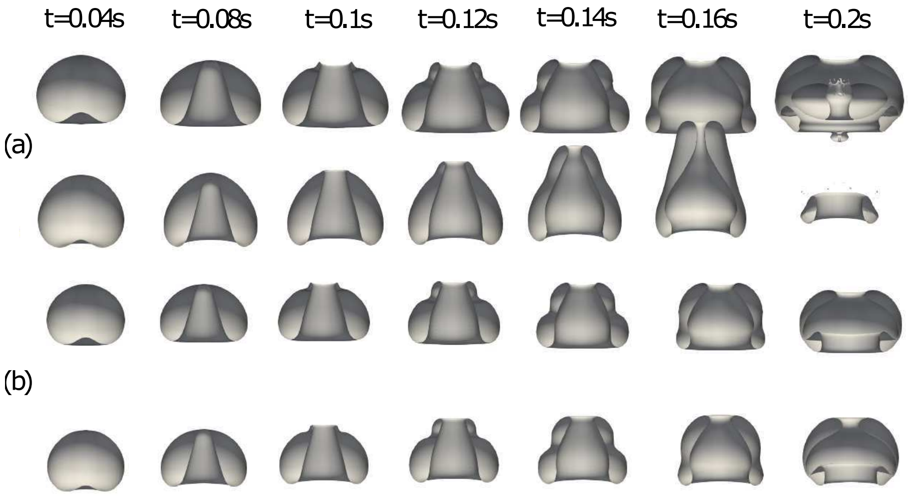

Figure 4.26: The comparison of shape evolution of two inline bubbles, a) h=1.5d, and b) h=2d.

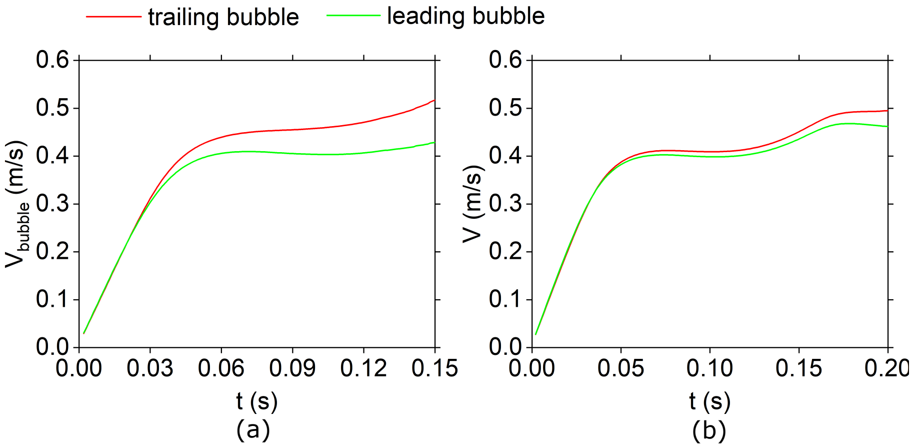

Figure 4.27: The time history of the bubble rising velocity a) h=1.5d, and b) h=2d.

implies a larger pressure difference between the two poles, increasing the liquid jet velocity.

With the approaching of the two bubbles, the elongation becomes more prominent at t=0.12 s. Due to the shielding effect of the leading bubble, the top of the trailing bubble becomes sharp, which helps to increase the gas velocity inside the trailing bubble. More gas moves into the upper part of

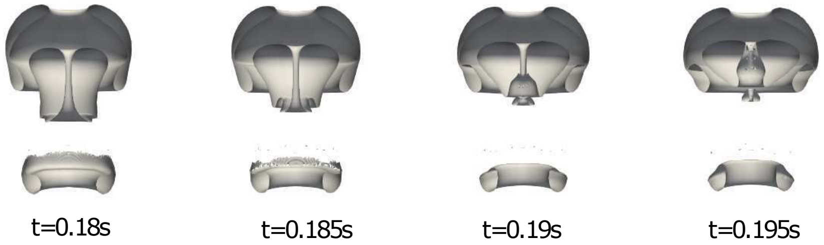

Figure 4.28: The formation of small toroidal bubble.

the trailing bubble (t=0.14 s) and the cross section of the liquid jet becomes smaller (t=0.16 s). The vertical length of the trailing bubble becomes longer with the approaching of the two bubbles and it is broken into two parts. The peripheral breakup is observed at t=0.18 s. In Figure 4.26 (a) at t=0.2 s, we can find a small toroidal bubble between the main bubble and the breakup part. The formation process of the small toroidal bubble is shown in Figure 4.28. The pinch-off singularity leads to the contraction of the lower edge of the upper part of the trailing bubble. Then the small toroidal bubble is "cut down" from the main part of the trailing bubble.

4.2.7 Nondimensionalization of the Influencing Factors

According to the above analysis, the central breakup behavior of a large bubble rising in quiescent liquid is influenced by many factors including the bubble size, liquid properties and so on. This brings difficulty to understanding the essential flow mechanism by analyzing them separately. Therefore, in this section, these factors are nondimensionalized and the central breakup behavior is studied together with the dimensionless numbers introduced in Section 1.2.4.

As indicated by Tripathi et al. [4], the bubble hydrodynamics are determined by three forces, inertia, viscous force and surface tension force, which defines Ga and Eo number. Different combinations of Ga and Eo yield different bubble hydrodynamics. In the central breakup region, the inertia surpasses both the viscous force and the surface tension force. Therefore the liquid jet can penetrate the bubble and the toroidal bubble is formed.

The influence of all the factors can be attributed to the change of Ga and Eo numbers. By summarizing the above results (Figure 4.8, 4.9, 4.10, 4.11), we can see that the bubble size influences the central breakup behavior the most. Since $Ga \propto R^{3/2}$ and $Eo \propto R^2$, the variation of the bubble size changes Ga and Eo to a larger extent compared to other factors. The second most important factor is the liquid density because both Ga and Eo are a linear function of the liquid density. The variation of liquid viscosity can change the Ga number while keeping the Eo number unchanged. The larger Ga number can lead to larger liquid jet velocity. However, no obvious increase of the bubble rising velocity and liquid jet velocity is observed with the increase of the Eo number while keeping the Ga number unchanged. This is because the inertia dominates over the surface tension force in the central breakup region. But as stated before, the surface tension could influence the post-breakup behaviors.

As explained in section 4.2.1, the gas inside the toroidal bubble around the liquid jet still maintains a high velocity after the central breakup, which could overcome the restriction of the surface tension. Thus the protrusion is formed on top of the toroidal bubble. Then more gas moves into the protrusion and the bubble becomes longer. This phenomenon can also be analyzed from a non-dimensional perspective. The large inertia (large Ga) leads to the high velocity of the liquid jet, thus penetrating the bubble. The collision of the liquid jet with the bubble increases the velocity of the gas around the liquid jet. When the surface tension force is small (large Eo), the gas can overcome the restriction, which results in the formation of the protrusion. However, when the surface tension force is large (small Eo), the gas cannot overcome the restriction and no protrusion can then be formed. Here we list the cases (Table 4.12) where no protrusion is observed in our simulations. According to our observation, no protrusion is observed when $Eo < 50$ and $Ga < 200$.

Table 4.12: The cases of no protrusion.

case	Eo	Ga
1	39.6	117.7
2	46.6	107.1
3	39.6	200

4.2.8 Scaling Law for the Liquid Jet and Rising Bubble

Based on the above analysis, the bubble central breakup is quite dependent on the liquid jet velocity and bubble rising velocity, which are influenced by the bubble size, the liquid viscosity, and density, while the influence of the surface tension is very small. In this section, we try to find a scaling law to analyze the influence of these factors on the liquid jet velocity and bubble rising velocity. We define the bubble Reynolds number (Re_{bubble}), and the liquid jet Reynolds number (Re_{jet}) as,

$$Re_{bubble} = \frac{\rho V_{bubble} R}{\mu} \tag{4.2}$$

$$Re_{jet} = \frac{\rho V_{jet} R}{\mu} \tag{4.3}$$

where R is the initial bubble radius, V_{bubble} is the terminal velocity of rising bubble, V_{jet} is the maximum velocity of liquid jet in each case. Figure 4.29 represents the relation between the Re and Ga for all the conducted simulations (21 numerical experiments). The relation between the jet velocity (bubble rising velocity) and the bubble radius for the whole range of physical properties can be summarized as a simple linear law with the constants a and b obtained form a linear fitting to the results of the numerical experiments.

$$Re_{jet} = a_{jet} Ga + b_{jet} \tag{4.4}$$

$$Re_{bubble} = a_{bubble} Ga + b_{bubble} \tag{4.5}$$

where a_{jet},b_{jet},a_{bubble} and b_{bubble} are constant values.

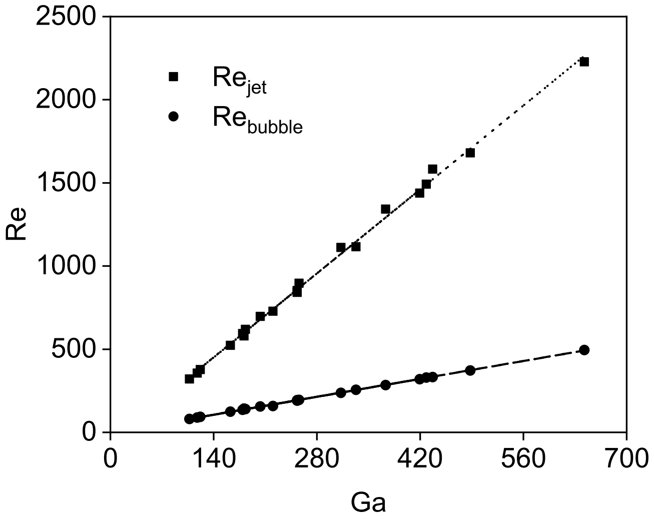

Figure 4.29: Reynolds numbers of the bubble and the liquid jet versus Ga number

4.3 Conclusions

The central breakup process of large bubbles can be influenced by bubble radius and the liquid properties. When the bubble radius becomes larger, the liquid jet velocity increases accordingly and the cross section of the liquid jet becomes smaller. But it takes a longer time to break up the bubble for larger bubbles. If the liquid jet velocity is bigger, the pressure value in the high pressure zone after breakup is also bigger making the sideways jet stronger and the protrusion more obvious. For smaller bubbles (R=0.015 m), no protrusion appears due to the smaller jet velocity. The smaller liquid viscosity as well as the larger liquid density can increase the liquid jet velocity. The influence of liquid surface tension on the bubble breakup is negligible due to the high liquid inertia, but it can affects the formation of the protrusion in the post-breakup stage.

These influencing factors are summarized with four dimensionless factors, Ga, Eo, ρ_r and μ_r. Since $Ga \propto R^{3/2}$ and $Eo \propto R^2$, the variation of the bubble size changes Ga and Eo to a larger extent compared to other factors.

The liquid density plays an important role in the central breakup process because both Ga and Eo are a linear function of the liquid density. The increase of the Ga number (decrease of liquid viscosity) can lead to a larger liquid jet velocity. However, no obvious increase of the bubble rising velocity and liquid jet velocity is observed with the increase of Eo number (decrease of surface tension coefficient) while keeping Ga number unchanged.

The influence of the density and viscosity ratios on the bubble has been studied by changing the gas density and viscosity. With the increase of the density ratio (increase of the gas density), the bubble rising velocity and jet velocity decrease. The variation of the viscosity ratio mainly inluences the circulation inside the bubble. Therefore the appearance of the protrusion is related to ρ_r and μ_r in addition to Ga and Eo.

With the increase of the aspect ratio, the bubble rising velocity becomes smaller. The jet velocity is almost the same except for the case of aspect ratio $E = 0.3$ (highly deformed bubble). This is due to the appearance of the local high pressure zone at the bottom of the bubble, resulting from the collision of the liquid jet with the bubble bottom. If the initial vertical bubble length is decreased, both the bubble rising velocity and the jet velocity become smaller. Thus, for $Z/Z_0 = 0.5$, a peripheral breakup instead of a central breakup is observed. The detached ring-like structure is broken into satellite bubbles. For the bubble with different aspect ratio E and constant volume, both V_{bubble} and V_{jet} decrease with the increase of the aspect ratio. The drag force exerted on the bubble increases with the increases of the aspect ratio (larger horizontal cross section), leading to the decrease of V_{bubble}. While with the increase of the aspect ratio, the bubble vertical length decreases, which resutls in the decrease of the potential energy $\rho g d$. Thus the kinetic energy of the liquid jet decreases.

Finally a case with two trailing bubbles has been also studied. For $h = 2d$, the leading and trailing bubbles do not influence each other. However, for $h = 1.5d$, the leading bubble greatly affects the trailing one. The velocity of the trailing bubble becomes larger than that of the leading one. The trailing bubble elongates due to the shielding effect of the leading bubble. The elongation of the trailing bubble leads to its peripheral breakup. The pinch off singularity yields the contraction of the lower edge of the upper part of the trailing bubble, thus resulting in the formation of a third toroidal bubble.

The formation of the protrusion after the central breakup is also determined by both the Ga and Eo numbers. A large inertia (large Ga) leads to the high velocity of the liquid jet, penetrating the bubble. The collision of the liquid jet with the bubble increases the velocity of the gas around the liquid jet. When the surface tension force is small (large Eo), the gas can overcome the restriction, which results in the formation of the protrusion. However, when the surface tension force is large (small Eo),the gas cannot overcome the restriction and no protrusion can be formed. In the end, a linear relation is found between the jet (bubble) Reynolds number and Ga number.

In this chapter, the fundamental aspects of the bubble central breakup behaviors have been addressed, including bubble size, liquid properties, the density ratio ρ_r, viscosity ratio μ_r, initial bubble shape and the two inline bubbles. We have found that the central breakup behavior mainly depends on the inertia, which surpasses the viscous force and surface tension force. The central breakup is governed by Ga, Eo, ρ_r and μ_r. The initial shape affects the central breakup mainly by changing the vertical bubble length L_v. Based on the results it is proposed that that the bubble radius R in Equations 1.1 and 1.2 be replaced with the vertical bubble length L_v for the central-breakup bubble.

Chapter 5

Non-isothermal Bubble Rising

In this chapter, the rising bubble dynamics with heat transfer is studied through the investigation of the path instability of a bubble rising in quiescent water with variable thermophysical properties. The coupled level set and volume of fluid method introduced in Chapter 2 are adopted to track the interface. Empirical correlations in terms of temperature for thermophysical properties and the equation of state for air are considered in the simulations. The zigzag motion of a compressible air bubble considering the temperature difference with respect to the surrounding water is numerically studied. The mechanism of the zig-zag motion is clarified by analyzing the bubble shape evolution and the wake structure.

The contents in this chapter have been published by the author in International Journal of Multiphase Flow [104].

5.1 Validation

5.1.1 2D Rising Bubble

Hysing et al.[101] proposed two benchmark test cases, namely TC1 and TC2, for the quantitative validation and comparison of two-phase flow codes with interfacial tracking methods. Because only the results of obtained for TC1 with all the benchmarked codes in [101] agree very well with one another, we

Table 5.1: Physical properties of the bubble and surrounding fluid for the test cases

Test case	ρ_1 (kg/m^3)	ρ_2	μ_1 (Pa $\cdot$ s)	μ_2	g (m/s^2)	σ (kg/s^2)
1	1000	100	10	1	0.98	24.5

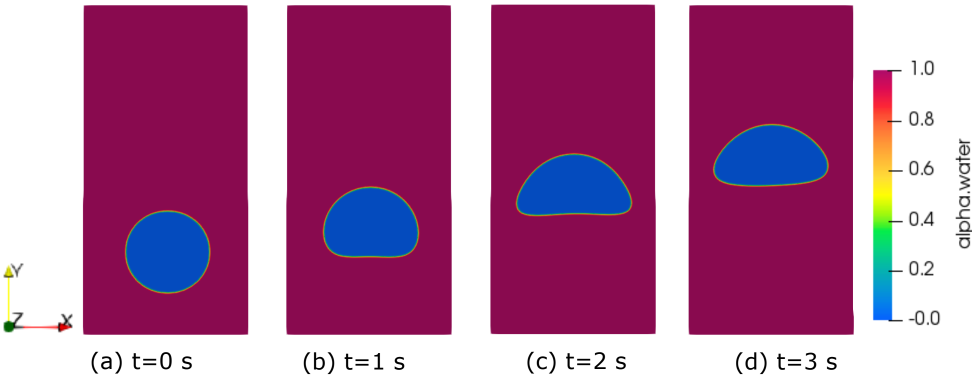

(a) t=0 s (b) t=1 s (c) t=2 s (d) t=3 s

Figure 5.1: The bubble shape evolution of test case at different time instants (h=1/160).

use TC1 as the first assessment case.

The initial configuration consists of a circular bubble of radius $r_0 = 0.25$ m centered at (0.5 m, 0.5 m) in a 1 m × 2 m rectangular domain. The physical properties of the bubble and surrounding fluid are listed in Table. 5.1. The no-slip boundary condition is applied at the top and bottom boundaries while the free slip conditions is used on the vertical walls. A zero gradient is applied for the pressure boundary conditions. The temperature is set to 293 K and all the boundary conditions are set as zero gradient. The computations were performed on a regular hexahedron mesh with a mesh size of $h = 1/[160, 320]$. The first-order Euler scheme was used for time discretization with time step $\Delta t = 1 \times 10^{-4}$ s and a maximum Courant number $Co = 0.05$.

Similar bubble shapes are observed compared to the results in Hysing et al. [101] shown in Figure 5.1. Furthermore, for the quantitative validation of the solver, the same benchmark quantities [101] from Equations 3.1 to 3.3 are adopted, which are: The results obtained by the present simulation

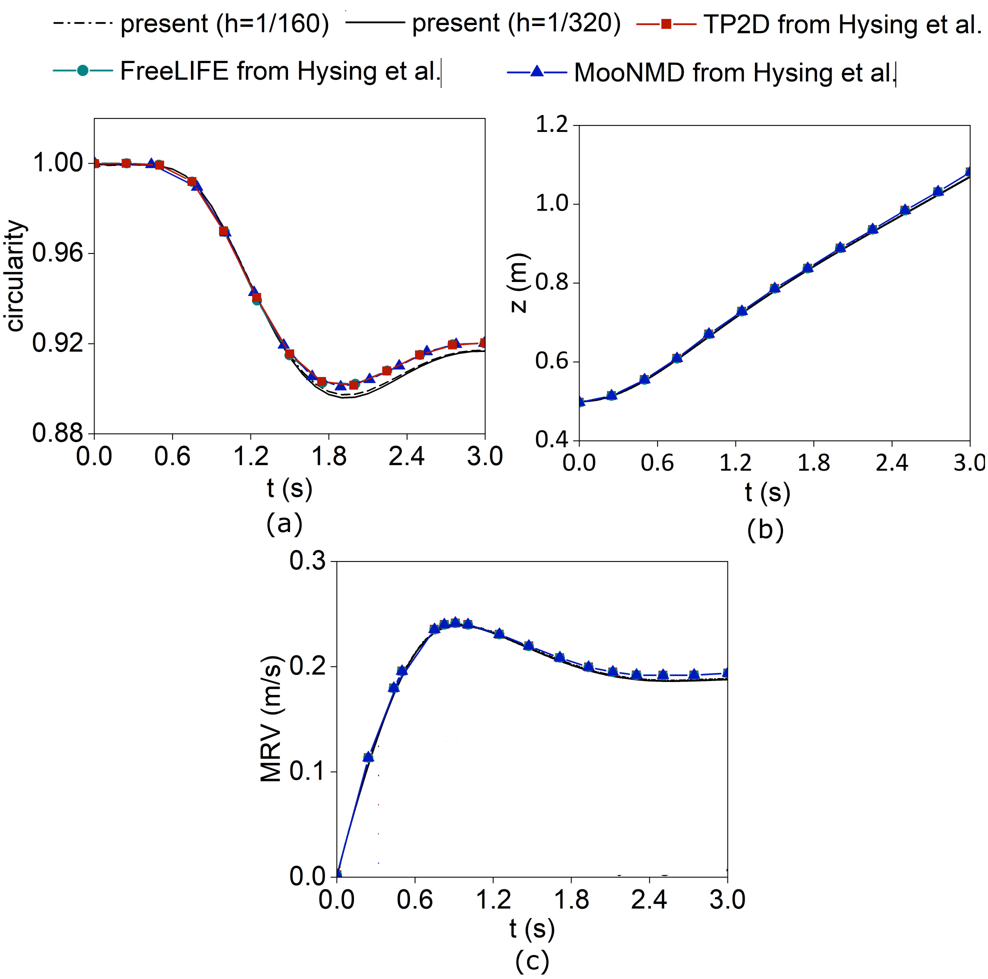

Figure 5.2: Quantitative validation of (a) circularity, (b) center of mass, (c) mean rise velocity.

are also compared to those offered by other three CFD methods reported in [101], namely the Transport Phenomena in 2D (TP2D) [115], the Free-Surface Library of Finite Element (FreeLIFE) [116] and the Mathematics and object-oriented Numerics in MagDeburg (MooNMD) [117]. All the benchmark quantities yielded by the present solver are smaller than those of the other methods as seen in Figure 5.2. In the work of Klostermann et al. [102] and Yamamoto et al. [103], they also reported smaller values. But the relative errors here are marginal (0.36%, 0.97% and 2.70% for the center of mass, the mean rise velocity, and the circularity respectively). Based on the aforementioned results, the accuracy of the present solver for 2D bubble rising is confirmed.

5.1.2 3D Static Bubble

In the work of Francois et al. [118], the authors simulated a static bubble and concluded that a consistent coupling between surface tension and pressure is necessary for obtaining a discrete force balance. The CLSVOF method could reduce the spurious currents due to the accurate calculation of the interface curvature [67, 75, 119]. Albadawi et al. [75] compared the results of 2D static bubble obtained from CLSVOF to that of the VoF method. In the present work, a 3D static air bubble at equilibrium in a zero gravity field is revisited to validate our solver. But the difference is that we consider the temperature difference between the air bubble and the water.

The initial bubble diameter is $D_{ini} = 0.01$ m positioned at the center of the cubic domain. The size of the cubic domain is $2D \times 2D \times 2D$ m^3 filled with water. Three cases are simulated: 1) the temperature of the water and the air bubble are the same (isothermal); 2) the temperature of the air bubble is 293 K while the water is at 363 K, which means the bubble will expand (cold bubble); 3) the temperature of the air bubble is 363 K while the water is at 293 K, which means the bubble will contract (hot bubble). The viscosity of the air is set as constant, 1.84×10^{-5} $\mathrm{Pa \cdot s}$. We can get other properties, such as air density, water properties from Equations 5.1 to 5.5.

$$p = \rho_{air} R_{air} T \tag{5.1}$$

$$\rho_{water} = \frac{98.343885}{0.30542^{1+(1-\frac{T}{647.13})^{0.081}}} \tag{5.2}$$

$$\mu_{water} = \exp(-51.964 + \frac{3670.6}{T} + 5.7331 \times \ln T - 5.3495 \times 10^{-29} \times T^{10}) \tag{5.3}$$

$$\kappa_{water} = 1.815 \times 10^{-9} \times T^3 - 8.0065 \times 10^{-6} \times T^2 + 0.0056903 \times T - 0.4267 \tag{5.4}$$

$$\sigma_{water} = 0.18548 \times (1 - \frac{T}{647.13})^{(2.047 \times \frac{T}{647.13} - 3.554) \times \frac{T}{647.13} + 2.717} \tag{5.5}$$

all in S.I. units.

The boundary conditions are listed in Table 5.2. The pressure value of the top wall is set to the atmospheric pressure (101325 Pa). We allow the fluid in and out at the top wall, so that the bubble is allowed to expand and contract. The mesh resolution is 20 and 40 cells per bubble diameter and the time step is set to $\Delta t = 1 \times 10^{-5}$ s, which satisfies the stability condition [67] given by

$$\Delta t < \sqrt{\frac{\rho \Delta x^3}{\sigma}} \tag{5.6}$$

Table 5.2: The setting of boundary conditions for the static bubble.

boundary	volume fraction	pressure	velocity	temperature
bottom wall	zeroGradient	fixedFluxPressure	fixedValue (0 0 0)	zeroGradient
top wall	inletOutlet	totalPressure	pressureInletOutletVelocity	zeroGradient
side walls	zeroGradient	zeroGradient	slip	zeroGradient

To validate the solver with variable thermo-physical properties, we compare the simulation results of the pressure difference between the inside and outside of the bubble to the theoretical values. The pressure difference can be calculated theoretically from the Young-Laplace equation [120]:

$$\Delta P_{theo} = \frac{2\sigma}{R} \tag{5.7}$$

where R is the radius of the bubble. In consideration of the compressibility effect, the bubble radius is not constant. Therefore, the perfect gas equation of state (5.8) should be considered as well.

$$pV = nR_{air}T \tag{5.8}$$

where V is the bubble volume, n is the number of moles. Following Albadawi's work [75], two numerical approximation of the pressure difference were calculated by the following equations:

$$\Delta P_0 = P_0 - P_\infty \tag{5.9}$$

$$\Delta P_{total} = P_{in} - P_{out} \tag{5.10}$$

where

- P_0 and P_∞ are the value of pressure at the bubble center and at the wall boundary, respectively.
- P_{in} and P_{out} are the averaged value of the pressure inside and outside of the bubble, respectively.

The theoretical and numerical pressure difference as well as the corresponding relative error at t=0.2 s are shown in Table 5.3. The errors E_0 for all the cases with different mesh sizes are the same ($< 2.5\%$). The relative errors of E_{total} are $< 5.3\%$ for $\Delta x = d/20$ and $< 3.14\%$ for $\Delta x = d/40$. We can find that the relative error E_{total} becomes smaller with the mesh refinement. But the accuracy of the results with mesh size $d/20$ is also acceptable.

In order to analyse how the bubble behaves under different combinations of air and water temperature, the bubble volume, the position of its centre of mass, and the sphericity of the bubbles for a mesh resolution $d/40$ have been plotted over time in Figure 5.3.

The bubble volume is non-dimensionalized with the initial bubble volume. The vertical position of its centre of mass is non-dimensionalized with its initial vertical position. An obvious volume change is observed for the non-isothermal bubbles. The relative errors of volume change are 0.037% and

Table 5.3: Errors of the pressure difference for bubble diameter 0.01m at t=0.2s.

Mesh size	Cases	R_{theo} (m)	ΔP_{theo} (Pa)	$\Delta P_0 (Pa)$	E_0(%)	ΔP_{total} (Pa)	E_{total}(%)
d/20	a	0.005	29.09	29	0.31	27.55	5.29
	b	0.0053697	22.6645	22	2.93	23.12	2
	c	0.004655	31.2627	31	0.84	29.95	4.29
d/40	a	0.005	29.09	29	0.31	28.931	0.55
	b	0.0053697	22.6645	22	2.93	21.952	3.14
	c	0.004655	31.2627	31	0.84	30.91	1.13

0.32% for cold and hot bubbles, respectively. All the non-isothermal bubbles moved down away from the initial position and then converged to a point located lower than the initial position. This is due to the bubble volume change and the setting of the boundary conditions (top wall). The displacements in the other two directions for both types of bubbles are below the machine precision: 1.33% and 3.33% for cold and hot bubbles respectively. As observed in Figure 5.3, the sphericity of the bubbles, after an initial drop in the first instants, recovers a little and reaches a steady value very close to 1 (less than 0.15% away from a perfect sphericity). Therefore, the present solver provides accurate predictions for non-isothermal two phase flow systems.

The implementation of the CSF model in the momentum equation generates spurious currents in the vicinity of the interface [121]. Here I analyze the influence of heat transfer on the spurious currents around the bubble shown in Figure 5.4. The maximum velocity magnitudes appeared around the interface between air and water (colours closer to red) with an order of 10^{-1}. The volume change in Figure 5.4 (b) and (c) can be observed. The cold and hot bubbles in Figure 5.4 (b) and (c) move down due to the volume change of the bubble and the boundary conditions. The inflow and outflow are only allowed on the top wall, which can be observed in Figure 5.4 (b) and (c). The expansion of the cold bubble leads to the outflow on the top wall and the contraction of the hot bubble results in the inflow on the top wall. With the development of the velocity field inside the domain, the bubbles move down.

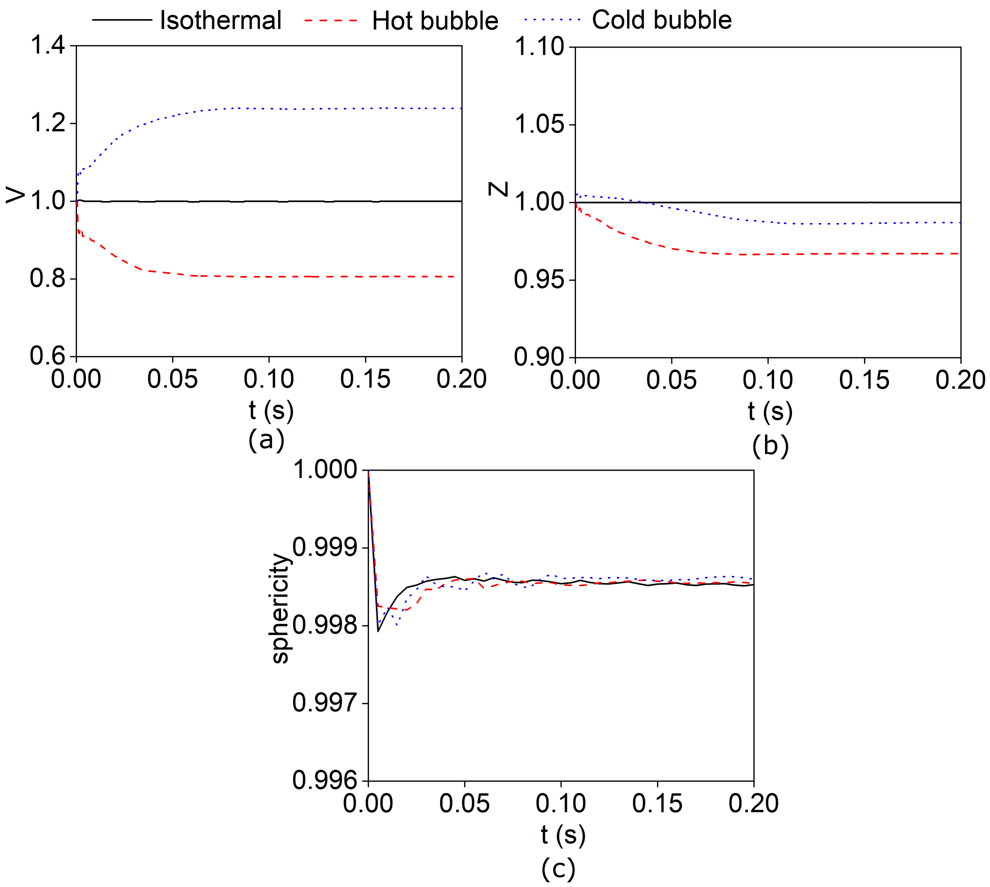

Figure 5.3: Evolution of (a) bubble volume, (b) vertical position, and (c) sphericity for 10 mm bubble.

5.2 Problem Description

5.2.1 Numerical Setting

The 3D domain has a horizontal cross section of $6d \times 6d$ and is 60d high in order to allow the bubble to reach a steady state. The initial bubble diameter simulated in this section is 10 mm. Four cases are investigated: 1) isothermal water and air (293 K); 2) hot air (363 K) in cold water (293 K); 3) isothermal water and air (363 K); 4) cold air (293 K) in hot water (363 K). All other flow conditions are the same for these four cases. We initiate all the simulations with a spherical bubble shape with a diameter of 10 mm. The bubble center

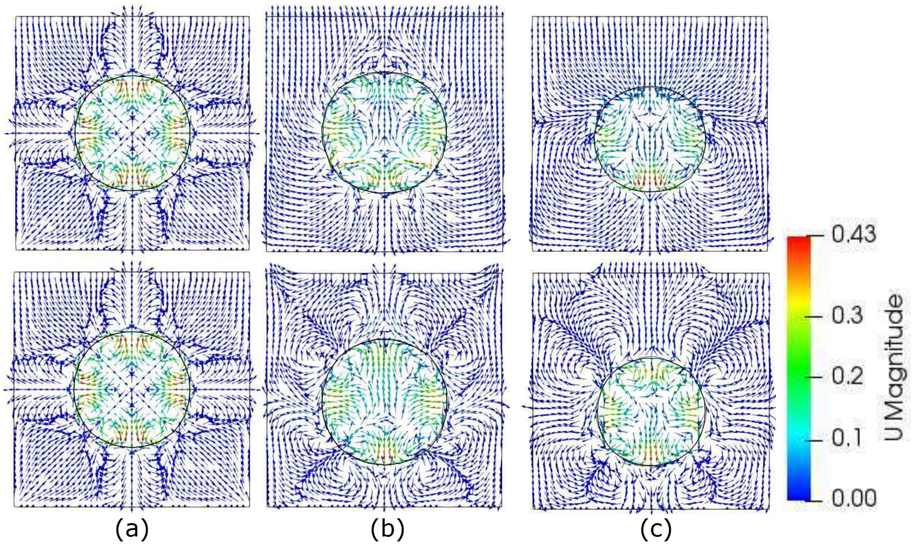

Figure 5.4: Velocity vectors around and inside 10mm bubble at t = 0.01 s (top row) and t = 0.2 s (bottom row), a) case a, b) case b, c) case c.

initially stands 3R above the bottom wall. The boundary conditions are the same as those listed in Table 5.2. The viscosity of air is set to 1.84×10^{-5} $\mathrm{Pa \cdot s}$. We can calculate other properties, such as air density from Equations 5.1 and other water properties from 5.2 to 5.5.

5.2.2 Mesh Independence Study

Before studying the oscillatory bubble dynamics, a mesh independence study is conducted. A cuboid flow domain with $6d \times 6d \times 10d$ is adopted for this purpose. The bubble size and the boundary conditions are the same as those in Section 5.1.2. The computations are performed on a structured hexahedral mesh with a size of $\Delta x = d/[10, 20, 30, 40]$. The time step is set as $\Delta x/10$ and the Courant number is set to 0.5. In the following sections, all variables are made dimensionless using the initial bubble diameter d and the gravitational time $\sqrt{d/g}$ as characteristic length and time scales respectively. The velocity scale is $\sqrt{gd}$.

We simulate the isothermal case (case a) in section 5.1.2 for the mesh independence study. The time history of the bubble rising velocity with different

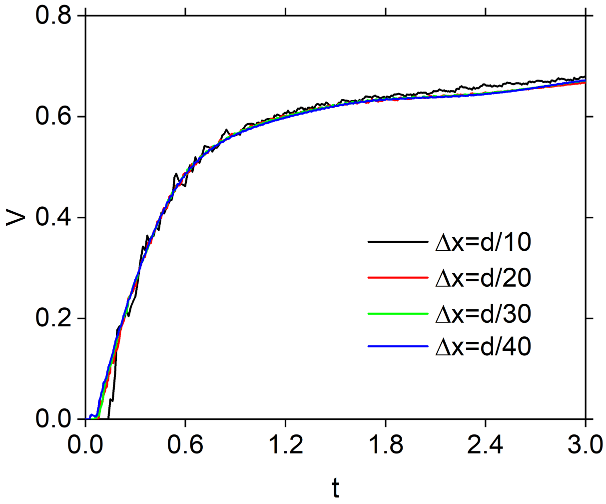

Figure 5.5: The time history of the bubble rising velocity with different mesh resolution.

mesh resolution is shown in Figure 5.5. We can see that the results of mesh size $d/20$ are well converged. Therefore, the mesh size $\Delta x = d/20$ is chosen for the following simulation to save computational time. Actually, in the work of Zun et al. [122] and Rek [123], they suggested that there should be at least 15 cells per bubble diameter, which proves the present mesh resolution as reasonable and computationally economic.

5.3 Results

For the four cases investigated here: 1) isothermal water and air (293 K); 2) hot air (363 K) in cold water (293 K); 3) isothermal water and air (363 K); 4) cold air (293 K) in hot water (363 K), different trajectory paths are observed due to the variation of the water properties and to the compressible effect of air (Figure 5.6). Three stages are observed in case 1 and 2, straight path, aperiodic zig-zag and periodic zig-zag motion (planar zig-zag in [52]). But in cases 3 and 4, the trajectory can be divided into four stages, namely straight path, spiral (chaotic spiral for case 4), aperiodic zig-zag and periodic zig-zag motion (flattened spiraling in [52]). The mechanism for the different

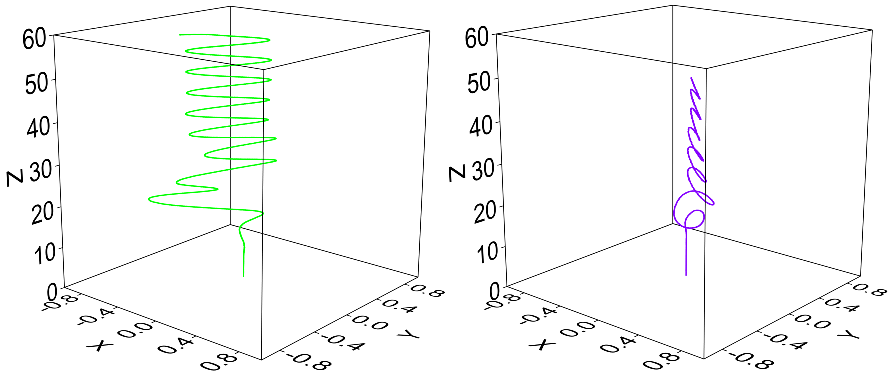

(a) case 1 (b) case 2

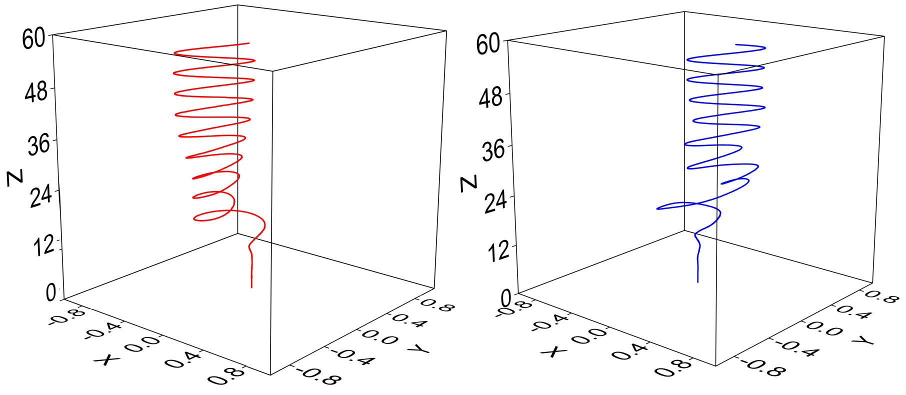

(c) case 3 (d) case 4

Figure 5.6: Different paths of the bubbles

paths will be analyzed in the following sections.

5.3.1 Shape Evolution

The simulation makes use of the aspect ration E recommended by Charin et al. [14] to evaluate the effect of the bubble shape evolution on the path instability, which is defined by:

$$E = \frac{L_z}{\sqrt{L_x L_y}} \tag{5.11}$$

The bubble rises due to the buoyancy force initially following a straight vertical trajectory. The distances of the straight path are about 8.4d, 8.8d, 8.0d and 7.9d for cases 1 to 4 respectively (5.7). During this period, the aspect ratios of all cases are oscillating, which is caused by the wobbling behavior of the bubbles. But the bubble shape is axi-symmetric as displayed Figure 5.8 at t=9.4. The aspect ratio of case 2(4) is a bit bigger(smaller) than that of case 1(3) due to the decrease(increase) of the bubble volume resulting from the compressibility effect of the air. In the aperiodic zig-zag motion, the bubbles lose their symmetry (Figure 5.8 at t=21.9). There are certain inclination of the bubble with respect to its path. During the aperiodic motion, the bubble's aspect ratios in all cases increase to around 0.6 and oscillate for 3 to 4 cycles (Figure 5.7). In the periodic zig-zag motion, the frequency of oscillation of the periodic motion is about 5Hz. The St number is about 0.2 using Equation 1.5 after taking into account the terminal bubble velocity. However, the frequency of the aspect ratio oscillation is about 10 Hz, twice that of the zig-zag motion. We can find that when the bubble passes the furthermost positions, the aspect ratio decreases to the minimum value. In contrast, when the bubble passes the average position, the aspect ratio reaches the maximum value. The reason can be clarified as follows. At the start of the zig-zag loop, there is no inclination of the bubble with respect to its path. Within the zig-zag loop, the bubble begins to tilt toward the direction of the path, achieving the maximum inclination in the middle of the half cycle of the zig-zag [52]. After that, the inclination of the bubble reduces until it vanishes again at the end of the present cycle of zig-zag. So there are two periods within one zig-zag cycle. When the bubble is in the extreme of a zig-zag motion, the bubble has no inclination, corresponding to the maximal lateral excursion and the minimum E value. In the middle of the half cycle of the zig-zag period, the bubble reaches the maximum inclination and reaches the maximum E vlaue.

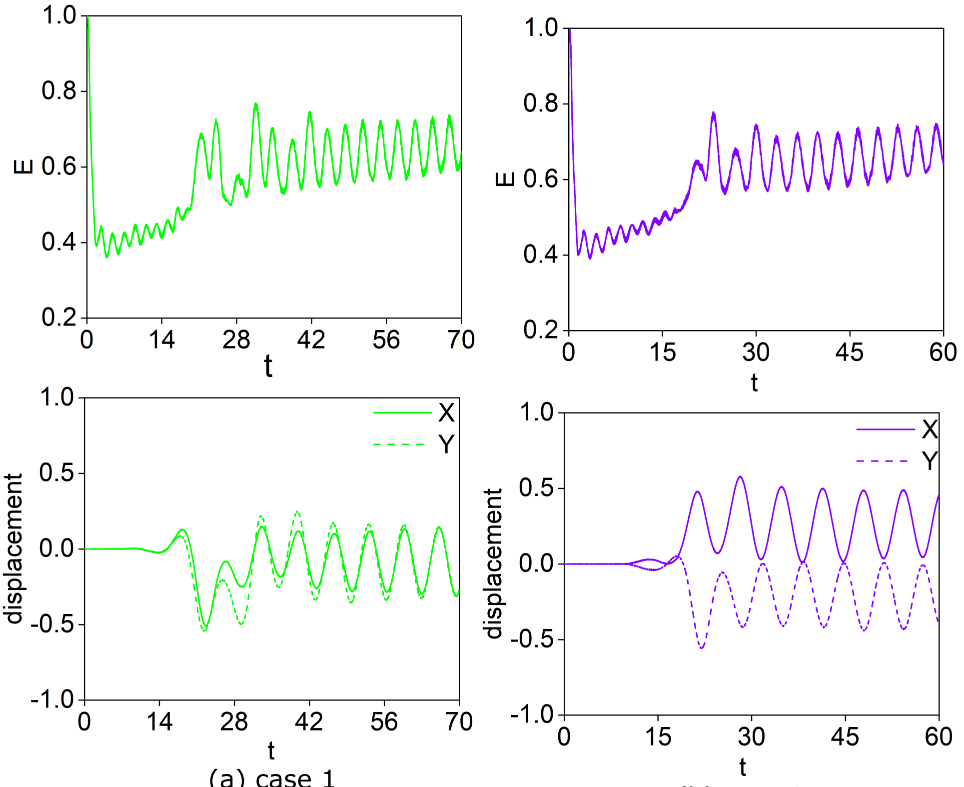

(a) case 1

(b) case 2

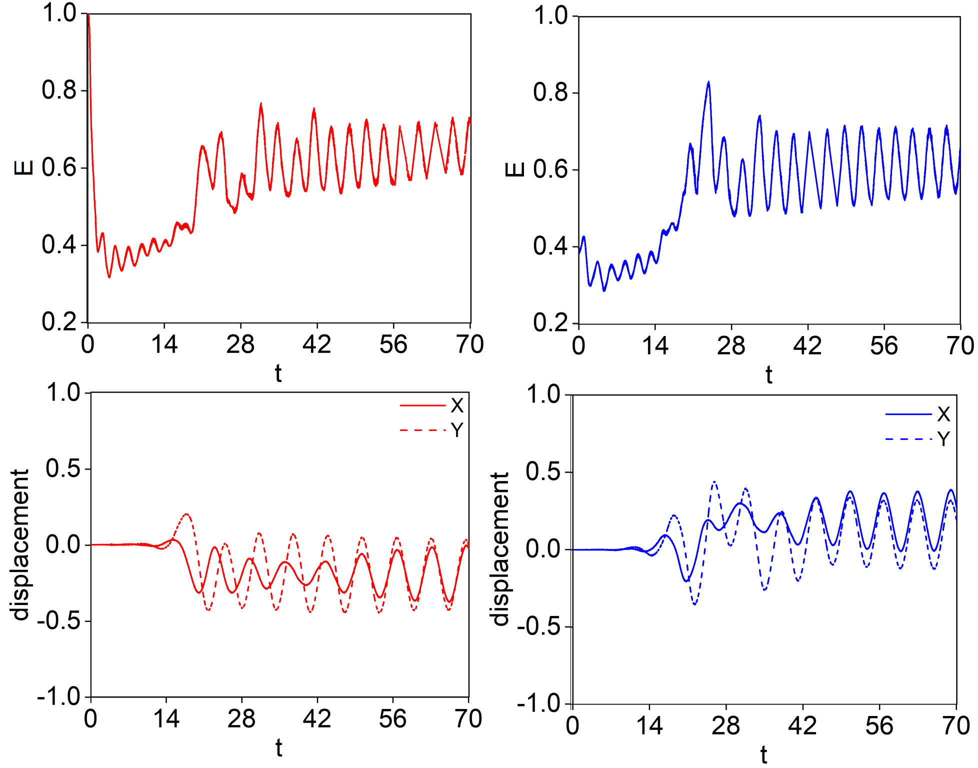

(c) case 3

(d) case 4

Figure 5.7: Transient results of aspect ration E, and displacement of the bubble in the X and Y directions for the four cases

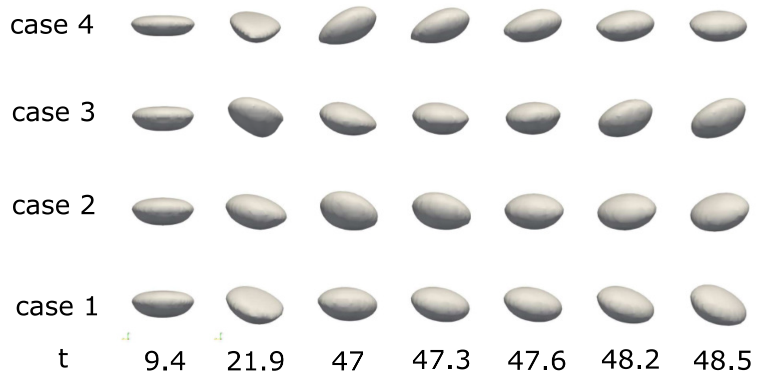

Figure 5.8: Temporal evolution of the bubble shapes at different times.

5.3.2 Wake Structure

As the bubble rises, an axi-symmetric toroidal ring develops and attaches to the bubble (t=9.4 in Figure 5.9). The flow around the bubble separates from the body at some point because of its excessive curvature and the vortices are not formed symmetrically around the bubble (t=18.8 in Figure 5.9). The asymmetric vortices change the pressure distribution along the surface and different lift forces develop on each side of the bubble, leading to the zig-zag motion of the bubble. For cases 1 and 2, the periodic hairpin vortex shedding can be found in the periodic zig-zag motion. The wake structures of both cases have a 2R mode, meaning double-sided periodic sequences of vortex rings [52, 124]. For cases 3 and 4, the vortex attached to the bubble is twisted and spiral, corresponding to the spiral motion of the bubble as seen in Figure 5.6(c) and (d). Different from the finding in Cano-Lozano et al. [52], the hairpin is present in the simulations performed in this work. At t=47 and t=62.6 (Figure 5.9(c) and (d)), the periodic shedding of the hairpin vortex with appearance of 2R mode can be clearly observed.

5.3.3 Vortex Dynamics

In this section we calculate the vorticity component in the X and Y directions and the norm of streamwise vorticity accumulated on the bubble surface,

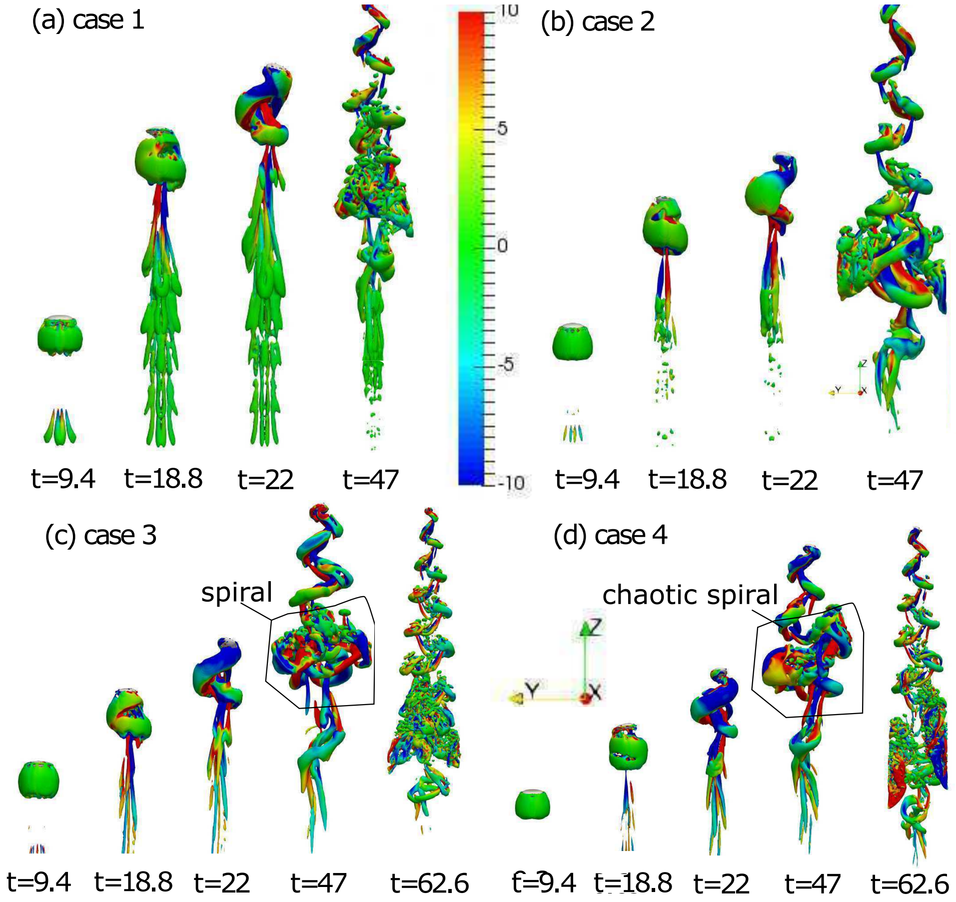

Figure 5.9: The vortex structures revealed by λ_2 criterion (with $\lambda_2 = 20$) at different times for different cases. The iso-vortices are color-coded with Ω_z.

that is $\tau_{(X,Y)} = \int_s \omega_{(X,Y)} dS$ and $|\tau_Z| = \int_s |\omega_Z| dS$ [105], where S is the bubble interface and $\omega_{X,Y}$ is the vorticity component in the X and Y directions. For cases 1 and 2 in the phase of straight path, the positive and negative vortices in the X and Y directions can balance each other (Figure 5.10). In the aperiodic zig-zag motion of the bubble, the oscillations of $\tau_{X,Y,Z}$ and $|\tau_Z|$ are aperiodic as well. In the phase of periodic zig-zag motion starting from about t=30, the periodic oscillations of τ_X and τ_Y are observed and the frequency is about 5 Hz, which is the same as that of the zig-zag motion as shown in Figure 5.7. The frequency of the oscillation of $|\tau_Z|$ is about 10 Hz (twice of the zigzag motion as well as τ_X and τ_Y), which is the same to the conclusion in [105]. In the paper of Zhang and Ni [105], they think that when the accumulation of $|\tau_Z|$ on the bubble surface reaches a critical value, the vortex shedding can be triggered. Here the critical values are different for the two cases and the value of case 2 is smaller, which is caused by the decrease of bubble volume due to the compressibility effect. In the work of Magnaudet and Mougin [125], they guess the critical value is probably related to the interface curvature, which can be proved in the present work. From Figure 5.7, the frequency and furthermost position of E are the same as that of $|\tau_Z|$.

For cases 3 and 4, in the phase of spiral motion (from t=6 to t=15), the frequencies of the oscillation of τ_X and τ_Y are quite large and amplitude is increasing, which is quite different from the aperiodic zigzag. In the transition phase from spiral to periodic zigzag, the oscillation of τ_X and τ_Y is irregular. When τ_X and τ_Y reach a certain value, the bubble enters into the zigzag motion, same to the flattened spiraling regime in [52]. The amplitude is larger than that of cases 1 and 2 but the frequency is almost the same: 5 Hz. A periodic oscillation of $|\tau_Z|$ is found and the frequency is 10 Hz, twice that of the zig-zag motion, which is the same as in cases 1 and 2, but with larger oscillation amplitude.

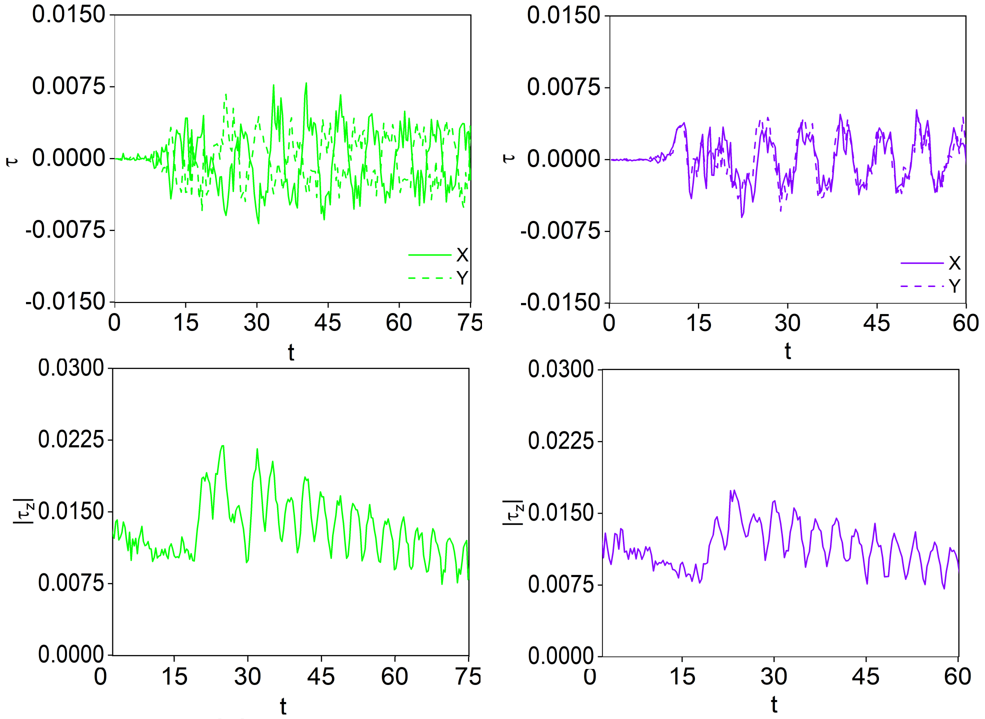

(a) case 1

(b) case 2

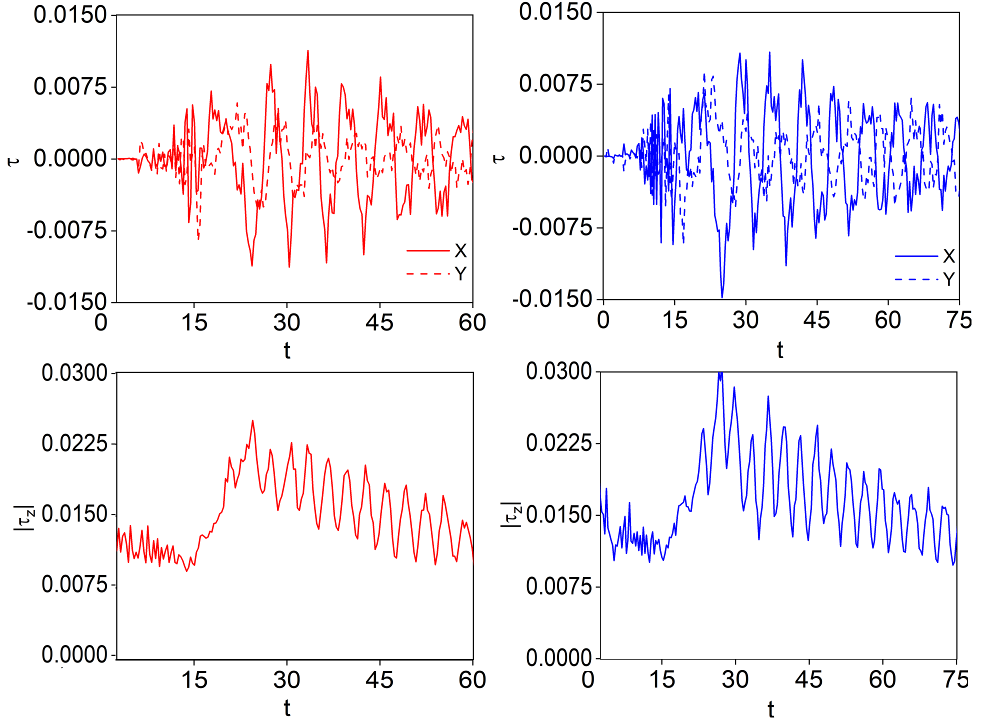

(c) case 3

(d) case 4

Figure 5.10: The time history of the vorticity component in X and Y direction ($\tau_{(X,Y)}$) and the magnitude of vorticity component in Z direction ($|\tau_Z|$) on the bubble surface for all cases.

5.4 Conclusion

In this chapter the rising bubble dynamics with heat transfer has been studied by investigating the path instability of compressible air bubbles rising in quiescent water considering the variation of water properties. The CLSVOF method has been adopted to track the interface. The equation of state for ideal gas was considered for the air in the bubble and The thermo-physical properties of water were considered as function of its temperature.
The simulations of the path instability of a compressible air bubble rising in quiescent water with variable thermo-physical properties are investigated for the first time. Four cases have been studied: 1) isothermal water and air (293 K); 2) hot air (363 K) in cold water (293 K); 3) isothermal water and air (363 K); 4) cold air (293 K) in hot water (363 K). All the cases present zig-zag motion but with differences. Three phases are observed in the bubble's trajectory in cases 1 and 2, namely straight path, aperiodic zig-zag and periodic zig-zag motion. In cases 3 and 4, the trajectory can be divided into four stages, straight path, spiral (chaotic spiral in case 4), aperiodic zigzag and periodic zigzag motion. The wake structures of all the cases are dominated by a 2R mode. The frequency of the aspect ratio oscillation is about 10 Hz, twice that of the zig-zag motion. The St number is about 0.2 for the periodic zig-zag motion. When the bubble passes the furthermost positions in teh trajectory, the aspect ratio decreases to the minimum value. In contrast, when the bubble passes the middle position, the aspect ratio reaches the maximum value. The frequency of the periodic oscillations of τ_X and τ_Y is 5 Hz, which is the same to that of zig-zag motion. The frequency of the oscillation of $|\tau_Z|$ is twice of the zig-zag motion as well as τ_X and τ_Y, but the same as that of the aspect ratio.

The air bubble rising in quiescent water yields the path instability, which has been studied by many researchers [3, 18, 52, 125]. The onset of path instability is thought to be related to the shape asymmetry and vortex shedding [52]. However, whether path instability leads to the vortex shedding or vice versa is still unclear. In addition, few researchers focus on the study of rising bubble at high Re ($\sim$ 1000). In this section, we conduct simulation on air bubble rising in quiescent water at high Re ($\sim$ 2000). Once the air bubble is released in the water, it rises due to the buoyancy and a boundary layer around the bubble is formed. The water motions are completely driven by the bubble rise. Due to the interaction of large inertia and small surface tension force, the bubble wobbling is observed first. As the bubble rises, the boundary layer separates from the bubble surface because of its excessive curvature (here the bubble wobbling speeds up the separation of the boundary layer) and the vortices are then formed. In addition, the bubble velocity increases as the bubble rises, which leads to the increase of the Re. Thus the vortices are not formed symmtrically at some point when the Re is large enough and different lift forces develop on each side of the bubble, which results in the bubble motion transvorce to the flow. In our simulation, τ_X and τ_Y oscillate earlier than the bubble displacement in X and Y direction. In the periodic zig-zag motion of the bubble, the hairpin structures with 2R mode control the turbulent motion by the parent-offspring mechanism.

For the simulated cases with different temperature, the differences of the zig-zag motion resutl from the variation of water temperature (function of temperature) and bubble volume change, which is studied for the first time. In Equations 5.2-5.5, the water viscosity is affected most by the variation of temperature, which influences the Re. Thus the oscillations of τ_X and τ_Y of cases 3 and 4 are observed earlier than that of cases 1 and 2 due to the large Re and the oscillation amplitudes of case 3 and 4 are also larger. For cases 1 and 2, the difference comes mainly from the variation of the bubble volume, which is caused by the air compressibility. For case 2, the bubble (363K) volume decreases once released in the water (293 K), which also decreases the Re. We can see that the oscillation amplitudes of τ_X and τ_Y of case 2 is smaller than that of case 1. Same conclusions can be obtained for cases 3 and 4. The bubble (293 K) volume of case 4 increases during its rise in water (363 K), which increases the Re. The oscillation amplitudes of τ_X and τ_Y of case 4 is larger than that of case 3. The novelty of this section lies on the comprehensive consideration of all kinds of factors affecting the path instability, including density, viscosity, surface tension, and bubble volume while the study of a single factor affecting the path instability has been reviewed in Section 1.2.2.

Chapter 6

Bubble Condensation

In this chapter, the rising bubble dynamics with heat and mass transfer are studied for the process of bubble condensation. Two mass transfer models, namely Lee model and Tanasawa model implemented in OpenFOAM, are assessed in this Chapter. The influences of subcooled temperature, bubble size, and fluid properties on the bubble dynamics during condensation are also studied. The assessment of the mass transfer models based on experimental data is included in section 6.1. The value of the empirical coefficient and the mesh size are determined. Results in 2D and 3D flow configurations are compared and a detailed analysis of the bubble condensation process is discussed in Section 6.2. Section 6.3 is devoted to the summary and conclusion.

The contents in this chapter have been published by the author in the journal of Nuclear Engineering and Design [126].

6.1 Assessment of the Phase Change Models

6.1.1 Problem Description

In the work of Liu et al. [51], the experimental data of Jo and Jo [127] has been used for the validation and assessment of their phase change models, which is also used in this thesis. An initial bubble with the diameter (D_0) of

3 mm and a subcooling of 5 K is simulated. The vapor and water were both at atmospheric pressure. The physical properties of water and vapor for the conditions of the experiment are listed in Table 6.1

Table 6.1: Physical properties of water and vapor.

Property	Liquid	Vapor
P(Pa)	101325	
T_{sat} (K)	373	
σ (N/m)	0.06	
h_{fg} (J/kg)	2.67×10^6	
μ (kg/(m s))	3×10^{-4}	1.23×10^{-5}
ρ (kg/m^3)	1000	0.59
C_p (J/kg K)	4181	2076
λ (W/m K)	0.68	0.025

To simulate the bubble condensation process, a cubic fluid domain with the dimension of $6D_0 \times 6D_0 \times 10D_0$ has been adopted, where D_0 is the initial bubble diameter. The boundary conditions are listed in Table 6.2. At the top wall boundary, inflow and outflow are possible. In OpenFOAM [95], the boundary condition "fixedFluxPressure" sets the pressure gradient to the provided value such that the flux on the boundary equals to the value specified by the velocity boundary condition. The boundary condition "totalPressure" describes the patch pressure by subtracting the dynamic pressure from the total pressure. The boundary condition "pressureInletOutletVelocity" represents an application of velocity inlet/outlet boundary condition to pressure boundaries. A zero-gradient condition is applied for outflow. The velocity is obtained from the patch-face normal component of the internal-cell value for the outflow.

Table 6.2: Boundary conditions for the simulation of bubble condensation.

boundary	bottom wall	top wall	side walls
volume fraction	zeroGradient	inletOutlet	zeroGradient
pressure	fixedFluxPressure	totalPressure	fixedFluxPressure
velocity	fixedValue (0 0 0)	pressureInletOutletVelocity	fixedValue (0 0 0)
temperature	zeroGradient	zeroGradient	zeroGradient

6.1.2 Lee Model

6.1.2.1 Influence of the Empirical Coefficient L

In order to decrease the deviation of the interface temperature from the saturation temperature, the value of the empirical coefficient L can take values in a wide range from 0.1 to 1×10^7 s^{-1} in different simulations. The optimum value of L depends on several factors that characterize the simulated flow, such as the flow rate, subcooling, mesh size and time step [77]. To study the effect of L on the bubble condensation and save computational cost, 2D numerical simulations are conducted. The mesh size is $D_0/50$ and the time step is 1×10^{-6} s. The Courant number is set to 0.1 for all the simulations in this paper. The results for different L values are displayed in Figure 6.1. The bubble condensation rate increases with increasing L because the mass transfer rate is proportional to L in Equation 2.27. When the value of L is 1.5×10^5 s^{-1}, the 2D simulation results agree well with the experimental data (the relative error is less than 15%).

6.1.2.2 Influence of Mesh Size

Figure 6.2 shows the effect of the mesh size on the simulation results with the Lee model. Different mesh sizes of $\Delta x/D_0 = 1/[50, 80, 100, 160]$ are used. The time step is set to 1×10^{-6} and the Courant number is set to 0.1. The empirical coefficient L for all the cases are 1.5×10^5 s^{-1}. The condensation rate increases as the mesh size becomes larger, which means that a converged solution cannot be obtained. The total mass transfer rate is calculated as [51]:

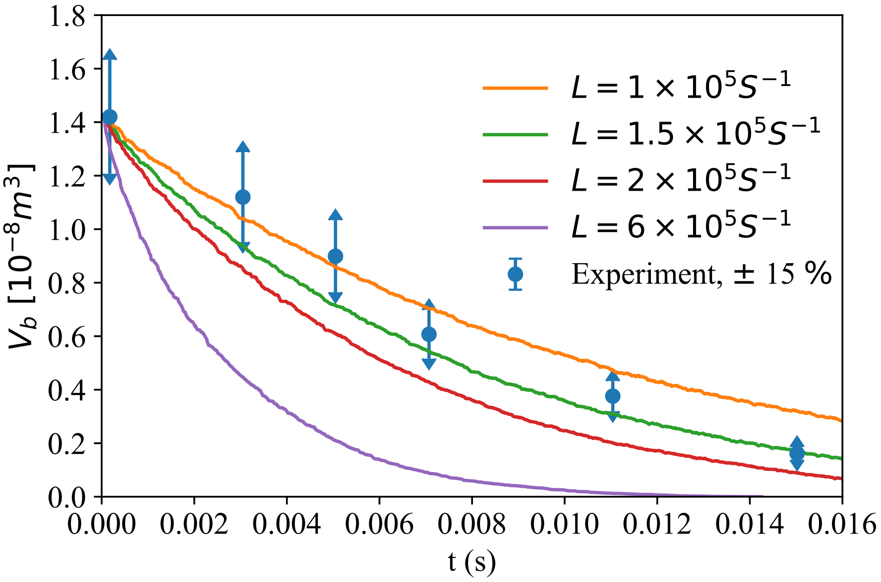

Figure 6.1: Effect of empirical coefficient on the variation of the condensing bubble volume for Lee model.

$$\dot{M} = \sum_i \alpha_v \dot{m} V_{cell} \tag{6.1}$$

Therefore, the condensation mass transfer rate is not only dependent on the volumetric mass source term $\dot{m}$ but also on the volume of each cell. Besides, the interface advection is calculated by the MULES scheme and the interface is limited to a 2- to 3-cell layer. As a result, the interface volume increases with the increase of the mesh size, resulting in a higher mass transfer rate. It is also noteworthy to mention that the coarsest mesh gives best results. Actually, a coarse mesh results in increased numerical diffusion and the turbulent diffusion is dampened in 2D simulation. Therefore it is possible that the numerical diffusion compensates the missing turbulent diffusion in 2D simulation.

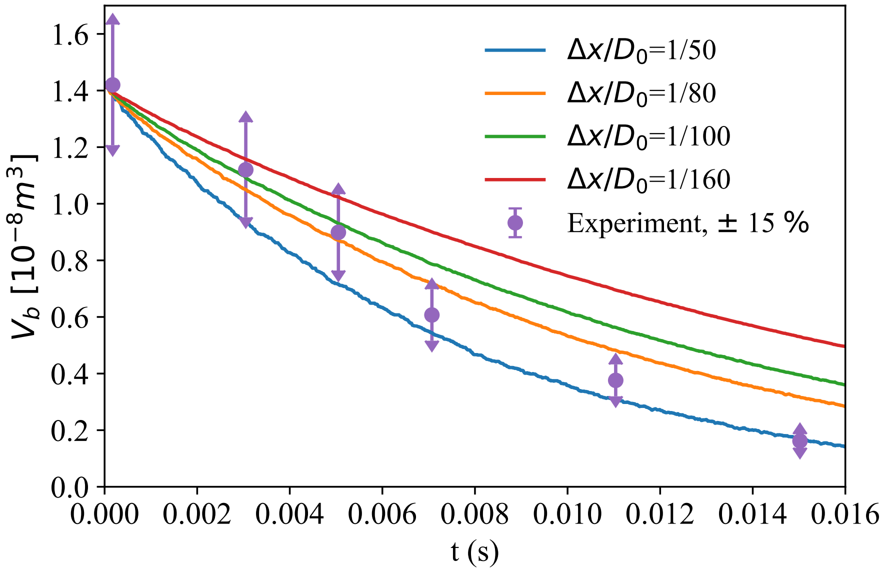

Figure 6.2: Effect of mesh size on the variation of the condensing bubble volume for Lee model.

6.1.2.3 2D- vs 3D-Simulation

In this section the results of bubble condensation using Lee model are compared for 2D- and 3D-simulations. The mesh size in both cases is $D_0/50$. The empirical coefficient L equals 1.4×10^5 s^{-1}. The variations of the bubble volume and rising position during condensation are shown in Figure 6.3. The bubble volume of the 2D-bubble is calculated as

$$V_b = \frac{4}{3}\pi \left(\frac{A_b}{\pi}\right)^{\frac{3}{2}} \tag{6.2}$$

The variations of the bubble volume in the 2D- and 3D-simulation are almost the same, but the rising bubble positions are quite different. The 3D-bubble rises much faster than the 2D-bubble. The reasons may be: 1) the shapes of the 2D-bubble and 3D-bubble are different, thus the lift and drag force are different; 2) the mass transfer rate across the surface of the 2D- and 3D-bubble is different from each other, thus the flow fields around the bubbles are different; 3) the turbulent diffusion is dampened in 2D simulation. The shape

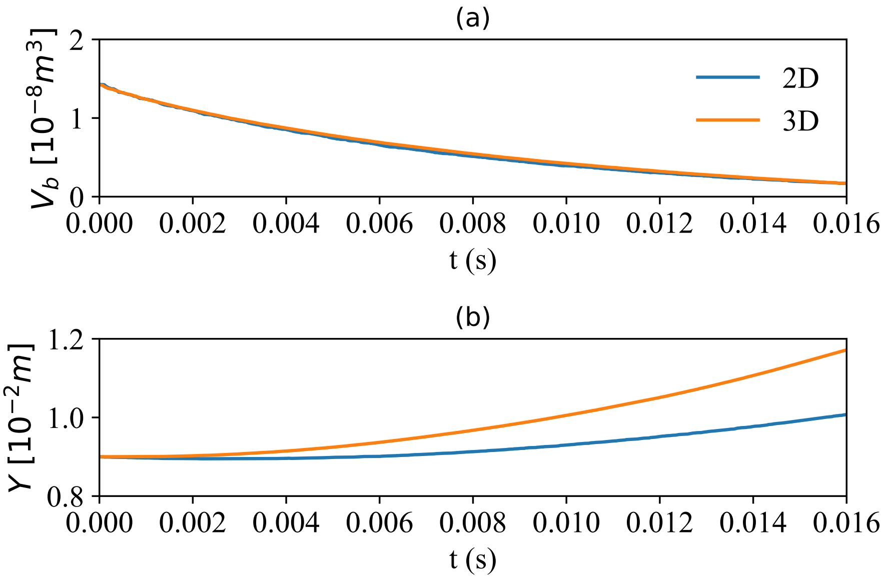

Figure 6.3: Comparison of 2D- and 3D-simulation results with respect to a) the bubble volume, and b) rising position.

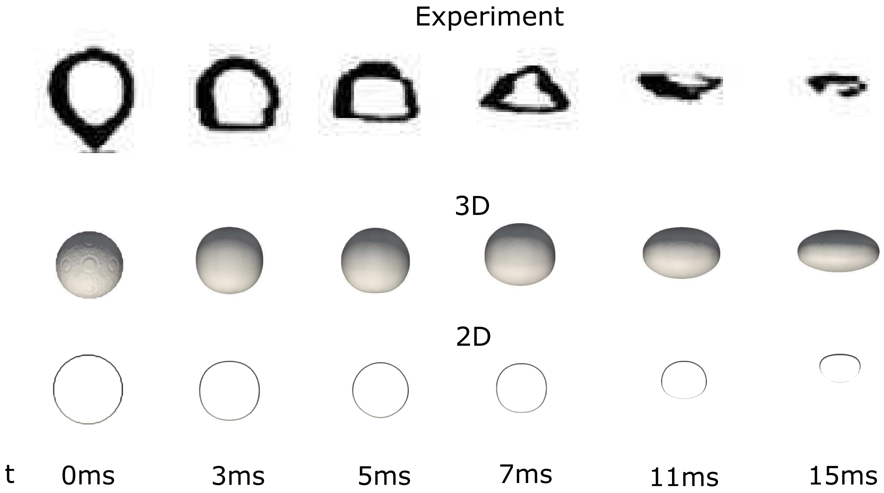

Figure 6.4: Comparison of the experimental bubble shape with the simulation results.

evolution of the bubble in the 2D- and 3D-simulations is shown in Figure 6.4. The bubble shape is extracted as α=0.5. The 3D-simulation results agree better with the experimentally observed bubble shape´s evolution [127] than that of the 2D-simulation.

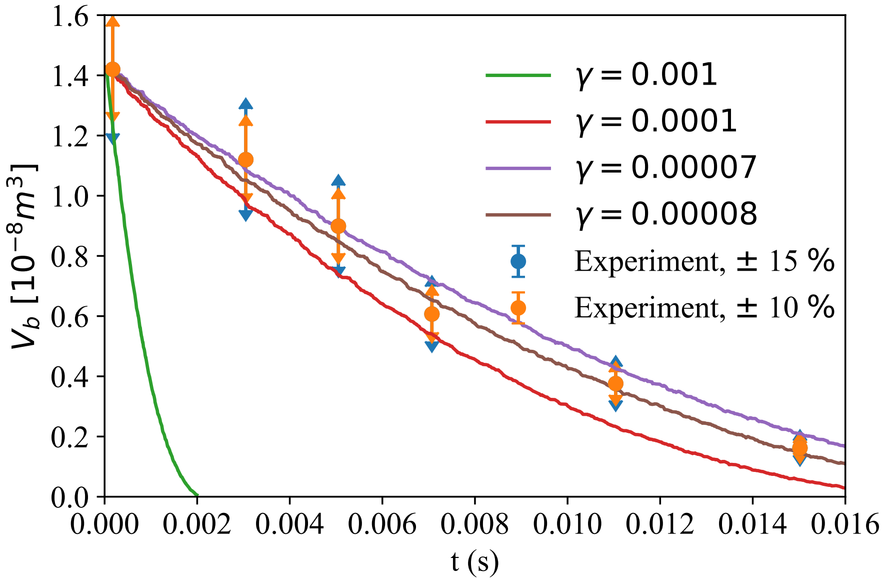

Figure 6.5: Effect of empirical coefficient γ on the variation of the condensing bubble volume for Tanasawa model.

6.1.3 Tanasawa Model

6.1.3.1 Influence of the Empirical Coefficient

In Tanasawa model the empirical coefficient γ is an unknow quantity. In this section the simulation results obtained using different γ walues are compared to experimental data in order to determine the best value of γ.

Figure 6.5 shows the variation of the bubble volume with different empirical coefficients γ. Reasonable results can be obtained with $\gamma = 0.00008$ and $\gamma = 0.00007$. But the relative error of the results with $\gamma = 0.00008$ is less than 10%, while it is 15% for $\gamma = 0.00007$. The value of γ agrees with the conclusion of Marek and Straub [99] that γ lays below 0.1 for stagnant liquid surface. Therefore, the optimal value of γ is chosen as 0.00008 for the 2D-simulation.

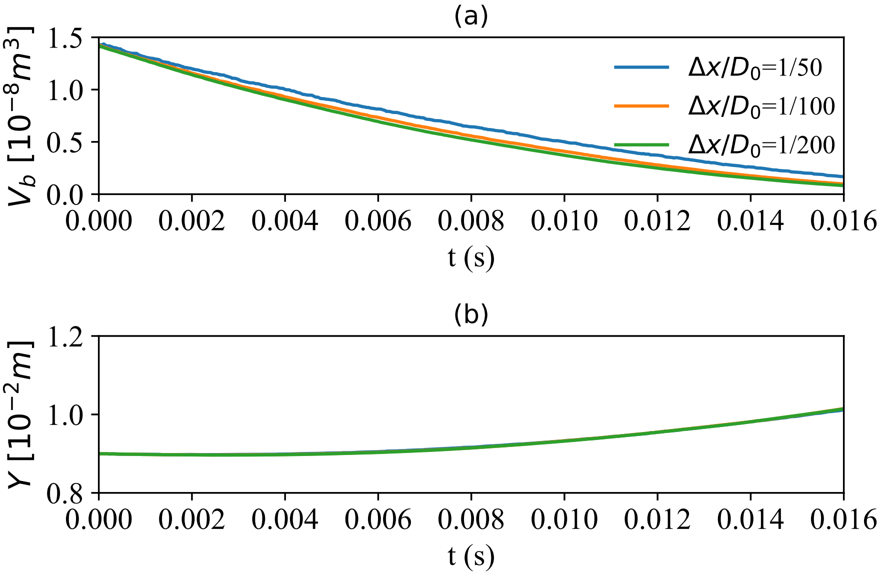

Figure 6.6: Effect of mesh size on the variation of a) the condensing bubble volume, and b) bubble rising position for Tanasawa model.

6.1.3.2 Influence of Mesh Size

The influence of the mesh size on the bubble condensation is shown in Figure 6.6. The simulation is 2D and $\gamma = 0.00008$. The mesh sizes of the simulation are $\Delta x/D_0 = 1/[50, 100, 200]$. The simulation results converge with $\Delta x/D_0 = 1/100$.

6.1.3.3 2D- vs 3D-Simulation

The 2D- and 3D-simulation results of bubble condensation are compared in this section. The mesh size is $\Delta x/D_0 = 1/100$. The empirical coefficient is $\gamma = 0.00007$. As shown in Figure 6.7, the condensation rate of the 3D-simulation is larger than that of the 2D-simulation. Besides, the 3D-bubble rises much faster than the 2D-bubble, which is a similar conclusion to that reached using Lee model. The reasons are also the same to that of the Lee model.

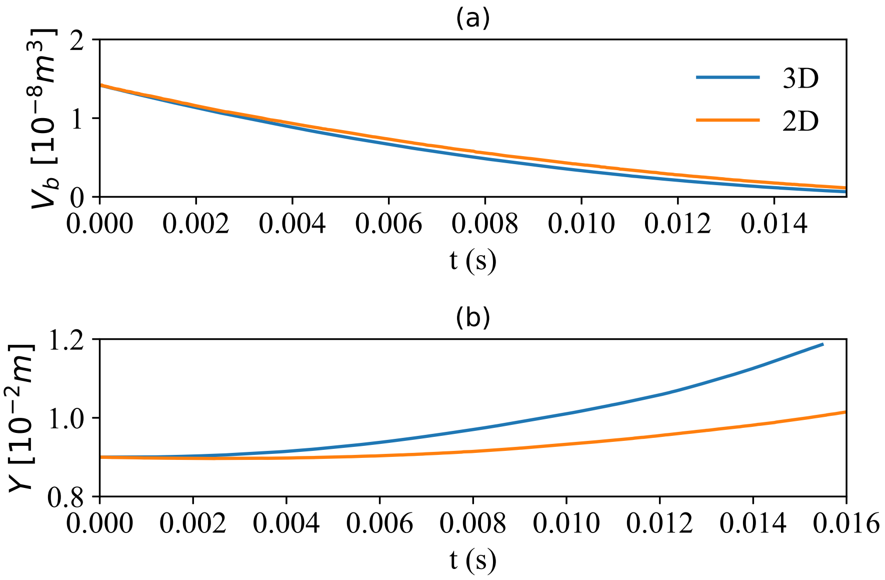

Figure 6.7: Comparison of 2D- and 3D-simulation results with respect to a) the bubble volume, and b) the rising bubble position.

6.2 Results

6.2.1 Single Bubble Condensation

Based on the discussion in Section 6.1, a 3D-simulation of bubble condensation using Tanasawa model has been conducted with a mesh size of $\Delta x/D_0 = 1/100$. Table 6.1 lists the physical properties of water and vapor used for the simulation and γ is equal to 0.00006. We compare the simulated bubble volume with the experimental data as shown in Figure 6.8 and the relative error is less than 5%. We can see in Figure 6.9 that the simulated bubble shape evolution agrees well to the experimental data.

During the bubble rise, its dynamics are affected by many factors, including the surface tension, viscous force, gravitational force. For the bubble condensation, it is also affected by the mass flow and bubble volume variation caused by the phase change. The velocity field around the bubble during condensation is displayed in 6.10. At the initial time the bubble is spherical

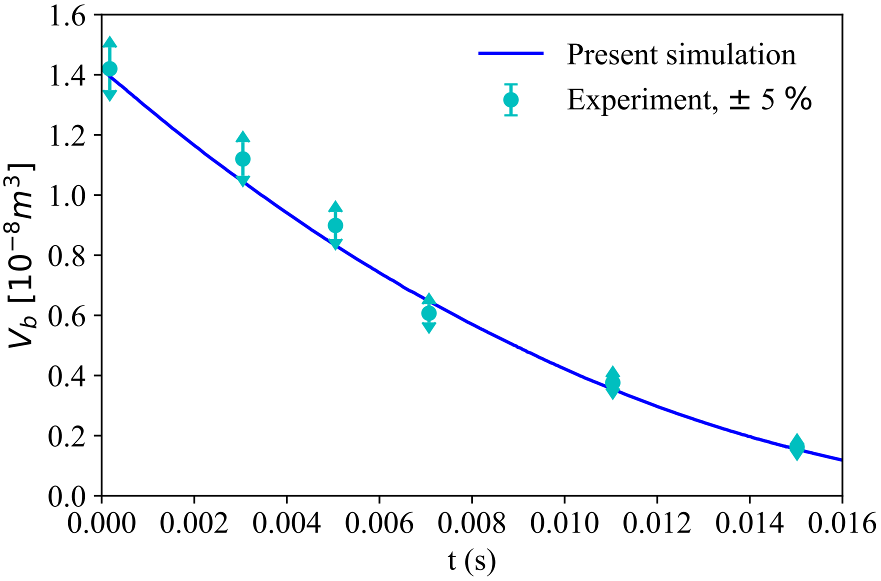

Figure 6.8: Comparison of simulation results of bubble volume to the experimental data.

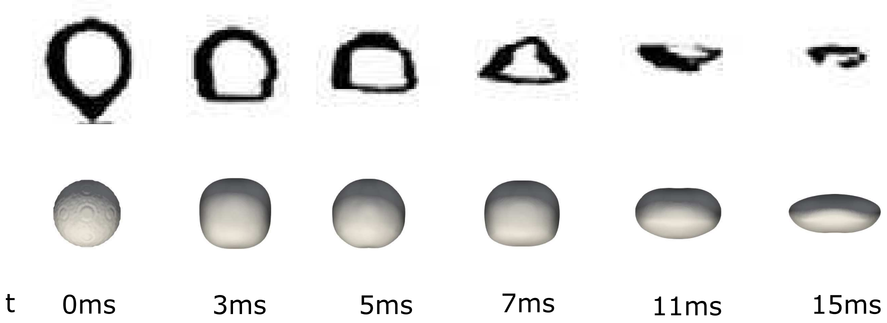

Figure 6.9: Comparison of simulation results of bubble shape evolution to the experimental data.

in Figure 6.9. The subcooled water flows into the bubble from all directions due to the bubble's condensation (t=1 ms in Figure 6.10). At the same time, the bubble begins to rise due to buoyancy having to resist the downflow of the subcooled water above it caused by the condensation process. The upward water flow under the bubble has the same direction as the rising bubble. A deformation from a spherical to an ellipsoidal shape is observed.

The time histories of the mass transfer rate across the interface and of the

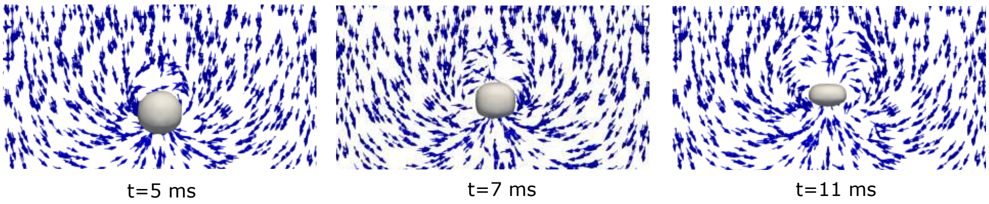

Figure 6.10: Evolution of the velocity field around the bubble during condensation.

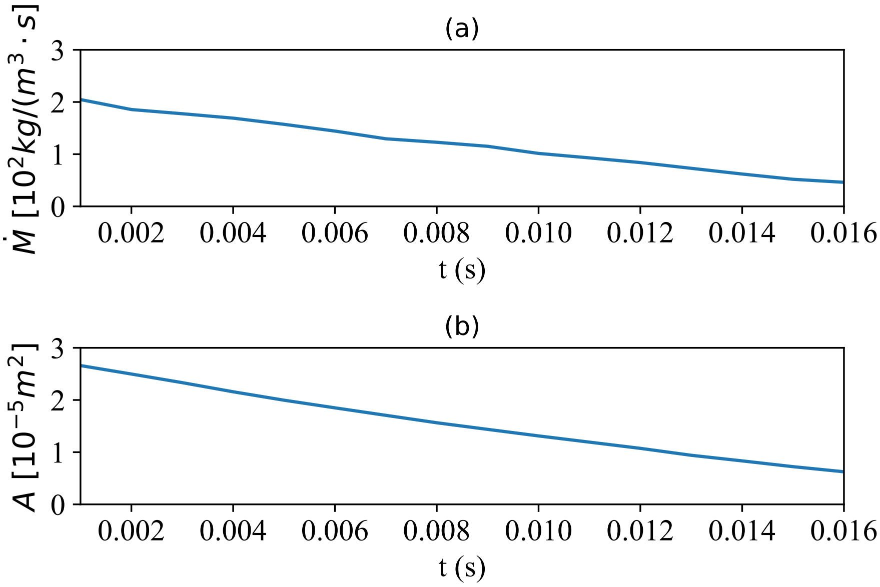

Figure 6.11: Time history of a) mass transfer rate, and b) interface area during condensation.

interface area are shown in Figure 6.11. We can see that the mass transfer rate is decreasing due to the decrease of the interface area.

6.2.2 Influence of Bubble Diameter

In this section, the influence of bubble size on the bubble condensation process is studied. The influence of the bubble size can be attributed to two aspects: 1) the increase of the bubble diameter leads to the higher inertia force, thus increasing the bubble deformation; 2) the turbulence effect of larger bubble is stronger, thus affecting the heat and mass transfer between

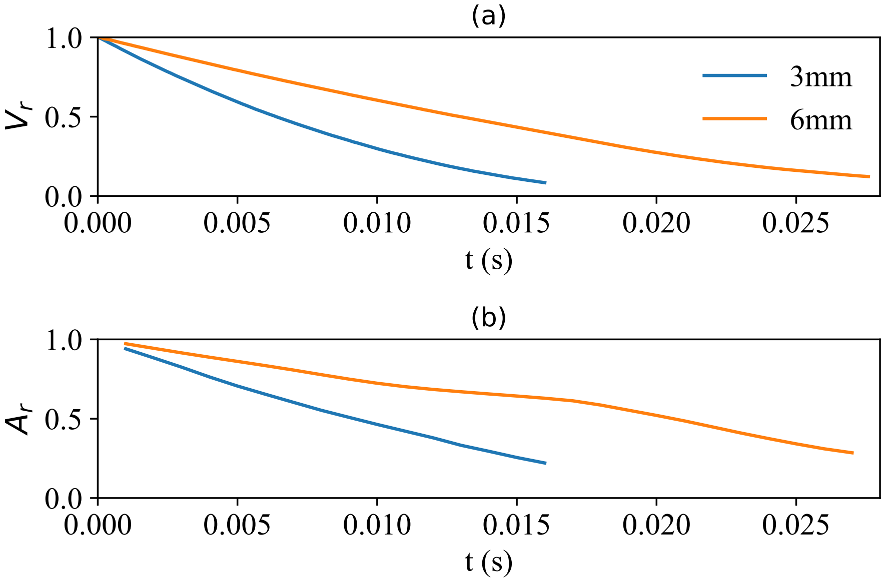

Figure 6.12: Effect of the bubble size on condensation, a) time history of the normalized bubble volume, b) time history of the normalized bubble surface area.

the vapour bubble and cold bulk. Figure 6.12 shows the effect of the bubble size on the bubble condensation. V_r refers to the ratio of the instant bubble volume to the initial bubble volume and A_r is the ratio of the instant bubble surface area to the initial bubble surface area. A longer condensation time is observed for a bigger bubble size.

As discussed before, the bubble ($d_0 = 3\,\mathrm{mm}$) is deformed from spherical to oblate. However, the deformation of the larger bubble ($d_0 = 6\,\mathrm{mm}$) is more severe due to the increase of inertia force, which increases the contact area of the vapour bubble with the cold bulk. Besides, the increase of the bubble diameter increases the bubble Re, which greatly influences the shear stress between the rising vapor bubble and the motionless bulk, resulting in the turbulence inside the bubble more intensive and the thermal field around the bubble unstable [25, 93]. As a result, the surface wave is formed on the bubble surface (t=0.022 s) in Figure 6.13 (b), which enlarges the effective area of condensation, thus increasing the mass transfer rate. In our simulations, the

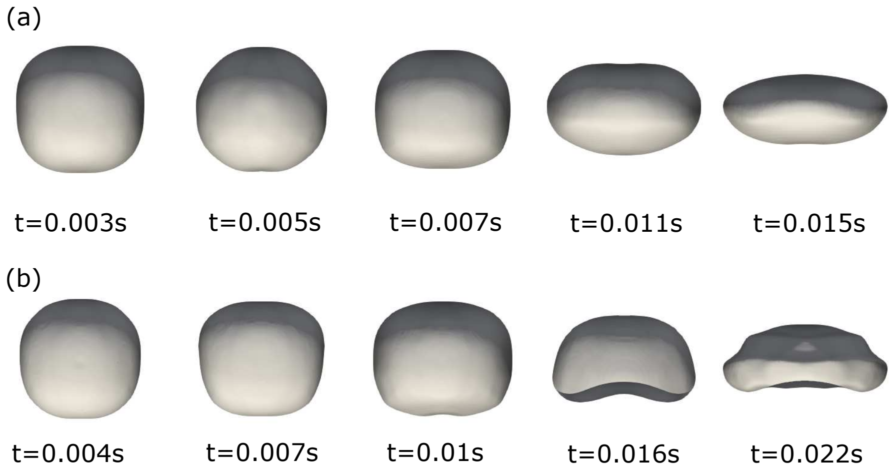

Figure 6.13: Effect of the bubble size on condensation, a) $d_0 = 3\,\mathrm{mm}$, b) $d_0 = 6\,\mathrm{mm}$.

Table 6.3: The average mass transfer rate for different subcooling temperature.

T_{sub} (K)	$\dot{m}$ (kg/(m$^3 \cdot$ s))
5	0.01198
10	0.03539
20	0.0468

average mass transfer rates are 0.01198 kg/(m^3 s), and 0.02764 kg/(m^3 s) for 3 mm bubble, and 6 mm bubble, respectively.

6.2.3 Influence of Subcooling

The increase of subcooling can result in the increase of the mass flux across the interface, thus complicating the bubble dynamics during the condensation process. The influence of subcooling on the bubble's condensation is shown in Figure 6.14. In the simulations, the initial bubble diameter is 3 mm. Three subcoolings 5 K, 10 K, and 20 K are analyzed. The mass transfer rate increases with the increase of subcooling as displayed in Table 6.3.

The shape evolution with different subcooling during bubble condensation is compared shown in Figure 6.15. With the increase of the subcooling, the bubble experiences more severe deformation. For $\Delta T_{sub} = 20$ K, the bub-

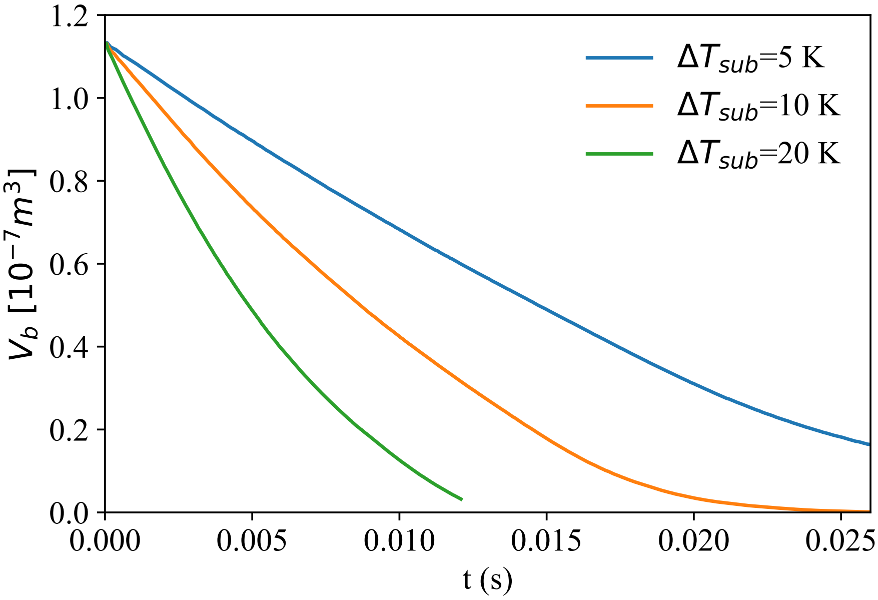

Figure 6.14: The effect of the subcooling on the condensation.

ble collapse more quickly and the bubble becomes from spherical, ellipsoidal to skirt, which is quite different from other two cases. Actually, the higher subcooing induces stronger condensation (higher mass flux across the interface), which accelerates the instability of the bubble surface [93]. Besides, the turbulence in the thermal field on the periphery of the bubble increases and uneven local condensation at the bubble surface might occure at higher subcooled temperatuer, leading to the deformation of the interface [91]. The bubble rising velocity with different subcooling is shown in Figure 6.16. With the increase of the subcooled temperature, the rising velocity also increases, which can also enhance the heat transfer.

6.2.4 Influence of Liquid Viscosity

The effect of the liquid viscosity on the bubble condensation is studied in this section. Three cases with different liquid viscosity, $\mu = [3 \times 10^{-4}, 3 \times 10^{-2}, 3]$ kg/(m s) are simulated. The initial bubble diameter is 3 mm with a subcooling of 5 K. The other physical properties of the water and vapor

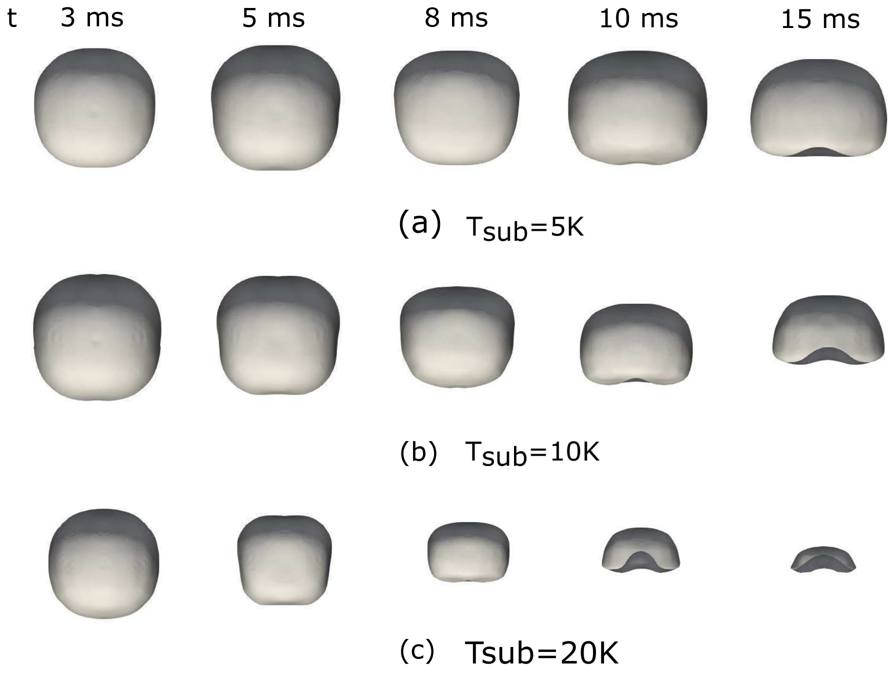

Figure 6.15: The effect of the subcooling on the shape variation during condensation.

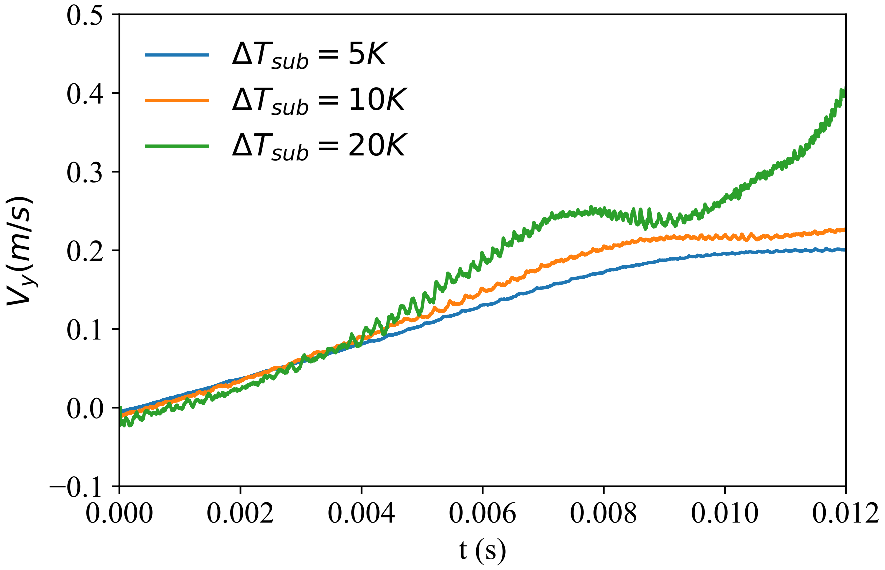

Figure 6.16: The effect of the subcooling on the bubble's rising velocity during condensation.

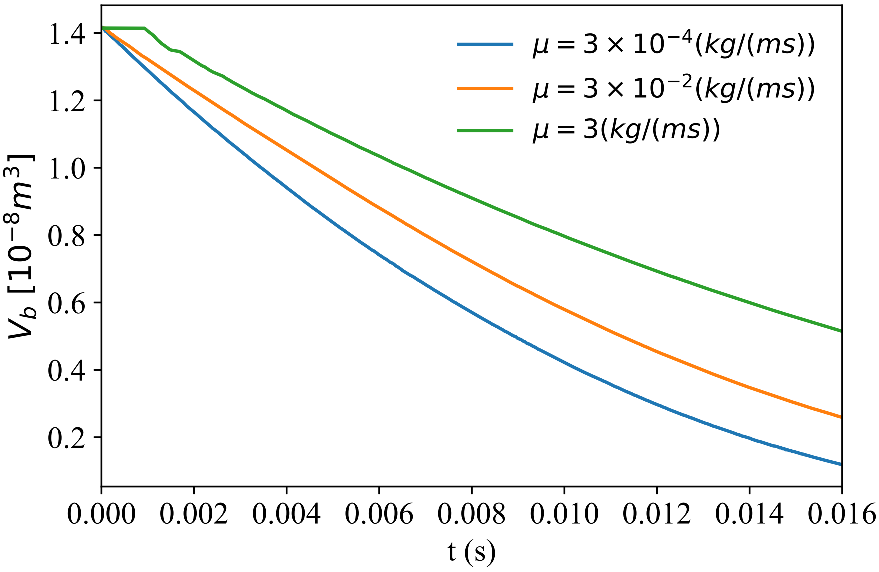

Figure 6.17: Effect of the liquid viscosity on the bubble volume during condensation.

are kept unchanged. The time history of the bubble's volume variation is shown in Figure 6.17. With the increase of the liquid viscosity, the mass transfer rate and the bubble rising velocity both decrease (Figure 6.18). The increase of the liquid viscosity restricts the bubble rising and deformation, which reduces the convective heat transfer. For the liquid viscosity $\mu = 3$ kg/(m s) the bubble is nearly still (the green line in Figure 6.18). The shape evolution of the bubble with different liquid viscosity is displayed in Figure 6.19. The bubble keeps its spherical shape for large liquid viscosity.

6.2.5 Influence of Surface Tension

In this section the effect of the surface tension on the bubble's condensation is investigated. Three cases with the surface tension coefficients $\sigma = [0.002, 0.06, 0.2]$ kg/s^2 are simulated. The initial bubble diameter is 3 mm. The subcooling is 5 K. The other physical properties of the water and vapor are kept unchanged. The effect of the surface tension on the bubble volume variation is shown in Figure 6.20. From t=0 s to t=0.013 s, the bubble's

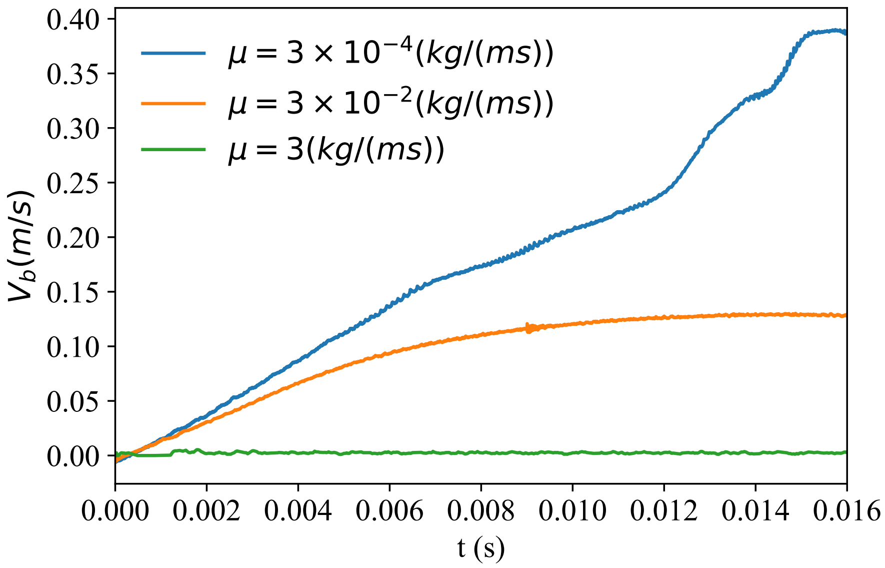

Figure 6.18: Effect of the liquid viscosity on the bubble rising velocity during condensation.

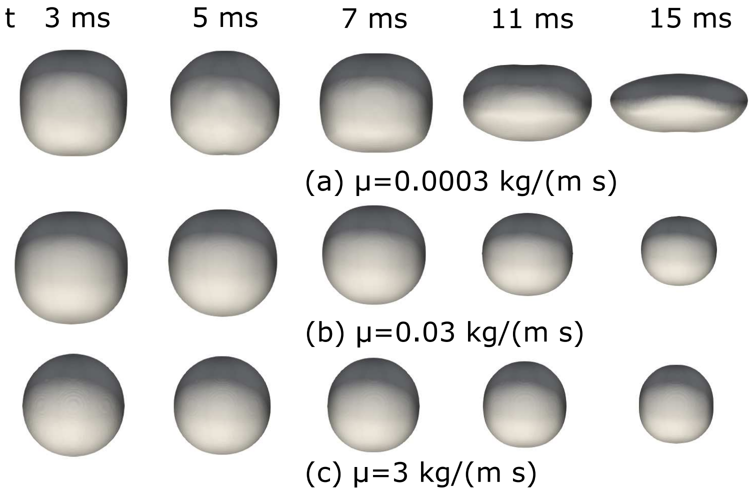

Figure 6.19: Effect of the liquid viscosity on the bubble rising velocity volume during condensation.

volume decreases with the increase of the surface tension but it's the other way around after t=0.013 s. The time-average bubble volume is calculated for the three cases and the case with $\sigma = 0.002$ kg/s^2 is found to exhibit the smallest average bubble volume. Therefore, the decrease of the surface

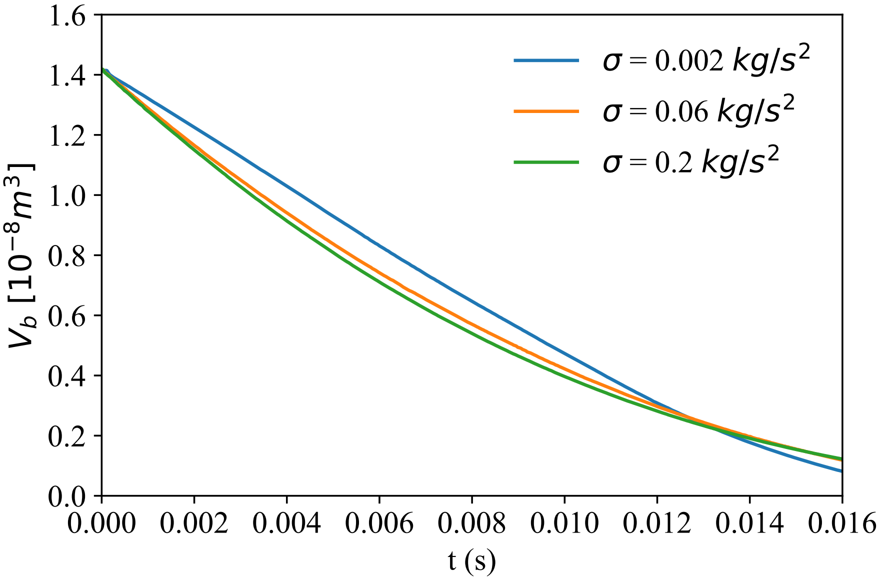

Figure 6.20: Effect of the surface tension on the bubble's volume during condensation.

tension increases the condensation rate. The role of the surface tension is to keep the bubble spherical. Therefore, with the decrease of the surface tension, the bubble is easier to deform and has a larger surface area than the spherical bubble. The large bubble surface (vapor-liquid interface) enlarges the effective area of condensation, thus resulting in the acceleration of bubble condensation.

To verify our findings, the bubble surface area with different surface tension is plotted in Figure 6.21. With the decrease of the surface tension, the bubble surface area increases due to large bubble deformation. The shape evolution of the bubble with $\sigma = 0.002 \mathrm{kg/s^2}$ is displayed in Figure 6.22. The bubble's central breakup is observed and clarified in our previous paper [5] and [38]. The appearance of central breakup enlarges the effective condensation area. The time-average mass transfer rate across the interface is compared with different surface tension in Table 6.4. The average mass transfer rate is the highest with the smallest surface tension ($\sigma = 0.002 \mathrm{kg/s^2}$).

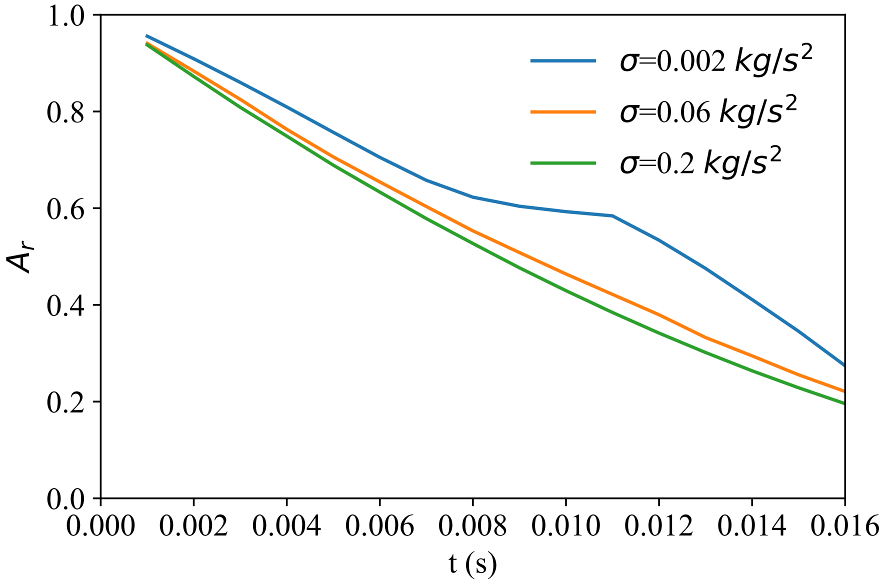

Figure 6.21: Effect of the surface tension on the bubble's surface area during condensation.

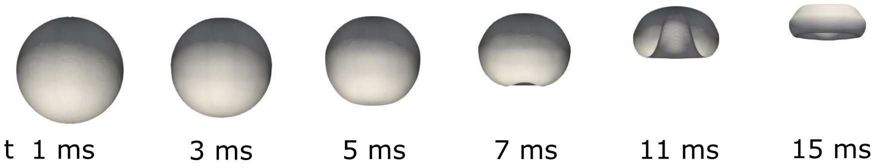

Figure 6.22: Shape evolution of the bubble with $\sigma = 0.002\,\mathrm{kg/s^2}$.

6.3 Conclusion

In this chapter, the phase change models, Lee and Tanasawa model, are assessed and analyzed for a single bubble condensation by comparing to the experimental data. Different aspects, including the empirical coefficient, mesh size and the comparison of 2D and 3D simulation are covered. The main conclusions are summarized below.

For the Lee model, the mesh-independent results cannot be obtained due to the dependence of the mass source term on the volume of the mesh cell. Therefore, the Tanasawa model is adopted for the simulation of bubble condensation as the mesh-independent results are obtained, where mesh size

Table 6.4: The average mass transfer rate for different surface tension.

σ (kg/s^2)	$\dot{m}$ (kg/(m$^3 \cdot$ s))
0.2	0.01135
0.06	0.01198
0.002	0.01431

$\Delta x/D_0 = 1/100$ is properly converged. The mass transfer rate increases with the increase of γ. The results (2D-simulation) obtained with $\gamma = 0.00008$ agree well with the experimental data and the relative error is less than 10%. By comparing the 2D and 3D simulation results, the variation of the bubble volume is almost the same in both cases, but the 3D bubble rises faster than the 2D bubble during the condensation process. The reasons may be: 1) the diverse shapes of the 2D and 3D bubbles leads to the different lift and drag force; 2) the mass transfer rate across the surface of the 2D and 3D bubbles is different from each other, thus the flow fields around the bubbles are different; 3) the turbulent diffusion is dampened in 2D simulation.

The increase of the bubble diameter increases the bubble Re, which greatly affects the shear stress between the rising vapor bubble and the motionless bulk, resulting in the turbulence inside the bubble more intensive and the thermal field around the bubble unstable [25, 93]. As a result, the surface wave is formed on the bubble surface. The surface wave on the bubble surface enlarges the effective area of condensation, thus increasing the mass transfer rate.

With the increase of the subcooling, the condensation becomes stronger (higher mass flux across the interface), which accelerates the instability of the bubble surface. Besides, the turbulence in the thermal field on the periphery of the bubble increases and uneven local condensation at the bubble surface might occur at higher subcooling, leading to the deformation of the interface. The breakup of the vapor bubble ($D_0 = 6$ mm) is observed with $\Delta T_{sub} = 20$ K due to the appearance of the surface wave caused by the intensive liquid motion in the rear of the bubble and the high subcooling, which brings about a Rayleigh-Taylor instability forming on the bubble surface.

Table 6.5: Summary of different factors affecting the bubble condensation.

factors	influences	keywords
bubble size	$d_0 \uparrow$, $\dot{m} \uparrow$	Re, shear stress, surface wave
ΔT_{sub}	$\Delta T_{sub} \uparrow$, $\dot{m} \uparrow$	mass flux, bubble deformation, condensation area
viscosity	$\mu \downarrow$, $\dot{m} \uparrow$	convective heat transfer
surface tension	$\sigma \downarrow$, $\dot{m} \uparrow$	central breakup, condensation area

The increase of the liquid viscosity restricts the bubble rising and deformation, and reduces the convective heat transfer, which decreases the condensation rate. With the decrease of the surface tension, the bubble is easier to deform and has a larger surface area than the spherical bubble, which results in the acceleration of bubble condensation.

Chapter 7

Conclusion and Outlook

7.1 Conclusion

The objective of the thesis is to numerically study the bubble dynamics with heat and mass transfer. The bubble rising in quiescent liquid is a fundamental problem concerning with many engineering applications. The bubble shape and path are affected by the interaction of the inertia, viscous force and surface tension force. When the heat and mass transfer are considered, the rising bubble dynamics are also affected by the variation of the physical properties, the volume change of the bubble, and the mass transfer across the interface, which is a quite complex problem. To solve this problem, the thesis is divided into three parts, 1) bubble dynamics without heat and mass transfer; 2) bubble dynamics with heat transfer; 3) bubble dynamics with heat and mass transfer (bubble condensation). To conduct the numerical simulation, VoF method is adopted to track the interface. The Continuous Surface Force model is used to calculate the surface tension of the interface between the bubble and liquid. Two phase change models, Lee model and Tanasawa's model, are assessed with a single bubble condensation. After evaluation, Tanasawa model is adopted to simulate the bubble condensation, and multiple factors affecting the bubble condensation are analyzed based on the simulation results.

For the isothermal rising bubble without heat and mass transfer, the oscillatory phenonmena and central breakup are simulated and analyzed to obtain a basic understanding of the rising bubble dynamics.

Due to the coupling of the bubble shape, path and wake, the bubble with path instability rises usually following zigzag, spiral or combination of both. We simulate an 8 mm air bubble rising in quiescent waterThe bubble wobbling has two roles: (1) the excessive curvature speed up the separation of the boundary layer; (2) the velocity peaks (Re) results in the formation of asymmetrical vortices. The oscillation frequencies (6Hz, St=0.22) of the bubble movement,the vorticity accumulated on the bubble surface, the lift force and viscous force are the same while the oscillation frequency of the aspect ratio E is twice of that of the bubble movement. The forces exerted on the bubble seem to oscillate firstly, earlier than that of the bubble movement and the vorticity. The hairpin structures are tilted and interacted with one another during the spiral motion. The velocity fluctuations in vertical direction are more intense than that in the lateral direction, all of which present linear increase while the dimensionless kinetic energy presents a quadratic increase.

For two inline bubbles, three cases are considered with the initial distance $h = [2d, 4d, 6d]$. When $h = 2d$, the terminal velocity of TB increases over time due to the added mass effect and TB collides with LB before it enters into the spiral motion. We also observe the central breakup of TB due to its elongation. When $h = 4d$, the two bubbles interact in the straight rising path and the transition phase. The same velocity oscillations are observed when TB is unaffected by LB. After that, the velocity of TB increase due to the interaction with LB and the velocity oscillation of TB is bigger than that of LB. When $h = 6d$, the distance of the two bubble is far enough that both yield path instability. The wake generated by LB can cause the lateral motion of TB (moving either towards the wake center or away from it), which depends on the position of TB in the wake of LB and the intensity of the vortices TB encounters. Compared to the case of single bubble, the liquid volume-averaged velocity created by two inline bubbles is doubled before TB enters the wake region of LB (t'=10) and is less than the doubled value after TB enters the wake region of LB. The total liquid kinetic energy transferred from two inline bubbles is four times of that from single bubble before t'=10 and less than the four times after that due to the wake effect of the LB.

Due to to the difficulty in creating large spherical bubbles experimentally, the central breakup of a large spherical bubble is rarely studied experimentally. But it is encountered in many natural and engineering applications. We analyzed the hydrodynamics during the central breakup process. Different influencing factors on the central breakup behaviors are discussed. The pressure difference between the top and bottom of the bubble leads to the formation of the liquid jet. The jet velocity is much higher than the bubble rising velocity. The collision of the liquid jet with the bottom and top of the bubble create high pressure regions. After the central breakup, the gas velocity around the liquid jet inside the toroidal bubble is larger than that of the gas in other places, which results in the formation of the protrusion. The appearance of the protrusion elongates the bubble and increases the bubble rising velocity.

The central breakup behaviors of a large spherical bubble are affected by many factors, which are summarized with four dimensionless factors, Ga, Eo, ρ_r and μ_r. Since $Ga \propto R^{3/2}$ and $Eo \propto R^2$, the variation of the bubble size changes Ga and Eo to a larger extent compared to other factors. The liquid density plays an important role in the central breakup process because both Ga and Eo are linear function of the liquid density. The increase of Ga number (decrease of liquid viscosity) can lead to larger liquid jet velocity. However, no obvious increase of the bubble rising velocity and liquid jet velocity is observed with the increase of Eo number (decrease of surface tension coefficient) while keeping Ga number unchanged.

The influence of the density and viscosity ratios on the bubble is studied by changing the gas density and viscosity. With the increase of the density ratio (increase of the gas density), the bubble rising velocity and jet velocity decrease. The variation of the viscosity ratio mainly influences the circulation inside the bubble. Therefore the appearance of the protrusion is related to ρ_r and μ_r in addition to Ga and Eo.

With the increase of the aspect ratio, the bubble rising velocity becomes smaller. The jet velocity is almost the same except for the case of aspect ratio $E = 0.3$ (highly deformed bubble). This is due to the appearance of the local high pressure zone on the bottom of the bubble, resulting from the collision of the liquid jet with the bubble bottom. If we decrease the initial vertical bubble length, both the bubble rising velocity and the jet velocity become smaller. For $Z/Z_0 = 0.5$, peripheral breakup instead of central breakup is observed. The detached ring-like structure is broken into satellite bubbles. For the bubble with different aspect ratio E and constant volume, both V_{bubble} and V_{jet} decrease with the increase of the aspect ratio.

We further simulate two inline toroidal bubbles. For $h = 2d$, the leading and trailing bubbles do not influence each other. However, for $h = 1.5d$, the leading bubble greatly affects the trailing one. The velocity of the trailing bubble becomes larger than that of the leading one. The trailing bubble elongates due to the shielding effect of the leading bubble. The elongation of the trailing bubble leads to the peripheral breakup. The pinch off singularity yields the contraction of the lower edge of the upper part of the trailing bubble, thus resulting in the formation of the third toroidal bubble. Based on the above analsis, we summarized a linear relation between the jet (bubble) Reynolds number and Ga number.

The second part is the study of the rising bubble dynamics with heat transfer which is encountered in many engineering applications. Besides, all the physical properties, including density, viscosity, surface tension and thermal conductivity, are functions of temperature and pressure. Therefore it is crucial to account for the variation of thermo-physical properties and the compressibility of air for the investigation of bubble rising dynamics in consideration of the temperature difference between the bubble and the surrounding fluid. We simulate the path instability of a compressible air bubble rising in quiescent water with variable thermo-physical properties for the first time. Four cases are investigated: 1) isothermal water and air (293 K); 2) hot air (363 K) in cold water (293 K); 3) isothermal water and air (363 K); 4) cold air (293 K) in hot water (363 K). All the cases present zigzag motion but with distinctions. I observe three stages of trajectory in case 1 and 2, straight path, aperiodic zigzag and periodic zigzag motion. In case 3 and 4, the trajectory can be divided into four stages, straight path, spiral (chaotic spiral in case 4), aperiodic zigzag and periodic zigzag motion. The wake structures of all the cases are dominated by a 2R mode. The frequency of the aspect ratio oscillation is about 10Hz, twice that of the zigzag motion. The St number is about 0.2 for the periodic zigzag motion. When the bubble passes the furthermost positions, the aspect ratio decreases to the minimum value. In contrast, when the bubble passes the average position, the aspect ratio reaches the maximum value. The frequency of the periodic oscillations of τ_X and τ_Y is 5Hz, which is the same to that of zigzag motion. The frequency of the oscillation of $|\tau_Z|$ is twice of the zigzag motion as well as τ_X and τ_Y, but the same as that of the aspect ratio.

In the end, the rising bubble dynamics with heat and mass transfer (bubble condensation) are numerically investigated. Two phase change models, Lee and Tanasawa model, are assessed and analyzed for a single bubble condensation. a single bubble condensation by comparing to the experimental data. Different aspects, including the empirical coefficient, mesh size and the comparison of 2D and 3D simulation are covered. The main conclusions are summarized below.

For the Lee model, the mesh-independent results cannot be obtained due to the dependence of the mass source term on the volume of the mesh cell. Therefore, the Tanasawa model is adopted for the simulation of bubble condensation as the mesh-independent results are obtained, where mesh size $\Delta x/D_0 = 1/100$ is properly converged. The mass transfer rate increases with the increase of γ. The results (2D-simulation) obtained with $\gamma = 0.00008$ agree well with the experimental data and the relative error is less than 10%. By comparing the 2D and 3D simulation results, the variation of the bubble volume is almost the same in both cases, but the 3D bubble rises faster than the 2D bubble during the condensation process. The reasons may be: 1) the diverse shapes of the 2D and 3D bubbles leads to the different lift and drag force; 2) the mass transfer rate across the surface of the 2D and 3D bubbles is different from each other, thus the flow fields around the bubbles are different; 3) the turbulent diffusion is dampened in 2D simulation.

The increase of the bubble diameter increases the bubble Re, which greatly affects the shear stress between the rising vapor bubble and the motionless bulk, resulting in the turbulence inside the bubble more intensive and the thermal field around the bubble unstable [25, 93]. As a result, the surface wave is formed on the bubble surface. The surface wave on the bubble surface enlarges the effective area of condensation, thus increasing the mass transfer rate.

With the increase of the subcooling, the condensation becomes stronger (higher mass flux across the interface), which accelerates the instability of the bubble surface. Besides, the turbulence in the thermal field on the periphery of the bubble increases and uneven local condensation at the bubble surface might occur at higher subcooling, leading to the deformation of the interface. The breakup of the vapor bubble ($D_0 = 6$ mm) is observed with $\Delta T_{sub} = 20$ K due to the appearance of the surface wave caused by the intensive liquid motion in the rear of the bubble and the high subcooling, which brings about a Rayleigh-Taylor instability forming on the bubble surface.

The increase of the liquid viscosity restricts the bubble rising and deformation, and reduces the convective heat transfer, which decreases the condensation rate. With the decrease of the surface tension, the bubble is easier to deform and has a larger surface area than the spherical bubble, which results in the acceleration of bubble condensation.

7.2 Outlook

There are several aspects that needs further research, which are covered in the following.

- For the isothermal rising bubble dynamics, the interaction of two inline bubbles in different regimes is considered as part of future research. The rising bubble with different combination of Ga, Eo, μ_r and ρ_r yields different shapes and paths. The interaction of two bubbles in different regiomes will be more complex, especially for the bubble with path instability. The interaction of the trailing bubble with the wake structures of the leading bubble will make the study of rising bubble dynamics more difficult. The dynamics of each bubble, including the path, rising velocity, vortex dynamics and aspect ratio, must be accurately tracked and calculated numerically.

- For the non-isothermal rising dynamics, the mutual effect between the rising bubble dynamics and heat transfer needs further research. The heat transfer coefficient at the interface must be calculated accurately. Besides, the thermo-capillary effect on the bubble dynamics should be noted, such as the linear fluid and the "self-rewetting" fluid [39].

- For the bubble condensation, more accurate phase change model must be developed. Until now, no general phase change model that could solve all the flow conditions is developed. We should pay attention to the numerical techniques of the accurate interface capture, heat and mass transfer across the interface. Besides, in the present work, the smooth bubble condensation is mainly simulated and studied. However, other condensation features such as shape oscillation regime and capillary wave regime [93] should be investigated in the future. Another difficulty in simulating bubble condensation is the high computational cost. The mesh resolution must be fine enough to capture the interface when the bubble size is rather small due to the condensation. The adaptive mesh refinement may work in this case. We also notice that the physics-informed deep learning technique may also be used for the study of the bubble condensation based on the training of experimental and DNS data.

Appendix A

Code implementation of CLSVOF method

```
//----calculation of mesh size Delta x----//
volScalarField CellDims
(
   IOobject
   (
      "CellDims",
     runTime.timeName(),
      mesh,
     IOobject::NO_READ,
     IOobject::NO_WRITE
   ),
   mesh,
   dimensionedScalar("dummy", dimensionSet(0,1,0,0,0,0,0), 0)
);
// Like above, but longest cell dimensions - useful for checking
    interface location
volScalarField MaxCellDims
(
   IOobject
```

```
   (
    "MaxCellDims",
    runTime.timeName(),
    mesh,
    IOobject::NO_READ,
    IOobject::NO_WRITE
   ),
   mesh,
   dimensionedScalar("dummy", dimensionSet(0,1,0,0,0,0,0), 0)
);

const cellList& cells = mesh.cells();

forAll(cells, c) // over all cells
{
   scalar Dim = GREAT;
   scalar MaxDim = SMALL;
   const labelList& curEdges = mesh.cellEdges()[c];
   // Now go through cell edges and get min
   forAll (curEdges, e)
   {
        scalar len = mesh.edges()[curEdges[e]].mag(mesh.points());
        if (len < Dim)
        {
           Dim = len;
        }
        if (len > MaxDim)
        {
           MaxDim = Dim;
        }
     }
     CellDims[c] = Dim;
     MaxCellDims[c] = MaxDim;
```

```
}

Info<< "Minimum cell dimension: " << gMin(CellDims) << endl;
dimensionedScalar DeltaX = gMin(CellDims);
//----non-dimensional delta x----//
dimensionedScalar dimChange
(
   dimensionedScalar("dimChange",dimLength, 1.0)
);
scalar deltaX = DeltaX/dimChange;
//----calculation of Gamma----//
gamma_
(
   "gamma",
   deltaX*double(0.75)
)
//----Calculation of the initial level set field----//
psi0 == (double(2.0)*alpha1 - double(1.0))*gamma;
//----calculation of the sign function S(phi0)----//
volScalarField psiSign
(
   IOobject
   (
      "psiSign",
      runTime.timeName(),
      mesh,
      IOobject::NO_READ,
      IOobject::AUTO_WRITE
   ),
   mesh,
   dimensionedScalar("psiSign",dimless, 0.0)
);
psiSign = psi0/(mag(psi0)+1e-8);
```

```
//----Calculation of the non-dimensional interface thickness----//
epsilon
(
   "epsilon",
   deltaX*double(1.5)
)
//----calculation of artificial time step----//
deltaTau
(
   "deltaTau",
   deltaX*double(0.1)
)
//----calculation of level set function----//
psi = psi0
for (int corr=0; corr<int(epsilon/deltaTau); corr++)
{
   psi == psi +
       psiSign*(double(1)-mag(fvc::grad(psi)*dimChange))*deltaTau;
   psi.correctBoundaryConditions();
}
```

Appendix B

Code implementation of surface tension force

```
//----calculation of surface tension force based on volume fraction
   field----//
const fvMesh& mesh = alpha1.mesh();
const surfaceVectorField& Sf = mesh.Sf();

// Cell gradient of alpha
const volVectorField gradAlpha(fvc::grad(alpha1, "nHat"));

// Interpolated face-gradient of alpha
surfaceVectorField gradAlphaf(fvc::interpolate(gradAlpha));

// Face unit interface normal
surfaceVectorField nHatfv(gradAlphaf/(mag(gradAlphaf) + deltaN));

correctContactAngle(nHatfv.boundaryFieldRef(),
   gradAlphaf.boundaryField());

// Face unit interface normal flux
nHatf = nHatfv & Sf;
```

```
// Simple expression for curvature
K = -fvc::div(nHatf_);
// calculation of surface tension force
sigmaK = sigma*K;
surfaceTensionForce = fvc::interpolate(sigmaK)*fvc::snGrad(alpha1)

//----calculation of surface tension force based on level set
   field----//
const fvMesh& mesh = psi.mesh();
const surfaceVectorField& Sf = mesh.Sf();
// Cell gradient of psi
const volVectorField gradPsi(fvc::grad(psi));

// Interpolated face-gradient of psi
surfaceVectorField gradPsif(fvc::interpolate(gradPsi));

// Face unit interface normal
nVecfv = gradPsif/(mag(gradPsif) + deltaN);
correctContactAngle(nVecfv_.boundaryFieldRef(),
   gradPsif.boundaryField());

// Face unit interface normal flux
nVecf = nVecfv & Sf;

// Simple expression for curvature
C = -fvc::div(nVecf);

//calculation of delta function
forAll(psi.mesh().cells(),celli)
{
  if(mag(psi[celli]) > epsilon)
    delta[celli] = double(0.0);
  else
```

```
     delta_[celli] = double(1.0)/(double(2.0)*epsilon_.value())
     *(double(1.0)+cos(M_PI*psi[celli]/epsilon)));
}
// calculation of surface tension force
sigmaC = sigma*C;
surfaceTensionForce = fvc::interpolate(sigmaC)
*fvc::snGrad(psi)*fvc::interpolate(delta);
```

Bibliography

[1] Neil E Todreas and Mujid S Kazimi. *Nuclear systems: thermal hydraulic fundamentals*, volume 1. CRC press, 2012.

[2] Dahya Bhaga and ME Weber. Bubbles in viscous liquids: shapes, wakes and velocities. *Journal of Fluid Mechanics*, 105:61–85, 1981.

[3] DM Sharaf, AR Premlata, Manoj Kumar Tripathi, Badarinath Karri, and Kirti Chandra Sahu. Shapes and paths of an air bubble rising in quiescent liquids. *Physics of Fluids*, 29(12):122104, 2017.

[4] Manoj Kumar Tripathi, Kirti Chandra Sahu, and Rama Govindarajan. Dynamics of an initially spherical bubble rising in quiescent liquid. *Nature Communications*, 6:6268, 2015.

[5] Yuanwei Cao and Rafael Macián-Juan. Numerical investigation of central breakup of large bubble induced by liquid jet. *Physics of Fluids*, 32(3):033302, 2020.

[6] Kun Luo, Changxiao Shao, Min Chai, and Jianren Fan. Level set method for atomization and evaporation simulations. *Progress in Energy and Combustion Science*, 73:65–94, 2019.

[7] Liu Liu, Hongjie Yan, Guojian Zhao, and Jiacai Zhuang. Experimental studies on the terminal velocity of air bubbles in water and glycerol aqueous solution. *Experimental Thermal and Fluid Science*, 78:254–265, 2016.

[8] Shelley Lynn Anna. Droplets and bubbles in microfluidic devices. *Annual Review of Fluid Mechanics*, 48:285–309, 2016.

[9] Roberto Zenit and Javier Rodriguez Rodriguez. The fluid mechanics of bubbly drinks. *Physics today*, 71(11):44–50, 2018.

[10] Manoj Kumar Tripathi, AR Premlata, Kirti Chandra Sahu, and Rama Govindarajan. Two initially spherical bubbles rising in quiescent liquid. *Physical Review Fluids*, 2(7):073601, 2017.

[11] B Aboulhasanzadeh and G Tryggvason. Effect of bubble interactions on mass transfer in bubbly flow. *International Journal of Heat and Mass Transfer*, 79:390–396, 2014.

[12] Rajiva Lochan Mohanty and Mihir Kumar Das. A critical review on bubble dynamics parameters influencing boiling heat transfer. *Renewable and Sustainable Energy Reviews*, 78:466–494, 2017.

[13] Monica Gumulya, Jyeshtharaj B Joshi, Ranjeet P Utikar, Geoffrey M Evans, and Vishnu Pareek. Bubbles in viscous liquids: Time dependent behaviour and wake characteristics. *Chemical Engineering Science*, 144:298–309, 2016.

[14] Amanda HLM Charin, Paulo LC Lage, Luiz Fernando LR Silva, Željko Tuković, and Hrvoje Jasak. On the dynamic behavior of rising droplets. *International Journal of Multiphase Flow*, 110:165–178, 2019.

[15] JR Landel, Carlo Cossu, and CP Caulfield. Spherical cap bubbles with a toroidal bubbly wake. *Physics of Fluids*, 20(12):122101, 2008.

[16] S Winnikow and BT Chao. Droplet motion in purified systems. *The Physics of Fluids*, 9(1):50–61, 1966.

[17] Gregory Ryskin and LG Leal. Numerical solution of free-boundary problems in fluid mechanics. part 2. buoyancy-driven motion of a gas

bubble through a quiescent liquid. *Journal of Fluid Mechanics*, 148:19–35, 1984.

[18] PC Duineveld. The rise velocity and shape of bubbles in pure water at high reynolds number. *Journal of Fluid Mechanics*, 292:325–332, 1995.

[19] A Tomiyama, GP Celata, S Hosokawa, and S Yoshida. Terminal velocity of single bubbles in surface tension force dominant regime. *International Journal of Multiphase Flow*, 28(9):1497–1519, 2002.

[20] AWG De Vries, A Biesheuvel, and L Van Wijngaarden. Notes on the path and wake of a gas bubble rising in pure water. *International Journal of Multiphase Flow*, 28(11):1823–1835, 2002.

[21] Christian Veldhuis, Arie Biesheuvel, and Leen Van Wijngaarden. Shape oscillations on bubbles rising in clean and in tap water. *Physics of Fluids*, 20(4):040705, 2008.

[22] M Wegener, J Grünig, J Stüber, AR Paschedag, and M Kraume. Transient rise velocity and mass transfer of a single drop with interfacial instabilities–experimental investigations. *Chemical Engineering Science*, 62(11):2967–2978, 2007.

[23] Mirco Wegener, Matthias Kraume, and Anja R Paschedag. Terminal and transient drop rise velocity of single toluene droplets in water. *AIChE journal*, 56(1):2–10, 2010.

[24] M Wegener, N Paul, and M Kraume. Fluid dynamics and mass transfer at single droplets in liquid/liquid systems. *International Journal of Heat and Mass Transfer*, 71:475–495, 2014.

[25] S Al Issa, P Weisensee, and R Macián-Juan. Experimental investigation of steam bubble condensation in vertical large diameter geometry under atmospheric pressure and different flow conditions. *International Journal of Heat and Mass Transfer*, 70:918–929, 2014.

[26] AM Zhang, P Cui, J Cui, and QX Wang. Experimental study on bubble dynamics subject to buoyancy. *Journal of Fluid Mechanics*, 776:137–160, 2015.

[27] QX Wang and K Manmi. Three dimensional microbubble dynamics near a wall subject to high intensity ultrasound. *Physics of Fluids*, 26(3):032104, 2014.

[28] Habiba Lais, Premesh S Lowe, Tat-Hean Gan, and Luiz C Wrobel. Numerical modelling of acoustic pressure fields to optimize the ultrasonic cleaning technique for cylinders. *Ultrasonics Sonochemistry*, 45:7–16, 2018.

[29] Timothy L Hall, Hedieh Alavi Tamaddoni, Alexander P Duryea, and William W Roberts. Acoustic removal of cavitation nuclei to enhance stone comminution in shockwave lithotripsy. *The Journal of the Acoustical Society of America*, 141(5):3673–3673, 2017.

[30] Michael S Mihatsch, Steffen J Schmidt, and Nikolaus A Adams. Cavitation erosion prediction based on analysis of flow dynamics and impact load spectra. *Physics of Fluids*, 27(10):103302, 2015.

[31] Thomas Séon and Arnaud Antkowiak. Large bubble rupture sparks fast liquid jet. *Physical Review Letters*, 109(1):014501, 2012.

[32] T Séon and A Antkowiak. Jets in viscous bubbles. *Physics of Fluids*, 23(9):091103, 2011.

[33] LT Liu, XL Yao, AM Zhang, and YY Chen. Numerical analysis of the jet stage of bubble near a solid wall using a front tracking method. *Physics of Fluids*, 29(1):012105, 2017.

[34] Tong Li, A-Man Zhang, Shi-Ping Wang, Shuai Li, and Wen-Tao Liu. Bubble interactions and bursting behaviors near a free surface. *Physics of Fluids*, 31(4):042104, 2019.

[35] Mitsuhiro Ohta, Tatsuya Imura, Yutaka Yoshida, and Mark Sussman. A computational study of the effect of initial bubble conditions on the motion of a gas bubble rising in viscous liquids. *International Journal of Multiphase Flow*, 31(2):223–237, 2005.

[36] Thomas Bonometti and Jacques Magnaudet. Transition from spherical cap to toroidal bubbles. *Physics of Fluids*, 18(5):052102, 2006.

[37] Li Chen, Suresh V Garimella, John A Reizes, and Eddie Leonardi. The development of a bubble rising in a viscous liquid. *Journal of Fluid Mechanics*, 387:61–96, 1999.

[38] Yuanwei Cao and Rafael Macián-Juan. Numerical study of the central breakup behaviors of a large bubble rising in quiescent liquid. *Chemical Engineering Science*, page 115804, 2020.

[39] Manoj Kumar Tripathi, KC Sahu, G Karapetsas, K Sefiane, and OK Matar. Non-isothermal bubble rise: non-monotonic dependence of surface tension on temperature. *Journal of Fluid Mechanics*, 763:82–108, 2015.

[40] Mounika Balla, Manoj Kumar Tripathi, Kirti Chandra Sahu, George Karapetsas, and Omar K Matar. Non-isothermal bubble rise dynamics in a self-rewetting fluid: three-dimensional effects. *Journal of Fluid Mechanics*, 858:689–713, 2019.

[41] Alexander Potapov, Roman Spivak, Olga M Lavrenteva, and Avinoam Nir. Motion and deformation of drops in bingham fluid. *Industrial & Engineering Chemistry Research*, 45(21):6985–6995, 2006.

[42] Manoj Kumar Tripathi, Kirti Chandra Sahu, George Karapetsas, and Omar K Matar. Bubble rise dynamics in a viscoplastic material. *Journal of Non-Newtonian Fluid Mechanics*, 222:217–226, 2015.

[43] Kirti Chandra Sahu. A review on rising bubble dynamics in viscosity-stratified fluids. *Sādhanā*, 42(4):575–583, 2017.

[44] NO Young, JS Goldstein, and Mi J Block. The motion of bubbles in a vertical temperature gradient. *Journal of Fluid Mechanics*, 6(3):350–356, 1959.

[45] J Tsamopoulos, Y Dimakopoulos, N Chatzidai, G Karapetsas, and M Pavlidis. Steady bubble rise and deformation in newtonian and viscoplastic fluids and conditions for bubble entrapment. *Journal of Fluid Mechanics*, 601:123–164, 2008.

[46] Mohammad Majlesara, Omid Abouali, Reza Kamali, Mehdi Niazi Ardekani, and Luca Brandt. Numerical study of hot and cold spheroidal particles in a viscous fluid. *International Journal of Heat and Mass Transfer*, 149:119206, 2020.

[47] Seong-Su Jeon, Seong-Jin Kim, and Goon-Cherl Park. Numerical study of condensing bubble in subcooled boiling flow using volume of fluid model. *Chemical Engineering Science*, 66(23):5899–5909, 2011.

[48] Liang-ming Pan, Zhi-wei Tan, De-qi Chen, and Long-chang Xue. Numerical investigation of vapor bubble condensation characteristics of subcooled flow boiling in vertical rectangular channel. *Nuclear Engineering and Design*, 248:126–136, 2012.

[49] Qingyun Zeng, Jiejin Cai, Huaqiang Yin, Xingtuan Yang, and Tadashi Watanabe. Numerical simulation of single bubble condensation in subcooled flow using openfoam. *Progress in Nuclear Energy*, 83:336–346, 2015.

[50] Xiao-hang Qu and Mao-cheng Tian. Acoustic and visual study on condensation of steam–air mixture jet plume in subcooled water. *Chemical Engineering Science*, 144:216–223, 2016.

[51] Hongli Liu, Jiguo Tang, Licheng Sun, Zhengyu Mo, and Guo Xie. An assessment and analysis of phase change models for the simulation of

vapor bubble condensation. *International Journal of Heat and Mass Transfer*, 157:119924, 2020.

[52] José Carlos Cano-Lozano, Carlos Martinez-Bazan, Jacques Magnaudet, and Joël Tchoufag. Paths and wakes of deformable nearly spheroidal rising bubbles close to the transition to path instability. *Physical Review Fluids*, 1(5):053604, 2016.

[53] Rogerio Manica, Evert Klaseboer, and Derek YC Chan. The hydrodynamics of bubble rise and impact with solid surfaces. *Advances in Colloid and Interface Science*, 235:214–232, 2016.

[54] Ian Davis, Rudi O'Reilly Meehan, Kevin Nolan, Kieran Grennan, and Darina Murray. A wake tracking approach for two-phase schlieren. *International Journal of Multiphase Flow*, 102:38–48, 2018.

[55] Cyril W Hirt and Billy D Nichols. Volume of fluid (vof) method for the dynamics of free boundaries. *Journal of Computational Physics*, 39(1):201–225, 1981.

[56] Stanley Osher and James A Sethian. Fronts propagating with curvature-dependent speed: algorithms based on hamilton-jacobi formulations. *Journal of Computational Physics*, 79(1):12–49, 1988.

[57] Mark Sussman, Peter Smereka, and Stanley Osher. A level set approach for computing solutions to incompressible two-phase flow. *Journal of Computational physics*, 114(1):146–159, 1994.

[58] Antoine du Chéné, Chohong Min, and Frédéric Gibou. Second-order accurate computation of curvatures in a level set framework using novel high-order reinitialization schemes. *Journal of Scientific Computing*, 35(2-3):114–131, 2008.

[59] Frederic Gibou, Ronald Fedkiw, and Stanley Osher. A review of level-set methods and some recent applications. *Journal of Computational Physics*, 353:82–109, 2018.

[60] Mathieu Coquerelle and Stéphane Glockner. A fourth-order accurate curvature computation in a level set framework for two-phase flows subjected to surface tension forces. *Journal of Computational Physics*, 305:838–876, 2016.

[61] Jiaqi Zhang and Pengtao Yue. A high-order and interface-preserving discontinuous galerkin method for level-set reinitialization. *Journal of Computational Physics*, 378:634–664, 2019.

[62] Murray Rudman. Volume-tracking methods for interfacial flow calculations. *International Journal for Numerical Methods in Fluids*, 24(7):671–691, 1997.

[63] O Ubbink and RI Issa. A method for capturing sharp fluid interfaces on arbitrary meshes. *Journal of Computational Physics*, 153(1):26–50, 1999.

[64] Henry G Weller, Gavin Tabor, Hrvoje Jasak, and Christer Fureby. A tensorial approach to computational continuum mechanics using object-oriented techniques. *Computers in physics*, 12(6):620–631, 1998.

[65] Henry G Weller. A new approach to vof-based interface capturing methods for incompressible and compressible flow. *OpenCFD Ltd., Report TR/HGW*, 4, 2008.

[66] Bruno Lafaurie, Carlo Nardone, Ruben Scardovelli, Stéphane Zaleski, and Gianluigi Zanetti. Modelling merging and fragmentation in multiphase flows with surfer. *Journal of Computational Physics*, 113(1):134–147, 1994.

[67] Suraj S Deshpande, Lakshman Anumolu, and Mario F Trujillo. Evaluating the performance of the two-phase flow solver interfoam. *Computational Science & Discovery*, 5(1):014016, 2012.

[68] Simon Hill, Daniel Deising, Thomas Acher, Harald Klein, Dieter Bothe, and Holger Marschall. Boundedness-preserving implicit correction of

mesh-induced errors for vof based heat and mass transfer. *Journal of Computational Physics*, 352:285–300, 2018.

[69] William F Noh and Paul Woodward. Slic (simple line interface calculation). In *Proceedings of the fifth international conference on numerical methods in fluid dynamics June 28–July 2, 1976 Twente University, Enschede*, pages 330–340. Springer, 1976.

[70] William J Rider and Douglas B Kothe. Reconstructing volume tracking. *Journal of Computational Physics*, 141(2):112–152, 1998.

[71] Johan Roenby, Henrik Bredmose, and Hrvoje Jasak. A computational method for sharp interface advection. *Royal Society Open Science*, 3(11):160405, 2016.

[72] Jeremiah U Brackbill, Douglas B Kothe, and Charles Zemach. A continuum method for modeling surface tension. *Journal of computational physics*, 100(2):335–354, 1992.

[73] Mark Sussman and Elbridge Gerry Puckett. A coupled level set and volume-of-fluid method for computing 3d and axisymmetric incompressible two-phase flows. *Journal of Computational Physics*, 162(2):301–337, 2000.

[74] Zhaoyuan Wang, Jianming Yang, Bonguk Koo, and Frederick Stern. A coupled level set and volume-of-fluid method for sharp interface simulation of plunging breaking waves. *International Journal of Multiphase Flow*, 35(3):227–246, 2009.

[75] A Albadawi, DB Donoghue, AJ Robinson, DB Murray, and YMC Delauré. Influence of surface tension implementation in volume of fluid and coupled volume of fluid with level set methods for bubble growth and detachment. *International Journal of Multiphase Flow*, 53:11–28, 2013.

[76] Mehriar Dianat, Maciej Skarysz, and Andrew Garmory. A coupled level set and volume of fluid method for automotive exterior water management applications. *International Journal of Multiphase Flow*, 91:19–38, 2017.

[77] Chirag R Kharangate and Issam Mudawar. Review of computational studies on boiling and condensation. *International Journal of Heat and Mass Transfer*, 108:1164–1196, 2017.

[78] Wen Ho Lee. Pressure iteration scheme for two-phase flow modeling. *IN" MULTIPHASE TRANSPORT: FUNDAMENTALS, REACTOR SAFETY, APPLICATIONS".*, pages 407–432, 1980.

[79] Zheng Yang, XF Peng, and P Ye. Numerical and experimental investigation of two phase flow during boiling in a coiled tube. *International Journal of Heat and Mass Transfer*, 51(5-6):1003–1016, 2008.

[80] HL Wu, XF Peng, P Ye, and Y Eric Gong. Simulation of refrigerant flow boiling in serpentine tubes. *International Journal of Heat and Mass Transfer*, 50(5-6):1186–1195, 2007.

[81] Robert W Schrage. *A theoretical study of interphase mass transfer*. Columbia University Press, 1953.

[82] Ichiro Tanasawa. Advances in condensation heat transfer. In *Advances in Heat Transfer*, volume 21, pages 55–139. Elsevier, 1991.

[83] N Samkhaniani and MR Ansari. Numerical simulation of bubble condensation using cf-vof. *Progress in Nuclear Energy*, 89:120–131, 2016.

[84] Frédéric Gibou, Liguo Chen, Duc Nguyen, and Sanjoy Banerjee. A level set based sharp interface method for the multiphase incompressible navier–stokes equations with phase change. *Journal of Computational Physics*, 222(2):536–555, 2007.

[85] Dong-Liang Sun, Jin-Liang Xu, and Li Wang. Development of a vapor–liquid phase change model for volume-of-fluid method in fluent. *International Communications in Heat and Mass Transfer*, 39(8):1101–1106, 2012.

[86] Jerrold Isenberg and Samuel Sideman. Direct contact heat transfer with change of phase: bubble condensation in immiscible liquids. *International Journal of Heat and Mass Transfer*, 13(6):997–1011, 1970.

[87] Mamoru AKIYAMA. Bubble collapse in subcooled boiling. *Bulletin of JSME*, 16(93):570–575, 1973.

[88] YM Chen and F Mayinger. Measurement of heat transfer at the phase interface of condensing bubbles. *International Journal of Multiphase Flow*, 18(6):877–890, 1992.

[89] Gopinath R Warrier, Nilanjana Basu, and Vijay K Dhir. Interfacial heat transfer during subcooled flow boiling. *International Journal of Heat and Mass Transfer*, 45(19):3947–3959, 2002.

[90] Yuan Dewen, Pan Liangming, Chen Deqi, and Wang Xiaojun. Condensation heat transfer coefficient at vapour-liquid interface of subcooled flow boiling in vertical narrow rectangular channel. *Nuclear Power Engineering*, 30, 2009.

[91] A Lucic and F Mayinger. Transportphenomena in subcooled flow boiling. *Heat and mass transfer*, 46(10):1159–1166, 2010.

[92] Seong-Jin Kim and Goon-Cherl Park. Interfacial heat transfer of condensing bubble in subcooled boiling flow at low pressure. *International Journal of Heat and Mass Transfer*, 54(13-14):2962–2974, 2011.

[93] Jiguo Tang, Changqi Yan, and Licheng Sun. A study visualizing the collapse of vapor bubbles in a subcooled pool. *International Journal of Heat and Mass Transfer*, 88:597–608, 2015.

[94] Henning Scheufler and Johan Roenby. Accurate and efficient surface reconstruction from volume fraction data on general meshes. *Journal of Computational Physics*, 383:1–23, 2019.

[95] OpenFOAM OpenCFD. The open source cfd toolbox–user's guide. *OpenCFD Ltd., United Kingdom*, 1, 2012.

[96] Steven T Zalesak. Fully multidimensional flux-corrected transport algorithms for fluids. *Journal of Computational Physics*, 31(3):335–362, 1979.

[97] Edin Berberović, Nils P van Hinsberg, Suad Jakirlić, Ilia V Roisman, and Cameron Tropea. Drop impact onto a liquid layer of finite thickness: Dynamics of the cavity evolution. *Physical Review E*, 79(3):036306, 2009.

[98] Martin Knudsen and JR Partington. The kinetic. theoryof gases. some modern aspects. *The Journal of Physical Chemistry*, 39(2):307–307, 2002.

[99] R Marek and J Straub. Analysis of the evaporation coefficient and the condensation coefficient of water. *International Journal of Heat and Mass Transfer*, 44(1):39–53, 2001.

[100] Yuanwei Cao and Rafael Macián-Juan. The wobbling motion of single and two inline bubbles rising in quiescent liquid. *Physics of Fluids*, 33(7):073305, 2021.

[101] Shu-Ren Hysing, Stefan Turek, Dmitri Kuzmin, Nicola Parolini, Erik Burman, Sashikumaar Ganesan, and Lutz Tobiska. Quantitative benchmark computations of two-dimensional bubble dynamics. *International Journal for Numerical Methods in Fluids*, 60(11):1259–1288, 2009.

[102] J Klostermann, K Schaake, and R Schwarze. Numerical simulation of a single rising bubble by vof with surface compression. *International Journal for Numerical Methods in Fluids*, 71(8):960–982, 2013.

[103] Takuya Yamamoto, Yasunori Okano, and Sadik Dost. Validation of the s-clsvof method with the density-scaled balanced continuum surface force model in multiphase systems coupled with thermocapillary flows. *International Journal for Numerical Methods in Fluids*, 83(3):223–244, 2017.

[104] Yuanwei Cao, Inés Mateos Canals, and Rafael Macián-Juan. Path instability of a compressible air bubble rising in quiescent water with consideration of variable thermophysical properties. *International Journal of Multiphase Flow*, page 103320, 2020.

[105] Jie Zhang and Ming-Jiu Ni. What happens to the vortex structures when the rising bubble transits from zigzag to spiral? *Journal of Fluid Mechanics*, 828:353–373, 2017.

[106] Jyeshtharaj B Joshi, K Nandakumar, Geoffrey M Evans, Vishnu K Pareek, Monica M Gumulya, Mayur J Sathe, and Makrand A Khanwale. Bubble generated turbulence and direct numerical simulations. *Chemical Engineering Science*, 157:26–75, 2017.

[107] M Gumulya, RP Utikar, VK Pareek, GM Evans, and JB Joshi. Dynamics of bubbles rising in pseudo-2d bubble column: Effect of confinement and inertia. *Chemical Engineering Journal*, 405:126615, 2021.

[108] Jinhee Jeong and Fazle Hussain. On the identification of a vortex. *Journal of Fluid Mechanics*, 285:69–94, 1995.

[109] Jigen Zhou, Ronald J Adrian, S Balachandar, and TM Kendall. Mechanisms for generating coherent packets of hairpin vortices in channel flow. *Journal of Fluid Mechanics*, 387:353–396, 1999.

[110] Arahata Senapati, Gaurav Singh, and Rajaram Lakkaraju. Numerical simulations of an inline rising unequal-sized bubble pair in a liquid column. *Chemical Engineering Science*, 208:115159, 2019.

[111] Yang Zhang, Ke Chen, Yunxiang You, and Wei Ren. Coalescence of two initially spherical bubbles: Dual effect of liquid viscosity. *International Journal of Heat and Fluid Flow*, 72:61–72, 2018.

[112] Audrey Filella, Patricia Ern, and Veronique Roig. Interaction of two oscillating bubbles rising in a thin-gap cell: vertical entrainment and interaction with vortices. *Journal of Fluid Mechanics*, 888, 2020.

[113] Hiroaki Kusuno and Toshiyuki Sanada. Wake-induced lateral migration of approaching bubbles. *International Journal of Multiphase Flow*, 139:103639, 2021.

[114] Sergio A Baz-Rodríguez, Jorge Ramírez-Muñoz, Alberto Soria, and Julio C Sacramento-Rivero. Hydrodynamic interaction of two spherical bubbles rising in-line: a semi-analytical approach. *Chemical Engineering Communications*, 201(5):674–687, 2014.

[115] Stefan Turek. *Efficient Solvers for Incompressible Flow Problems: An Algorithmic and Computational Approache*, volume 6. Springer Science & Business Media, 1999.

[116] Nicola Parolini. Computational fluid dynamics for naval engineering problems. Technical report, EPFL, 2004.

[117] Volker John and Gunar Matthies. Moonmd–a program package based on mapped finite element methods. *Computing and Visualization in Science*, 6(2-3):163–170, 2004.

[118] Marianne M Francois, Sharen J Cummins, Edward D Dendy, Douglas B Kothe, James M Sicilian, and Matthew W Williams. A balanced-force

algorithm for continuous and sharp interfacial surface tension models within a volume tracking framework. *Journal of Computational Physics*, 213(1):141–173, 2006.

[119] Qingming Liu and Björn Palm. Numerical study of bubbles rising and merging during convective boiling in micro-channels. *Applied Thermal Engineering*, 99:1141–1151, 2016.

[120] Françoise Brochard-Wyart and David Quéré. *Capillarity and wetting phenomena: drops, bubbles, pearls, waves*. Springer, 2004.

[121] Yuriko Renardy and Michael Renardy. Prost: a parabolic reconstruction of surface tension for the volume-of-fluid method. *Journal of Computational Physics*, 183(2):400–421, 2002.

[122] Iztok Zun, Matjaz Perpar, Jurij Gregorc, Kosuke Hayashi, and Akio Tomiyama. Mixing of thermally stratified water layer by a free rising wobbling air bubble. *Chemical Engineering Science*, 72:155–171, 2012.

[123] Zlatko Rek. Using a dynamic and constant mesh in numerical simulation of the free-rising bubble. *Fluids*, 4(1):38, 2019.

[124] M Horowitz and CHK Williamson. The effect of reynolds number on the dynamics and wakes of freely rising and falling spheres. *Journal of Fluid Mechanics*, 651:251, 2010.

[125] Jacques Magnaudet and Guillaume Mougin. Wake instability of a fixed spheroidal bubble. *Journal of Fluid Mechanics*, 572:311–337, 2007.

[126] Yuanwei Cao and Rafael Macián-Juan. Numerical investigation of vapor bubble condensation in subcooled quiescent water. *Nuclear Engineering and Design*, 388:111621, 2022.

[127] Hongrae Jo and Daeseong Jo. Experimental studies of condensing vapor bubbles in subcooled pool water using visual and acoustic analysis methods. *Annals of Nuclear Energy*, 110:171–185, 2017.

[128] Christoph Brücker. Structure and dynamics of the wake of bubbles and its relevance for bubble interaction. *Physics of Fluids*, 11(7):1781–1796, 1999.

[129] M Gumulya, JB Joshi, RP Utikar, GM Evans, and Vishnu Pareek. Characteristics of energy production and dissipation around a bubble rising in water. *Chemical Engineering Science*, 193:38–52, 2019.